

**STUDIES ON ELEVATED
TEMPERATURE TRIBOLOGICAL
BEHAVIOR OF FLY ASH BASED
PLASMA SPRAY COATINGS**

Thesis

Submitted in partial fulfillment of the requirements for the degree of

DOCTOR OF PHILOSOPHY

by

MAHANTAYYA MATHAPATI



DEPARTMENT OF MECHANICAL ENGINEERING
NATIONAL INSTITUTE OF TECHNOLOGY KARNATAKA,
SURATHKAL, MANGALORE – 575025

SEPTEMBER, 2018

DECLARATION

I hereby *declare* that the Research Thesis entitled “**STUDIES ON ELEVATED TEMPERATURE TRIBOLOGICAL BEHAVIOR OF FLY ASH BASED PLASMA SPRAY COATINGS**” which is being submitted to the **National Institute of Technology Karnataka, Surathkal** in partial fulfillment of the requirements for the award of the Degree of **Doctor of Philosophy** in **Department of Mechanical Engineering** is a *bonafide report of the research work carried out by me*. The material contained in this Research Thesis has not been submitted to any University or Institution for the award of any degree.

Register Number : **145084ME14F09**

Name of the Research Scholar : **MAHANTAYYA MATHAPATI**

Signature of the Research Scholar:

Department of Mechanical Engineering

Place : **NITK, Surathkal**

Date :

C E R T I F I C A T E

This is to *certify* that the Research Thesis entitled “**STUDIES ON ELEVATED TEMPERATURE TRIBOLOGICAL BEHAVIOR OF FLY ASH BASED PLASMA SPRAY COATINGS**” submitted by **Mr. MAHANTAYYA MATHAPATI (Register Number: 145084ME14F09)** as the record of the research work carried out by him, is *accepted as the Research Thesis submission* in partial fulfillment of the requirements for the award of degree of **Doctor of Philosophy**.

Research Guides

Dr. Ramesh M R
Associate Professor
Department of Mechanical
Engineering, NITK, Surathkal

Dr. Mrityunjay Doddamani
Assistant Professor
Department of Mechanical
Engineering, NITK, Surathkal

Chairman – DRPC

Date:

ACKNOWLEDGEMENT

I would like to extend my gratitude to Dr. Ramesh M R, Associate Professor and Dr. Mrityunjay Doddamani, Assistant Professor, Mechanical Engineering, National Institute of Technology Karnataka (NITK), Surathkal for the invaluable constructive guidance and encouragement extended throughout my study.

I would like to thank my Research Progress Assessment Committee members Dr. H. Shivananda Nayaka and Dr. Raviraj H. M. for their valuable inputs.

I would like to thank Prof. S. Narendranath, Head of the Mechanical Engineering Department and all the members of faculty, Mechanical Engineering, NITK for their support throughout this research work.

Constant encouragement of my family to pursue higher studies has made it possible for me to reach this stage. I wish to thank all my family members for love, help and encouragement provided. A special note of thanks to all my friends and well wishers for their constant help, encouragement, and understanding.

ABSTRACT

Material behavior at elevated temperature is becoming an increasing technological importance. Components working at higher temperatures like in land based gas and steam turbines, power generation boiler tubes, hot sections of aero engine, propulsion bearings, materials processing and internal combustion engines are subjected to surface friction, wear, oxidation and hot corrosion conditions. Service conditions of such components in elevated temperature environments may compromise their mechanical properties resulting in the reduced life cycle. Components working in such adverse conditions demand suitable surface modification techniques like thermal spray coatings that are widely adopted in similar situations.

Plasma spray coating processes belong to the family of thermal spraying techniques and are widely used in many industries to protect the components against erosion, oxidation and wear. Thermal energy is utilized in this process to deposit a wide variety of materials including finely divided metallic and non-metallic materials. Higher temperatures utilized in these processes enable the use of coating materials with very high melting points like ceramics, cermets, and refractory alloys. The present work explores the possibility of using fly ash based plasma spray coatings for high temperature applications. The proposed coatings are investigated for their resistance to erosion, oxidation and wear under laboratory conditions.

Commercially available Cr_3C_2 -25NiCr, NiCrAlY, WC-Co, fly ash cenospheres, MoS_2 , CaF_2 and CaSO_4 are used as coating feedstock in the present investigation. Six types of coatings namely Cr_3C_2 -NiCr/Cenosphere, NiCrAlY/WC-Co/Cenosphere, Cr_3C_2 -NiCr/Cenosphere/ MoS_2 / CaF_2 , Cr_3C_2 -NiCr/Cenosphere/ MoS_2 / CaSO_4 , NiCrAlY/WC-Co /Cenosphere/ MoS_2 / CaF_2 and NiCrAlY/WC-Co /Cenosphere/ MoS_2 / CaSO_4 are deposited on MDN 321 steel substrate (Midhani Grade). Coatings are characterized using Scanning Electron Microscope (SEM), Energy Dispersive Spectroscopy (EDS) and X-ray diffraction (XRD). Further, microstructure and mechanical properties (microhardness, adhesion strength, erosion, oxidation, and wear) have been characterized to evaluate their potential for high

temperature application. For the chosen spray parameters, seemingly dense laminar structured coatings (six types as mentioned earlier) with a thickness in the range of 350-400 μm having porosity lower than 5 % has been achieved.

Erosion behavior of MDN 321 steel, $\text{Cr}_3\text{C}_2\text{-NiCr/Cenosphere}$, and $\text{NiCrAlY/WC-Co/Cenosphere}$ coatings are investigated at elevated temperatures using solid particle erosion test (ASTM G76-13) set up at 200, 400, 600 $^\circ\text{C}$ with 30 and 90 $^\circ$ impact angles using alumina erodent. Erosion resistance of both the coatings is observed to be higher than the substrate for the test temperatures chosen and noted to be more prominent at lower impact angle and higher temperature. Both the coatings exhibited a brittle mode of material removal through brittle cracking and chipping. $\text{NiCrAlY/WC-Co/Cenosphere}$ coating reported better erosion resistance as compared to $\text{Cr}_3\text{C}_2\text{-NiCr/Cenosphere}$ coating which may be attributed to plastic deformation of the NiCrAlY matrix due to the ductility of the matrix and hard WC-Co reinforcement to resist the matrix plow thereby reduces the erosion loss.

Cyclic oxidation behavior of MDN 321 steel, $\text{Cr}_3\text{C}_2\text{-NiCr/Cenosphere}$ and $\text{NiCrAlY/WC-Co/Cenosphere}$ coatings are further carried out at 600 $^\circ\text{C}$ for 20 cycles. Each cycle consisted of heating at 600 $^\circ\text{C}$ for 1 hour, followed by 20 minutes of cooling in air. The thermogravimetric technique is used to approximate the kinetics of oxidation of substrate and coatings. Both the coatings reported lower weight gain as compared to the substrate. $\text{NiCrAlY/WC-Co/Cenosphere}$ coating registered less weight gain as compared to $\text{Cr}_3\text{C}_2\text{-NiCr/Cenosphere}$ coating which is attributed to the excellent oxidation resistance of NiCrAlY and formation of CoWO_4 along with NiO and Cr_2O_3 oxides on the coating surface.

Influence of solid lubricants on $\text{Cr}_3\text{C}_2\text{-NiCr/Cenosphere}$ and $\text{NiCrAlY/WC-Co/Cenosphere}$ coatings is dealt next for tribological response. Dry sliding wear behavior of MDN 321 steel, $\text{Cr}_3\text{C}_2\text{-NiCr/Cenosphere/MoS}_2/\text{CaF}_2$, $\text{Cr}_3\text{C}_2\text{-NiCr/Cenosphere/MoS}_2/\text{CaSO}_4$, $\text{NiCrAlY/WC-Co/Cenosphere/MoS}_2/\text{CaF}_2$ and $\text{NiCrAlY/WC-Co/Cenosphere/MoS}_2/\text{CaSO}_4$ is carried out using high temperature pin on disc tribometer as outlined in ASTM G99-05 standard. All the four coatings

displayed a lower coefficient of friction and wear rate in comparison with the substrate. Excellent wear resistance of the coatings is attributed to the solid lubricants effect. Based on the wear rate data, the relative wear resistance of the coatings under dry sliding conditions is arranged in the following sequence:

$(\text{Cr}_3\text{C}_2\text{-NiCr/Cenosphere/MoS}_2/\text{CaSO}_4) > (\text{Cr}_3\text{C}_2\text{-NiCr/Cenosphere/MoS}_2/\text{CaF}_2) >$

$(\text{NiCrAlY/WC-Co/Cenosphere/MoS}_2/\text{CaSO}_4) > (\text{NiCrAlY/WC-Co/Cenosphere/MoS}_2/\text{CaF}_2)$

Higher wear resistance of $\text{Cr}_3\text{C}_2\text{-NiCr/Cenosphere/solid lubricant}$ coatings is attributed to the high hardness of $\text{Cr}_3\text{C}_2\text{-NiCr}$ which is incorporated in the coatings. Developed coatings in the present study exhibit higher temperature resistance to erosion, oxidation and wear as compared to MDN321 steel making them suitable for components subjected to elevated temperature service conditions.

Keywords: *Plasma spray; Fly ash cenosphere; Solid lubricants; Erosion; Oxidation; Wear; Elevated temperature.*

CONTENTS

Declaration	
Certificate	
Acknowledgment	
Abstract	
CONTENTS.....	i
LIST OF TABLES.....	ix
ABBREVIATIONS.....	x
1 INTRODUCTION.....	1
1.1 Thermal spray coatings.....	1
1.1.1 Plasma spray coatings.....	4
1.2 Coating materials.....	6
1.2.1 Fly ash as a coating material.....	8
1.2.2 Solid lubricants as coating materials.....	9
1.3 Literature survey.....	12
1.4 Objectives of the present work.....	24
1.5 Outline of the thesis.....	25
2 MATERIALS AND METHODS.....	26
2.1 Substrate.....	26
2.2 Coating feedstock.....	26
2.3 Plasma spraying.....	26
2.4 Porosity and density of the coatings.....	29
2.5 Surface roughness, microhardness and adhesion strength test.....	29
2.6 Microstructure and phase analysis.....	31
2.7 Solid particle erosion.....	31
2.8 Cyclic oxidation.....	34
2.9 Sliding wear.....	34
3 RESULTS AND DISCUSSION.....	36
3.1 Morphology of blended coating powders.....	36
3.2 Visual inspection of coated samples.....	38
3.3 Porosity and density of the coatings.....	39
3.4 Surface roughness, microhardness and adhesion strength.....	39

3.5	Surface morphology and cross sectional microstructure of the coatings	41
3.6	Phase analysis.....	47
3.7	Solid particle erosion studies.....	52
3.7.1	Erosion behaviour of MDN 321 steel substrate	52
3.7.2	Erosion behaviour of Cr ₃ C ₂ -NiCr/Cenosphere coating	58
3.7.3	Erosion behaviour of NiCrAlY/WC-Co/Cenosphere coating.....	65
3.7.4	Comparative discussion	73
3.8	Oxidation Studies	75
3.8.1	Visual observations	75
3.8.2	Thermogravimetric behaviour	75
3.8.3	XRD analysis	78
3.8.4	Surface and cross-sectional analysis of scale.....	78
3.8.5	Comparative discussion	81
3.9	Wear studies	83
3.9.1	MDN 321 steel substrate.....	83
3.9.2	Cr ₃ C ₂ -NiCr/Cenosphere/MoS ₂ /CaF ₂ and Cr ₃ C ₂ -NiCr/Cenosphere/MoS ₂ / CaSO ₄ coatings.....	88
3.9.3	NiCrAlY/WC-Co/Cenosphere/MoS ₂ /CaF ₂ and NiCrAlY/WC Co/Cenosphere/MoS ₂ /CaSO ₄ coatings	96
3.9.4	Wear mechanism.....	105
3.9.5	Comparative discussion	105
4	CONCLUSIONS.....	108
	SCOPE OF FUTURE WORK	111
	REFERENCES	112
	LIST OF PUBLICATIONS	124
	BIO-DATA	125

LIST OF FIGURES

Figure 1.1 Principle of thermal spray coating (Metco 2014).....	3
Figure 1.2 Schematic representation of plasma spray process (Tucker Jr 1994).....	5
Figure 1.3 Crystal structure of MoS ₂ (Erdemir 2001).....	10
Figure 2.1 Pycnometer.....	30
Figure 2.2 Surface roughness tester.....	30
Figure 2.3 Micro hardness tester.....	30
Figure 2.4 Universal testing machine.....	31
Figure 2.5 (a) Air jet erosion test machine (b) SEM micrograph of alumina erodent (c) schematic presentation of the test setup.....	32
Figure 2.6 3D optical non-contact profilometer.....	33
Figure 2.7 Tubular furnace.....	34
Figure 2.8 (a) Pin on disc tribometer setup (b) schematic representation of test setup....	35
Figure 3.1 Optical micrograph of MDN 321 steel substrate.....	36
Figure 3.2 Morphology of as blended (a) Cr ₃ C ₂ -NiCr/Cenosphere and (b) NiCrAlY/WC-Co/Cenosphere powders.....	36
Figure 3.3 Morphology of as blended (a) Cr ₃ C ₂ -NiCr/Cenosphere/MoS ₂ /CaF ₂ and (b) Cr ₃ C ₂ -NiCr/Cenosphere/MoS ₂ /CaSO ₄ powders.....	37
Figure 3.4 Morphology of as blended (a) NiCrAlY/WC-Co/Cenosphere/MoS ₂ /CaF ₂ (b) NiCrAlY/WC-Co/Cenosphere/MoS ₂ /CaSO ₄ powders.....	37
Figure 3.5 The camera photographs of (a) Cr ₃ C ₂ -NiCr/Cenosphere (b) NiCrAlY/WC-Co/Cenosphere (c) Cr ₃ C ₂ -NiCr/Cenosphere/MoS ₂ /CaF ₂ (d) Cr ₃ C ₂ -NiCr/Cenosphere/MoS ₂ /CaSO ₄ (e) NiCrAlY/WC-Co/Cenosphere/MoS ₂ /CaF ₂ and (f) NiCrAlY/WC-Co/Cenosphere/MoS ₂ /CaSO ₄ coatings.....	38
Figure 3.6 Fractured surfaces of (a) Cr ₃ C ₂ -NiCr/Cenosphere (b) NiCrAlY/WC-Co/Cenosphere (c) Cr ₃ C ₂ -NiCr/Cenosphere/MoS ₂ /CaF ₂ (d) Cr ₃ C ₂ -NiCr/Cenosphere/MoS ₂ /CaSO ₄ (e) NiCrAlY/WC-Co/Cenosphere/MoS ₂ /CaF ₂ and (f) NiCrAlY/WC-Co/Cenosphere /MoS ₂ /CaSO ₄ coatings.....	41

Figure 3.7 Surface morphology of Cr ₃ C ₂ -NiCr/Cenosphere coating along with the EDS composition analysis.	42
Figure 3.8 Surface morphology of NiCrAlY/WC-Co/Cenosphere coating along with the EDS composition analysis.	42
Figure 3.9 Surface morphologies of (a) Cr ₃ C ₂ -NiCr/Cenosphere/MoS ₂ /CaF ₂ (b) Cr ₃ C ₂ -NiCr/Cenosphere/MoS ₂ /CaSO ₄ (c) NiCrAlY/WC-Co/Cenosphere/MoS ₂ /CaF ₂ and (d) NiCrAlY/WC-Co/Cenosphere /MoS ₂ /CaSO ₄ coatings.....	43
Figure 3.10 Cross sectional SEM images of (a) Cr ₃ C ₂ -NiCr/cenosphere coating at lower magnification (b) circled area of (a) at higher magnification and (c) NiCrAlY/WC-Co/cenosphere coating at lower magnification (d) circled area of (c) at higher magnification.	44
Figure 3.11 Cross sectional SEM images of (a), (b) Cr ₃ C ₂ -NiCr/Cenosphere/MoS ₂ /CaF ₂ coating; (c), (d) Cr ₃ C ₂ -NiCr/Cenosphere/MoS ₂ /CaSO ₄ coating.....	46
Figure 3.12 Cross sectional SEM images of (a), (b) NiCrAlY/WC-Co/Cenosphere/MoS ₂ /CaF ₂ coating; (c), (d) NiCrAlY/WC-Co/Cenosphere/MoS ₂ /CaSO ₄ coating.....	47
Figure 3.13 XRD pattern of as blended powder and Cr ₃ C ₂ -NiCr/Cenosphere coating....	48
Figure 3.14 XRD pattern of as blended powder and NiCrAlY/WC-Co/Cenosphere coating.	48
Figure 3.15 XRD pattern of as blended powder and Cr ₃ C ₂ -NiCr/Cenosphere/MoS ₂ /CaF ₂ coating.....	50
Figure 3.16 XRD pattern of as blended powder and Cr ₃ C ₂ -NiCr/Cenosphere/MoS ₂ /CaSO ₄ coating.....	50
Figure 3.17 XRD pattern of as blended powder and NiCrAlY/WC-Co/Cenosphere/MoS ₂ /CaF ₂ coating.....	51
Figure 3.18 XRD pattern of as blended powder and NiCrAlY/WC-Co/Cenosphere/MoS ₂ /CaSO ₄ coating.....	51
Figure 3.19 Schematic diagram showing the erosion scar produced on typical eroded surface at (a) 30 and (b) 90° impact angles.	52
Figure 3.20 The camera photographs of the eroded MDN 321 steel at 600 °C with (a) 30 and (b) 90° impact angles.	53

Figure 3.21 Eroded surface 3-D profile of MDN 321 steel at (a) 200 (b) 400 and (c) 600 °C with 30° impact angle.	54
Figure 3.22 Eroded surface 3-D profile of MDN 321 steel at (a) 200 (b) 400 and (c) 600 °C with 90° impact angle.	55
Figure 3.23 (a) erosion rate and (b) volume loss of MDN 321 steel as a function of temperature at 30 and 90° impact angles.	56
Figure 3.24 Eroded surface SEM micrographs of MDN 321 steel at (a) 200 (b) 400 and (c) 600 °C with 30° impact angle.	57
Figure 3.25 Eroded surface SEM micrographs of MDN 321 steel at (a) 200 (b) 400 and (c) 600 °C with 90° impact angle.	58
Figure 3.26 The camera photographs of the eroded Cr ₃ C ₂ -NiCr/Cenosphere coating at 600 °C with (a) 30 and (b) 90° impact angles.	59
Figure 3.27 Eroded surface 3-D profile of Cr ₃ C ₂ -NiCr/Cenosphere coating at (a) 200 (b) 400 and (c) 600 °C with 30° impact angle.	60
Figure 3.28 Eroded surface 3-D profile of Cr ₃ C ₂ -NiCr/Cenosphere coating at (a) 200 (b) 400 and (c) 600 °C with 90° impact angle.	61
Figure 3.29 (a) erosion rate and (b) volume loss of Cr ₃ C ₂ -NiCr/Cenosphere coating as a function of temperature at 30 and 90° impact angles.	62
Figure 3.30 XRD pattern of eroded Cr ₃ C ₂ -NiCr/Cenosphere coating at different temperatures.	63
Figure 3.31 Eroded surface SEM micrographs of Cr ₃ C ₂ -NiCr/Cenosphere coating at (a) 200 (b) 400 and (c) 600 °C with 30° impact angle.	64
Figure 3.32 Eroded surface SEM micrographs of Cr ₃ C ₂ -NiCr/Cenosphere coating at (a) 200 (b) 400 and (c) 600 °C with 90° impact angle.	65
Figure 3.33 The camera photographs of the eroded NiCrAlY/WC-Co/Cenosphere coating at 600 °C with (a) 30 and (b) 90° impact angles.	66
Figure 3.34 Eroded surface 3-D profile of NiCrAlY/WC-Co/Cenosphere coating at (a) 200 (b) 400 and (c) 600 °C with 30° impact angle.	67
Figure 3.35 Eroded surface 3-D profile of NiCrAlY/WC-Co/Cenosphere coating at (a) 200 (b) 400 and (c) 600 °C with 90° impact angle.	68

Figure 3.36 (a) erosion rate and (b) volume loss of NiCrAlY/WC-Co/Cenosphere coating as a function of temperature at 30 and 90° impact angles.	70
Figure 3.37 XRD pattern of eroded NiCrAlY/WC-Co/Cenosphere coating at different temperatures.....	71
Figure 3.38 Eroded surface SEM micrographs of NiCrAlY/WC-Co/Cenosphere coating at (a) 200 (b) 400 and (c) 600 °C with 30° impact angle.....	72
Figure 3.39 Eroded surface SEM micrographs of NiCrAlY/WC-Co/Cenosphere coating at (a) 200 (b) 400 and (c) 600 °C with 90° impact angle.....	73
Figure 3.40 Erosion rate of MDN 321 steel, Cr ₃ C ₂ -NiCr/Cenosphere and NiCrAlY/WC-Co/Cenosphere coatings as a function of temperature at (a) 30 and (b) 90° impact angles.	74
Figure 3.41 The camera photographs of (a) MDN 321 steel (b) Cr ₃ C ₂ -NiCr/Cenosphere and (c) NiCrAlY/WC-Co/Cenosphere coatings subjected to cyclic oxidation at 600 °C in air for 20 cycles.....	76
Figure 3.42 Plot of oxidation cycles (a) weight gain per unit area (b) square of weight gain per unit area.....	77
Figure 3.43 XRD pattern of Cr ₃ C ₂ -NiCr/Cenosphere coating oxidized at 600 °C.....	78
Figure 3.44 XRD pattern of NiCrAlY/WC-Co/Cenosphere coating oxidized at 600 °C.	79
Figure 3.45 Surface morphology and EDS analysis of oxidized Cr ₃ C ₂ -NiCr/Cenosphere coating at 600 °C.....	79
Figure 3.46 Cross sectional X-ray mapping of oxidized Cr ₃ C ₂ -NiCr/Cenosphere coating at 600 °C.	80
Figure 3.47 Surface morphology and EDS analysis of oxidized NiCrAlY/WC-Co/Cenosphere coating at 600 °C.....	81
Figure 3.48 Cross sectional X ray mapping of oxidized NiCrAlY/WC-Co /Cenosphere coating at 600 °C.....	82
Figure 3.49 Friction coefficient of MDN 321steel at sliding velocity of 1.5 and 2.5 m/s with (a) 20 and (b) 40 N normal loads at 200, 400 and 600 °C.....	84
Figure 3.50 Wear rate of MDN 321 steel at sliding velocity of 1.5 and 2.5 m/s with (a) 20 and (b) 40 N normal loads at 200, 400 and 600 °C.	85

Figure 3.51 Worn surface SEM micrographs of MDN 321 steel with 1.5 m/s sliding velocity and 40 N normal load at (a) 200 (b) 400 and (c) 600 °C.	86
Figure 3.52 Worn surface SEM micrographs of MDN 321 steel with 2.5 m/s sliding velocity and 20 N normal load at (a) 200 (b) 400 and (c) 600 °C.	87
Figure 3.53 Friction coefficient of Cr ₃ C ₂ -NiCr/Cenosphere/MoS ₂ /CaF ₂ and Cr ₃ C ₂ -NiCr/Cenosphere/MoS ₂ /CaSO ₄ coatings at sliding velocity of 1.5 and 2.5 m/s with (a) 20 and (b) 40 N normal loads at 200, 400 and 600 °C.	89
Figure 3.54 Wear rate of Cr ₃ C ₂ -NiCr/Cenosphere/MoS ₂ /CaF ₂ and Cr ₃ C ₂ -NiCr/Cenosphere/MoS ₂ /CaSO ₄ coatings at sliding velocity of 1.5 and 2.5 m/s with (a) 20 and (b) 40 N normal loads at 200, 400 and 600 °C.	91
Figure 3.55 XRD pattern of worn out Cr ₃ C ₂ -NiCr/Cenosphere/MoS ₂ /CaF ₂ coating at 200, 400 and 600 °C.	92
Figure 3.56 XRD pattern of worn out Cr ₃ C ₂ -NiCr/Cenosphere/MoS ₂ /CaSO ₄ coating at 200, 400 and 600 °C.	92
Figure 3.57 Worn surface SEM micrographs of Cr ₃ C ₂ -NiCr/Cenosphere/MoS ₂ /CaF ₂ coating at (a) 200 (b) 400 (c) 600 °C and (d) opened cenosphere containing debris during wear test.	93
Figure 3.58 Worn surface SEM micrographs of Cr ₃ C ₂ -NiCr/Cenosphere/MoS ₂ /CaSO ₄ coating at (a) 200 (b) 400 (c) 600 °C and (d) opened cenospheres containing debris during wear test.	94
Figure 3.59 Post wear test photograph of (a) wear track on Al ₂ O ₃ disc and wear debris SEM micrographs of Cr ₃ C ₂ -NiCr/Cenosphere/MoS ₂ /CaF ₂ coating at (b) 200 (c) 400 and (d) 600 °C.	95
Figure 3.60 Friction coefficient of NiCrAlY/WC-Co/Cenosphere/MoS ₂ /CaF ₂ and NiCrAlY/WC-Co/Cenosphere/MoS ₂ /CaSO ₄ coatings at sliding velocity of 1.5 and 2.5 m/s with (a) 20 and (b) 40 N normal loads at 200, 400 and 600 °C.	97
Figure 3.61 Wear rate of NiCrAlY/WC-Co/Cenosphere/MoS ₂ /CaF ₂ and NiCrAlY/WC-Co/Cenosphere/MoS ₂ /CaSO ₄ coatings at sliding velocity of 1.5 and 2.5 m/s with (a) 20 and (b) 40 N normal loads at 200, 400 and 600 °C.	99
Figure 3.62 XRD pattern of worn out NiCrAlY/WC-Co/Cenosphere/MoS ₂ /CaF ₂ coating at 200, 400 and 600 °C.	100
Figure 3.63 XRD pattern of worn out NiCrAlY/WC-Co/Cenosphere/MoS ₂ /CaSO ₄ coating at 200, 400 and 600 °C.	101

Figure 3.64 Worn surface SEM micrographs of NiCrAlY/WC-Co/Cenosphere/MoS₂/CaF₂ coating at (a) 200 (b) 400 (c) 600 °C and (d) opened cenosphere containing debris during wear test. 102

Figure 3.65 Worn surface SEM micrographs of NiCrAlY/WC-Co/Cenosphere/MoS₂/CaSO₄ coating at (a) 200 (b) 400 (c) 600 °C and (d) opened cenosphere containing debris during wear test. 103

Figure 3.66 Post wear test photograph of (a) wear track on Al₂O₃ disc and wear debris SEM micrographs of NiCrAlY/WC-Co /Cenosphere/MoS₂/CaF₂ coating at (b) 200 (c) 400 and (d) 600 °C..... 104

Figure 3.67 Schematic diagram of the wear mechanism of Cr₃C₂-NiCr/Cenosphere/MoS₂/CaF₂ coating at different temperatures (a) start of wear test (b) wear surface at 200 °C (c) wear surface at 600 °C. 106

Figure 3.68 (a) friction coefficient and (b) wear rate of MDN 321 steel and coatings at 40 N normal load with 1.5 m/s velocity at 200, 400 and 600 °C temperatures. 107

LIST OF TABLES

Table 1.1 Literature review of erosion studies.....	13
Table 1.2 Review of oxidation studies.....	17
Table 1.3 Review of wear studies.	19
Table 2.1 Chemical composition (wt. %) of MDN 321 steel.	26
Table 2.2 Composition of powders.	27
Table 2.3 Mean particle size (μm) distribution of powders.....	27
Table 2.4 Composition of coating powders for erosion and oxidation test (wt. %).	28
Table 2.5 Composition of coating powders for wear test (wt. %).	28
Table 2.6 Plasma spray process parameters*.....	28
Table 2.7 Erosion test parameters.	33
Table 3.1 Porosity and density of the coatings.	39
Table 3.2 Surface roughness, microhardness and adhesion strength values.....	40
Table 3.3 EDS analysis of Cr_3C_2 -NiCr/Cenosphere coating at the designated point in Figure 3.6b.	45
Table 3.4 EDS analysis of NiCrAlY/WC-Co/Cenosphere coating at the designated point in Figure 3.6d.	45
Table 3.5 EDS analysis of wear debris of Cr_3C_2 -NiCr/Cenosphere/ MoS_2 / CaF_2 coating at 200, 400 and 600 °C.	96
Table 3.6 EDS analysis of NiCrAlY/WC-Co/Cenosphere/ MoS_2 / CaF_2 coating wear debris at 200, 400 and 600 °C.....	104

ABBREVIATIONS

Ag	: Silver
Al	: Aluminium
Al ₂ O ₃	: Aluminium Oxide
3Al ₂ O ₃ .2SiO ₂	: Mullite
APS	: Atmospheric Plasma Spray
ASTM	: American Society for Testing and Materials
Au	: Gold
BaF ₂	: Barium Fluoride
CaF ₂	: Calcium Fluoride
CaSO ₄	: Calcium Sulphate
Cr	: Chromium
Cr ₃ C ₂	: Chromium Carbide
Cr ₂ O ₃	: Chromium Oxide
Co	: Cobalt
COF	: Coefficient of Friction
EDS	: Energy Dispersive spectroscopy
HVOF	: High Velocity Oxy Fuel
MoS ₂	: Molybdenum disulfide
Ni	: Nickel
NiO	: Nickel Oxide
SEM	: Scanning Electron Microscope
TaS ₂	: Tantalum Sulfide

UTS : Ultimate Tensile Strength
WC : Tungsten Carbide
WO₃ : Tungsten Oxide
WS₂ : Tungsten disulfide
XRD : X-ray Diffraction

1 INTRODUCTION

Environmental degradation of metals and alloys due to service conditions is crucial that needs immediate attention which can minimize metal loss and failures therein to ensure safety and reliability. Gas and steam turbines, power generation boiler tubes, hot sections of aero engine, propulsion bearings, materials processing, and internal combustion engines suffer from surface friction, wear, erosion, oxidation and hot corrosion (Chen et al. 2013, Eriksson et al. 2015, Wang 2004, Zhen et al. 2017). These components need to possess excellent erosion, oxidation and wear resistance along with low friction coefficient in order to reduce energy consumption and noise levels (Bin et al. 2013). At present, Fe and Ti-based alloys used for such applications possess excellent strength and mechanical properties. Nevertheless, these alloys exhibit lower resistance to erosion, oxidation and wear.

In view of the quantum of loss due to erosion, oxidation, wear and corrosion, it becomes vital for an engineer to develop better resistance against such degradation by exploring the newer material system for the industrial service conditions. Materials working at elevated temperatures should have excellent resistance to wear and oxidation along with superior mechanical properties. However, only alloy development cannot provide the aforementioned properties. An alternate approach, where mechanical strength is accomplished by alloy development and wear or oxidation resistance by surface modifications using different coating methodologies is a widely accepted practice in aforementioned applications. Among the various coating methods, thermal spray coatings are gaining increasing popularity as compared to the other types, particularly for turbine and elevated temperature applications.

1.1 Thermal spray coatings

Thermal spray coating technique is versatile and widely used due to its adaptability with a variety of coating materials. Thermal spray empowers the coating materials to be deposited on the surface of large parts, which is difficult to produce by powder metallurgy for technical and economic reasons (Berger 2015). In thermal spray coatings, the coating

material is in the form of powder, wire or rod which is heated to above or near to its melting point and directed towards the substrate. The molten or semi-molten droplets impacts on the substrate with high energy with a negligible rise in substrate temperature and forms a lamellar structure with high coating density and hardness as shown in Figure 1.1. Almost any material that can be melted without decomposing can be used to form the coating and has the ability to deposit coatings with thicknesses ranging from several micrometers to several millimeters. The substrate, for most applications, is not heated above 150 °C, thereby metallurgical properties remain unchanged.

The bond between the sprayed coating and the substrate is primarily mechanical in nature (Bunshah 1994). The quality of the coatings obtained by thermal spray techniques is dependent on the nature of the coating process and the processing parameters. Cost/performance ratio of these coating are lower making them suitable for a variety of applications. These coatings are also suitable for components repairs as it does not alter the microstructure of substrates (Santa et al. 2009).

Advanced thermal spray coatings which have been used in industries for many years are enlisted below:

- Flame Spray
- Electric Arc Spray
- Plasma Spray
- Detonation Gun Spray
- High Velocity Oxy Fuel Spray (HVOF)

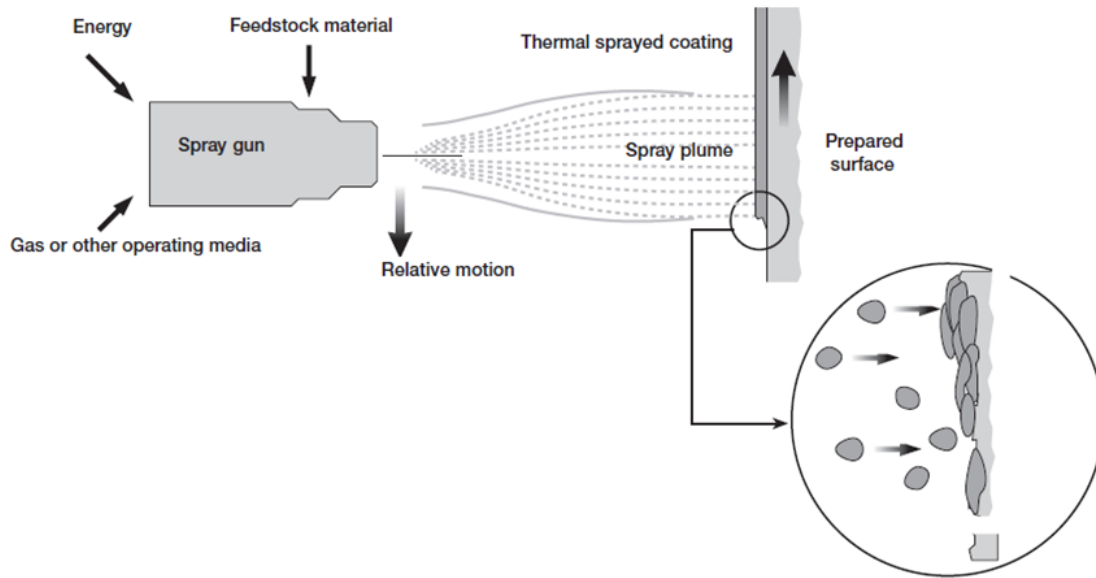


Figure 1.1 Principle of thermal spray coating (Metco 2014).

Applications of Thermal Spray Coatings

Thermal spray coatings are used in wide variety of application having a focus on enhancing wear, erosion, oxidation and corrosion resistance of the surface. These are also used for dimensional restoration, as a thermal barrier, thermal conductors, electrical conductors or insulators and to enhance or retard radiation (Tucker Jr 1994). Among other applications thermal spray coatings are also used as/in:

- an alternative to hard chromium plating to resist wear and corrosion
- medical implants such as artificial hip joints
- textile industry
- gas turbines
- automotive industry
- printing industry
- pump housings & impellers

Among the available thermal spray coating processes, plasma spray technique is considered as most versatile, flexible and cost effective solution for various industrial applications (Fauchais et al. 1997). Plasma spray process can be used to deposit the coatings for the applications in areas of wear, erosion and corrosion protection owing to its higher operating temperature (Singh et al. 2012).

1.1.1 Plasma spray coatings

Plasma spray process belongs to the family of thermal spray coating techniques. In this process, a wide variety of materials like metallic, non-metallic and ceramics can be coated in a molten or semi-molten state on the substrate by utilizing thermal energy (Fauchais et al. 2001). It works on the principle that, high energy spark produced between cathode and anode due to the potential difference in the energy source. Schematic representation of plasma spray process is shown in Figure 1.2. Tungsten is used as cathode and copper as an anode. The inert gases, usually argon (Ar), helium (He), or nitrogen (N₂) or mixtures of these, are used as plasma generating gases. When the gas is introduced between the two electrodes is get ionized due to reactions between the electrons from the cathode source thus, creating the plasma state. The gases are heated as they pass through the arc, they expand radially and axially, and accelerate through the nozzle exit with a typical flow rate of 3.5 liters/min (Sidky and Hocking 1999). The temperature in the core region can reach values of more than 10000 °C due to the heat released and radiation effects. The arc temperature is in the range of 6000-12000 °C (Tucker Jr 1994).

In the early fifties of the twentieth century, the plasma torches are developed to test materials at high enthalpies for simulated re-entry vehicles. In the late fifties and early sixties, the first serious attempts are reported on using plasma torches for spraying of primarily refractory materials. Using this process almost any material can be coated on almost any type of substrate. This flexibility of plasma spray technology is the key factor in its rapid development (Pfender 1988). Very high melting point materials like ceramic, cermets and refractory alloys can be deposited due to its high temperatures. Materials can be processed as long as there is a temperature difference of at least 27 °C between the

melting temperature and decomposition or evaporation temperature (Fauchais 2004). Depending upon the applications various types of plasma spray techniques are used and are listed below:

- Atmospheric Plasma Spraying (APS)
- Vacuum Pressure Plasma (VPS) or Low-Pressure Plasma Spraying (LPPS)
- Shrouded Plasma Spraying (SPS)
- Controlled Atmosphere Plasma Spraying (CAPS)

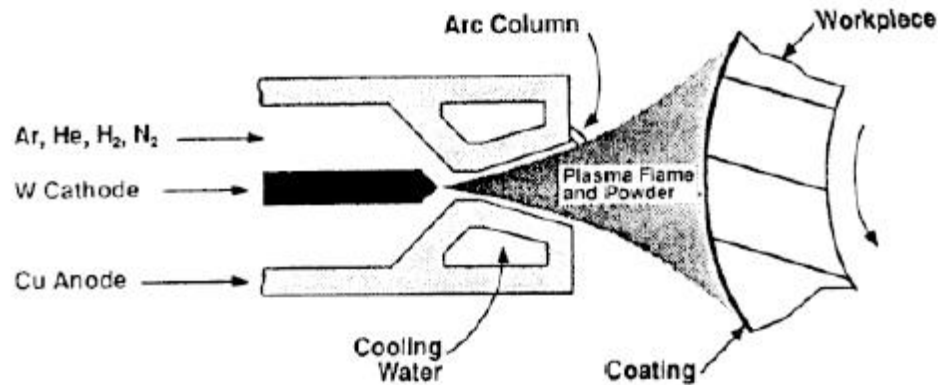


Figure 1.2 Schematic representation of plasma spray process (Tucker Jr 1994).

Plasma technique is proficient in developing the coatings of more than 100 μm with higher production rates without affecting the mechanical properties of the substrate (Yoshida 1993). Probable disadvantages associated with this process are higher porosity and poor adhesion, specifically for coating of ceramics on metals. Further, better adhesion strength can be achieved using bond coat layer and /or powder of small particle size. Plasma spray technique is also capable of forming microstructures with fine, non columnar and equiaxed grains, ability to produce homogeneous coatings without a change in composition with thickness and ability to deposit materials in almost any environment.

Applications of plasma spraying include wear, erosion, oxidation, corrosion, abrasion resistant coatings and production of monolithic and near net shape shapes, which at the same time take advantage of the rapid solidification process. It can also be used in the

reclamation of worn out components, production of aerospace and nuclear power components. Plasma spraying is also used for producing hydroxyapatite coatings onto the stems of orthopedic endo prostheses (William et al. 2003). Powder of glassy metals can be plasma sprayed without changing their amorphous characteristics. High-temperature superconductive materials have also been deposited by the plasma spray process (Pfender 1988). High-temperature applications like diesel engines, aircraft engines, and land-based gas turbines are plasma sprayed to protect the component from wear, oxidation and corrosion (Niranatlumpong et al. 2000).

1.2 Coating materials

Wide varieties of coating materials are available which can be used in the form of powder, wire, and rod. Selection of coating materials depends on the application, operating environments like temperature, corrosive medium etc. In modern industrial turbines, the inlet temperature exceeds 900 °C with component life expectancy to the order of 25,000-50,000 hours (Choudhury and Bhakta 1996). It is almost impossible for a monolithic material to have properties to withstand such extreme service conditions (Sidhu et al. 2006). The chosen coating materials should possess high-temperature stability and resistance to wear, erosion and oxidation.

MCrAlY (where M represents nickel, cobalt, or a combination of Ni and Co) with optimum amounts of Al and Cr powders possess excellent corrosion and oxidation resistance and are being extensively used for high-temperature applications (Seo et al. 2008). However, MCrAlY coatings are not used as a primary coating in the industry due to poor resistance to wear owing to their lower hardness as compared to carbides, ceramics, and oxides. Nevertheless, wear resistance of these coatings can be significantly improved by reinforcing the hard phases like WC, Al₂O₃, Cr₃C₂, and Cr₂O₃ in the Ni or Co matrix (Bin et al. 2013, Wang and Chen 2003).

WC-Co based cermet coatings possess an excellent combination of high hardness, wear and erosion resistance, high elasticity and chemical inertness. These unique properties of WC-Co coatings can be utilized to improve the wear resistance of engineering components (Jafari et al. 2013). WC is usually combined with other metals, such as cobalt or nickel to form a composite powder for enhanced wear and corrosion resistance. In WC-Co coatings Co is used as the matrix material and it affects the hardness of the coating. Increase in the Co content decreases the hardness of the coating (Wood 2010). However, WC-Co coatings exhibit a higher friction coefficient and provide lower protection for opposing surfaces. This can be overcome by adding suitable solid lubricants in the coatings.

Cr_3C_2 -NiCr coatings are commonly used in high temperature erosion, wear and corrosion resistive applications. Carbide particles embedded in NiCr matrix impart high hardness and strength up to 900 °C. Further, coefficient of thermal expansion of Cr_3C_2 ($10.3 \times 10^{-6} \text{ }^\circ\text{C}^{-1}$) is closer to iron ($11.4 \times 10^{-6} \text{ }^\circ\text{C}^{-1}$) and Ni ($12.8 \times 10^{-6} \text{ }^\circ\text{C}^{-1}$) which are the base alloys for high temperature applications. Such a composition if chosen, thermal mismatch in high temperature environment can be minimized to a great extent (Guilemany et al. 2002, Manjunatha et al. 2014, Yang et al. 2008). However, the Cr_3C_2 -NiCr coatings possess higher frictional coefficient to the counter bodies during prolonged sliding conditions leading to higher wear rates, limiting their application on high speed rotating devices. Incorporating solid lubricants in Cr_3C_2 -NiCr coatings lowers the friction coefficient and wear rate (Huang et al. 2009).

Oxide ceramics such as alumina, zirconia, titania, chromia, silica and yttria are used extensively as coating materials to improve wear, erosion, cavitation, fretting and corrosion resistance. They are especially useful in applications where wear and corrosion resistance are required simultaneously (Zavareh et al. 2015). For mass scale adaptability, material cost needs to be looked into carefully. Exploiting naturally available environmental pollutant like fly ash can be an option for developing cost-effective coating solutions.

1.2.1 Fly ash as a coating material

Fly ash is a richly accessible industrial waste, generated because of combustion of coal in thermal power plants. It is a predominantly inorganic residue obtained from the flue gases of furnaces at pulverized coal power plants. When coal is burnt in pulverized coal boilers, the minerals entrained in the coal are thermally transformed into chemical species that are reactive or could be chemically activated. These fly ash cenospheres are spherical in shape, readily available in powder form, inexpensive and possess superior mechanical properties (Bharath Kumar et al. 2016 A, Bharath Kumar et al. 2016 B, Manakari et al. 2015, Zeltmann et al. 2016). Oxides of silicon (SiO_2), aluminum (Al_2O_3) and mullite ($3\text{Al}_2\text{O}_3 \cdot 2\text{SiO}_2$) are the main compositions of cenospheres (Bharath Kumar et al. 2016 C, Doddamani et al. 2015). Among them, aluminum oxide and mullite exhibits high-temperature stability, wear, erosion and corrosion resistance (Arizmendi-Morquecho et al. 2012, Das et al. 2005).

There are two primary sources of fly ash: pulverized coal power plant and a municipal waste incineration plant. Fly ash produced from the burning of pulverized coal in a coal-fired boiler is a fine-grained, powdery particulate material that is carried off in the flue gas and usually collected from it by means of electrostatic precipitators, baghouses or mechanical collection devices such as cyclones. India is producing about 165 million tons fly ash per year from coal based thermal power plants, out of that only 100 million tons fly ash is being utilized. Fly ash is a major issue as electricity generation in India would remain largely coal-based for a couple of coming decades. Fly ash generated in the year 2016-2017 is 169 million tons (CEA 2017). The disposal of such a large amount of fly ash is a challenging task. At present it is being disposed of in ash ponds occupying large areas of land and about 1,00,000 acres of land is buried under these ash ponds.

Many researchers have studied the utilization of fly ash as a coating material. Mishra et al. (2000) studied the utilization of fly ash as a coating material on steel and aluminum substrates using plasma spray technique. They found that fly ash can be effectively used as

a coating material for thermal spray coatings. They also reported that fly ash can be mixed with other metal to get the desired properties. Aluminum pre-mixed with fly ash has shown better adhesion strength as compared to fly ash alone. Incorporation of these inexpensive hollow cenospheres in the coatings might effectively reduce the wear by opening up the built-in porosity which may act as localized regions for wear debris accumulation.

The available studies on fly ash cenosphere composite coatings for high-temperature application are relatively scarce. Furthermore, understanding the wear behavior of these fly ash cenospheres is an interesting and worth investigating task.

1.2.2 Solid lubricants as coating materials

Solid lubricants are used in case of oil and grease failure under higher loads, extreme temperature, high vacuum and adverse environments (Martin Jr 1972). Solid lubricants can be used as powders that can be directly applied to the surfaces, bonded films, as additives in the oils and grease and also on the integral part of the composites and coatings. Commonly available solid lubricants are transition metal disulfides (MoS_2 , WS_2 , TaS_2), soft noble metals (Au, Ag), inorganic fluorides (CaF_2 , BaF_2) and metal oxides (NiO , Cr_2O_3). Majority of these solid lubricants exhibit their lubricity due to a lamellar or layered crystal structure. A few others (soft metals, polytetrafluoroethylene, certain oxides, rare-earth fluorides, diamond, and diamond-like carbons, fullerenes) can also provide lubrication although they do not have a layered crystal structure (Erdemir 2001). These lubricants are classified based on the chemistry, crystal structure and lubricity as (Erdemir 2001):

- ✓ Lamellar Solid Lubricants
- ✓ Soft metals
- ✓ Mixed oxides
- ✓ Single oxides
- ✓ Halides and sulfates of alkaline earth metals
- ✓ Carbon-based solids

MoS₂ belongs to the family of transition metal dichalcogenides having layered crystal structure. Atoms or molecules are present in the layer having a strong attraction between them and is called a layer lattice crystal structure. The distance between the successive layers is more as compared to atoms. Layers shear parallel more easily than across and are represented in Figure 1.3. Thereby it supports relatively heavy loads at a right angle to the layers while still being able to slide in parallel. This property is being effectively used for lubrication process (Brudnyi and Karmadonov 1975). It exhibits low co-efficient of friction both in vacuum and atmosphere making them most suitable for dry sliding wear application providing lubrication up to 350 °C. However, temperatures above 500 °C, MoS₂ and other layered solid lubricants tend to oxidize resulting in lubricity loss (Zhang et al. 2009).

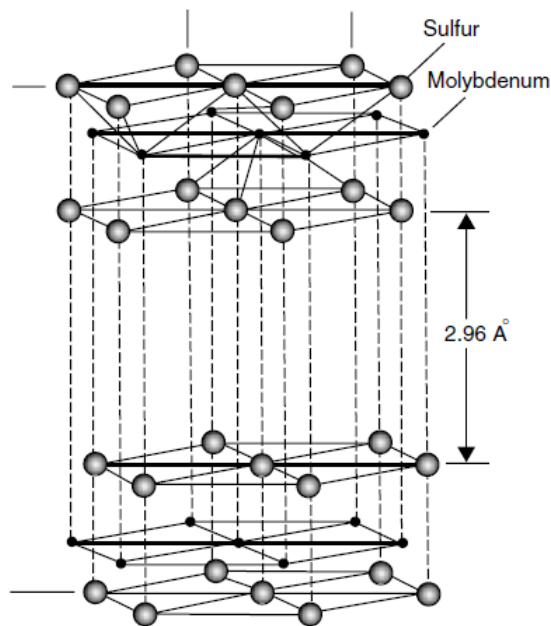


Figure 1.3 Crystal structure of MoS₂ (Erdemir 2001).

Inorganic fluorides and sulfates such as CaF₂, BaF₂, and CaSO₄ provide lubrication at elevated temperature (> 500 °C) due to their low shear strength at higher temperatures (Bi et al. 2013, Sliney 1969). However, the sole lubricant may not provide the lubrication over

a wide range of operating temperatures. Therefore incorporating high and low-temperature solid lubricants in the coatings may yield the synergetic effect over the wide temperature range (Baker et al. 2007, Chen et al. 2012). Some of the advantages and disadvantages of the solid lubricants are listed below:

Advantages:

- No contamination by dust particles.
- Stable at a higher temperature, cryogenic temperature, and high-pressure environments.
- Lubricate extremely well in high vacuum and have a very low vapor pressure.
- Longer shelf life.
- Less Number of parts in the components due to the elimination of oil seal and pumps.

Disadvantages:

- Friction coefficient is generally higher as compared to other lubricants.
- Solid lubricants cannot act as coolants compared to liquid lubricants.
- Lubrication effect in coatings is finite.
- Solid lubricants have little or no damping effect.

Many researchers effectively utilized the high-temperature performance of these solid lubricants as a coating material to improve the tribological properties at elevated temperatures (Huang et al. 2009, Kim et al. 2005, Zhang et al. 2009). Solid lubricants BaF₂/CaF₂ eutectic can significantly improve the tribological behavior of wear-resistant hard coatings due to its lower melting point and shear strength as compared to a single fluoride and its capability to sustain elevated temperatures (Huang et al. 2009).

However, these metallic, carbide and solid lubricant powders are the quite expensive demanding development of coatings consists of low-cost powders such as fly ash

cenospheres. Usage of such environmental pollutants in coatings might further reduce landfill burden and if developed successfully are eco-friendly as well.

1.3 Literature survey

Thermal spray coatings are used to enhance the elevated temperature wear, erosion and oxidation resistance of the materials. Selection of the coating materials is the key factor in the thermal spray coatings. Carbides, oxides, and ceramics are the promising materials for erosion, oxidation and wear resistant coatings. Coatings with solid lubricants show better wear resistance at elevated temperatures. A number of reviews dealing with various coating materials for developing erosion, wear and oxidation resistance through thermal spray coatings have been published in recent years and are presented in Table 1.1 to Table 1.3.

Table 1.1 Literature review of erosion studies.

Author	Coating material	Coating type	Remarks
Xia et al. (1999)	Cr ₃ C ₂ /NiCr, ZrO ₂ /NiCr, WTiC ₂ /NiCr, and X40	Plasma spray on the mild steel	<ul style="list-style-type: none"> • X40 coating showed better erosion resistance as compared to mild steel substrate at all the test conditions. • Cr₃C₂/NiCr coating displayed less erosion resistance as compared to the substrate at room temperature and 90° impact angle.
Hoop and Allen (1999)	88%WC- 12%NiCr, 88%WC-12% Ni, 75%Cr ₃ C ₂ -25% NiCr,	Plasma spray on the HFS620 boiler steel	<ul style="list-style-type: none"> • 88%WC-12%NiCr, 88%WC-12%Ni, 75%Cr₃C₂-25%NiCr coatings registered lower erosion rate as compared to boiler steel. • 60-70% decrease in the erosion rate of the 88%WC-12%NiCr coating as compared to boiler steel.
Wang and Verstak (1999)	Cr ₃ C ₂ /TiC– NiCrMo, Cr ₃ C ₂ -25Ni44CrSi, WC-17Co	HVOF on the mild steel	<ul style="list-style-type: none"> • 50-60% and 30-40% decrease in the thickness loss of the Cr₃C₂/TiC–NiCrMo coating as compared to Cr₃C₂-25Ni44CrSi coating at 300 °C test temperature and at all test impact angles.
Wang (2003)	FeB, FeBSiAlC, Fe39Cr5C, Fe27Cr3B2Si,	High velocity continuous combustion (HVCC) on the mild steel.	<ul style="list-style-type: none"> • FeB, FeBSiAlC coatings exhibited less thickness loss as compared to Fe39Cr5C, Fe27Cr3B2Si coatings. • 40-50% decrease in the thickness loss of the sealed and heat treated FeB coating as compared to Fe39Cr5C, Fe27Cr3B2Si coatings.

Vicenzi et al. (2006)	WC-12Co, Cr ₃ C ₂ -NiCr and WC-CrC-Ni	HVOF on the SAE 1020 steel	<ul style="list-style-type: none"> All the coatings showed higher erosion resistance as compared SAE 1020 steel. WC-12Co exhibited less thickness loss as compared to other coatings which are 90-95% lower than the SAE 1020 steel.
Ji et al. (2007)	Cr ₃ C ₂ -NiCr	HVOF on the mild steel	<ul style="list-style-type: none"> The orthogonal regression experimental design method is used to study the effect of spray parameters on the erosion performance. The effect of spray parameters on the erosion performance is studied. The flow rate of propane and oxygen gases influences erosion rate of the coatings.
Wang et al. (2007)	NiAl intermetallic with 2%, 5% and 8% CeO ₂	HVOF on the mild steel	<ul style="list-style-type: none"> Erosion rate of the coating increased with increase in the CeO₂ and increase in heat treatment temperature. 2% CeO₂ registered less erosion rate which is 60-70% less than the other coatings.
Yang et al. (2008)	Cr ₃ C ₂ -NiCr	HVOF on the mild steel	<ul style="list-style-type: none"> Erosion rate of the steel increased with increase in the test temperature for 30 and 90° impact angles. Erosion rate of coating not changed with a change in the temperature at 30° impact angle. 60-70% decrease in the erosion rate of the coating as compared to the steel.

Luo et al. (2010)	FeMnCr/Cr ₃ C ₂ , FeMnCr8Al/Cr ₃ C ₂ , FeMnCr15Al/Cr ₃ C ₂	High velocity arc spraying on steel	<ul style="list-style-type: none"> Erosion rate increased with increase in the impact angle. FeMnCr15Al/Cr₃C₂ coating displayed less erosion rate which is 40-50% lower than the FeMnCr/Cr₃C₂ and FeMnCr8Al/Cr₃C₂ coatings.
Bonache et al. (2011)	WC-12Co micrometric and nanometric powder	Atmospheric Plasma Spraying on the mild steel	<ul style="list-style-type: none"> Effects of plasma intensity and particle size on the erosion resistance are studied. Erosion resistance of the micrometric coatings decreased with an increase in the plasma intensity at 45° impact angle. Nano metric coatings showed less erosion resistance which is 10-15% less than the micrometric coatings
Kaur et al. (2012)	75Cr ₃ C ₂ -25(NiCr)	HVOF on the ASTM SA213-T22 boiler steel	<ul style="list-style-type: none"> Extreme cracking and spalling are observed in T22 boiler steel during the study whereas coating showed no such spallation. Thickness loss of the coating is 0.03 mm which is 25-30% lower than the boiler steel.
Sharma (2012)	NiCrFeSiB	Flame spray on low carbon steel	<ul style="list-style-type: none"> Erosive wear increased with increase in the velocity and temperature. Erosive wear of the coating is 40-50% less than the substrate.
Mishra et al. (2013)	NiCrAlY	Plasma spray on the Superni 75, Superni 600, Superni 718 and Superfer 800H	<ul style="list-style-type: none"> The coating on superni 600 and superfer 800H exhibited weight loss whereas coating on superni 75 and 718 showed weight gain. Coated superni 75 super alloy exhibited less weight loss which is 30-40% less than the other super alloys.

Manjunatha et al. (2014)	$\text{Cr}_3\text{C}_2\text{-NiCr}$	HVOF on AISI 316 molybdenum steel	<ul style="list-style-type: none"> • Coating displayed higher erosion rate at 75° impact angle and lower erosion rate at 90° impact angle. • 15-20% decrease in the erosion rate of the $\text{Cr}_3\text{C}_2\text{-15NiCr}$ coating as compared to $\text{Cr}_3\text{C}_2\text{-10NiCr}$ and $\text{Cr}_3\text{C}_2\text{-5NiCr}$ coatings.
Praveen et al. (2015)	$\text{NiCrSiB-Al}_2\text{O}_3$	Plasma spray on AISI 304 substrate	<ul style="list-style-type: none"> • Coating presented better resistance to erosion at 30° impact angle as compared with 90° due to the pinning and shielding effect of the alumina particle. • Coating exhibited better erosion resistance at 30° impact angle which is 2.5 times higher than substrate.
Sharma and Goel (2016)	WC-10Co-4Cr	HVOF on cast and solution treated 23-8-N nitronic steel substrates	<ul style="list-style-type: none"> • Coated 23-8-N nitronic steel substrate exhibited resistance to erosion owing to a combination of high fracture toughness and high hardness of coating as a result of high amount of WC retention.

Table 1.2 Review of oxidation studies.

Author	Coating material	Coating type	Remarks
Sidhu et al. (2006)	Cr ₃ C ₂ -NiCr	HVOF on superni 75	<ul style="list-style-type: none"> • Cr₃C₂-NiCr coating is resistant to hot corrosion in the given molten salt environment at 900 °C. • 70% reduction in the weight gain of the coating as compared to superni 75 substrates.
Seo et al. (2008)	NiCrAlY	Vacuum plasma spray on Inconel 718	<ul style="list-style-type: none"> • NiCrAlY coating registered better isothermal oxidation as compared to Inconel 718. Square of weight gain of coating is around 90% lower than the Inconel 718. • Surface roughness of the coating is decreased after isothermal exposure due to growth of oxide scales.
Kaur et al. (2009)	Cr ₃ C ₂ -NiCr	HVOF on SAE-347H boiler steel	<ul style="list-style-type: none"> • Coating registered higher oxidation and corrosion resistance as compared to substrate which is ascribed to the formed chromium rich oxide scale at elevated temperature.
Somasundaram et al. (2014)	WC-Co/NiCrAlY	HVOF on MDN 310 and superfer 800	<ul style="list-style-type: none"> • Both oxidation and hot corrosion resistance of the coating are higher than the substrates. The coating on superfer substrate showed better results as compared to coated MDN 310 steel. • Square of weight gain of coated superfer substrate registered 65 % less square of weight gain as compared to uncoated superfer substrate.

Jegadeeswaran et al. (2014)	25% $[\text{Cr}_3\text{C}_2-25(\text{Ni}20\text{Cr})]$ + 75% NiCrAlY	HVOF on Ti-31 alloy	<ul style="list-style-type: none"> • 25% $[\text{Cr}_3\text{C}_2-25(\text{Ni}20\text{Cr})]$ + 75% NiCrAlY coating displayed less weight gain which is 95 % lower than Ti-31 alloy. • The superior oxidation resistance of 25% $[\text{Cr}_3\text{C}_2-25(\text{Ni}20\text{Cr})]$ + 75% NiCrAlY is attributed to the thick protective oxide scale developed on the surface.
Singh et al. (2016)	$\text{Cr}_3\text{C}_2\text{-NiCr}$ and $\text{Cr}_3\text{C}_2\text{-NiCr}/25$ WC-Co	HVOF on ASTM SA213-T22 steel	<ul style="list-style-type: none"> • $(\text{Cr}_3\text{C}_2\text{-NiCr}) + 25\%$ (WC-Co) coating displayed better results in all the three environments as compared to stand-alone $\text{Cr}_3\text{C}_2\text{-}25(\text{NiCr})$ coating which showed 80% less weight gain than $\text{Cr}_3\text{C}_2\text{-}25(\text{NiCr})$ coating. • A simultaneous formation of protective phases such as Cr_2O_3, NiCr_2O_4, and NiWO_4 as strong phases have contributed the best properties to the coating.
Zhou et al. (2017)	$\text{Cr}_3\text{C}_2\text{-}25(\text{NiCr})$ and $\text{Cr}_3\text{C}_2\text{-WC-NiCoCrMo}$	HVOF on Inconel 625 plates	<ul style="list-style-type: none"> • The $\text{Cr}_3\text{C}_2\text{-WC-NiCoCrMo}$ and $\text{Cr}_3\text{C}_2\text{-NiCr}$ coatings registered similar levels of oxidation resistance. • $\text{Cr}_3\text{C}_2\text{-WCNiCoCrMo}$ coating demonstrated better corrosion resistance to that of the $\text{Cr}_3\text{C}_2\text{-NiCr}$ coating. • The corroded scale of the $\text{Cr}_3\text{C}_2\text{-WC-NiCoCrMo}$ coating is almost one-third less thick than the $\text{Cr}_3\text{C}_2\text{-NiCr}$ coating.

Table 1.3 Review of wear studies.

Author	Coating Material	Coating Type	Remarks
Li and Ding (2000)	Cr ₃ C ₂ -NiCr/ Ni, Ni-Co, Ni-Mo	Plasma spraying followed by electroless plating on 1Cr18Ni9Ti	<ul style="list-style-type: none"> Electroless plated Ni-based coatings improved the tribological properties of the Cr₃C₂-NiCr coating. 70-80% decrease in the COF of the Ni-based alloy coatings as compared to Cr₃C₂-NiCr coating.
Ouyang et al. (2001)	ZrO ₂ -CaF ₂ -Ag ₂ O (ZFA) and Ytria partially stabilized zirconia (YSPZ)	Low-pressure plasma-spray on carbon steel	<ul style="list-style-type: none"> ZFA coating presented lower friction and wear rate at room temperature, 200 and 800 °C. Ag₂O provided lubrication at 300-400 °C and CaF₂ at 600-700 °C. 30-40% decrease in the COF of the coatings as compared to YSZ coatings at 300-700 °C.
Guilemany et al. (2002)	Cr ₃ C ₂ -NiCr	HVOF on low carbon steel	<ul style="list-style-type: none"> 5-10% decrease in the volume loss of the heat treated coatings in an oxidizing atmosphere. 40-50% decrease in the volume loss of the heat treated coatings in an inert atmosphere.
Sahraoui et al. (2003)	Cr ₃ C ₂ -NiCr and WC-Co	HVOF on 25CD4 disc	<ul style="list-style-type: none"> Coatings displayed higher hardness and high volume fraction of carbides being retained during the coating process. WC-Co coating exhibited higher wear resistance and it is 60-70% lower as compared to Cr₃C₂-NiCr coating.
Krishna et al. (2003)	Fly ash	Detonation Spray on mild steel	<ul style="list-style-type: none"> Fly ash coatings exhibited low COF (0.26) which is 60-70% lower as compared to mild steel. 30% increase in the weight loss of the fly ash coatings as compared to mild steel.

Picas et al. (2003)	CrC–NiCr and nanocrystalline CrC–NiCr	HVOF on steel substrate	<ul style="list-style-type: none"> • The decrease in the size of the feedstock powder lowered the surface roughness of the coatings. • Nano structured CrC60–NiCr40 coating exhibited less COF of 0.13 and specific wear rate of $3.5 \times 10^{-15} \text{ m}^3/\text{Nm}$ at 40 N applied load as compared to CrC75–NiCr25 coating.
Wang et al. (2005)	FeS	Plasma spray on AISI 1045 steel	<ul style="list-style-type: none"> • Coating is carried out with three different coating thickness of 0.3, 0.8 and 1.5 mm. The 0.8 mm thick coatings displayed better tribological properties as compared to others. • Coating exhibited superior tribological properties as compared to AISI 1045 steel. • 25-30% decrease in the COF of the coating as compared to plain steel under oil lubrication at room temperature.
Tsunekawa et al. (2006)	Cast iron/h-BN	Plasma spray on aluminum alloy	<ul style="list-style-type: none"> • 5-10% decrease in the COF of Cast iron/h-BN coating as compared to cast iron coatings under a paraffin-based oil condition in an air atmosphere.
Yang et al. (2006)	WC–12% Co	HVOF on steel	<ul style="list-style-type: none"> • Wear rate of the coating decreased with increase in the test temperature. • 60-70% decrease in the wear rate of the coatings at 300 °C as compared to room temperature.

Zhang et al. (2007)	Cr ₃ C ₂ -NiCr La ₂ O ₃ , CeO ₂	Supersonic plasma spray on 2Cr13 stainless steel	<ul style="list-style-type: none"> • 5-10% decrease in the COF of the coatings containing La₂O₃, CeO₂ as that of the Cr₃C₂-NiCr coating. • 90-95% decrease in the volume loss of the coatings containing 2% and 4% La₂O₃.
Sidhu et al. (2007)	Fly ash	Shrouded plasma spray on low carbon steel	<ul style="list-style-type: none"> • Wear rate of the coating is increased with increase in the load. • Wear rate of the coating is 2.5 times more than that of the steel at 10 N load. • Coating exhibited better oxidation and salt corrosion resistance due to the presence of alumina and silica in the fly ash.
Du et al. (2010)	NiCr clad BaF ₂ /CaF ₂ /NiCr-Cr ₃ C ₂	Plasma spray on low carbon steel	<ul style="list-style-type: none"> • 20% decrease in the COF of the NiCr/Cr₃C₂-10%BaF₂/CaF₂ coating as compared to the NiCr/Cr₃C₂ in the temperature region between 500-800 °C. • 40% decrease in the wear rate of the NiCr/Cr₃C₂-10%BaF₂/CaF₂ coating as compared to the NiCr/Cr₃C₂ in the temperature region between 500-800 °C.
Ozdemir et al. (2010)	Al-12Si/TiB ₂ /h-BN	Plasma spray on aluminum alloy	<ul style="list-style-type: none"> • 5-10% decrease in the COF of the coating as compared to aluminum alloy substrate at 10 N loads using Al₂O₃ as a counter ball. • 70-80% decrease in the volume loss of a coating as compared to the substrate.

Yuan et al. (2010)	WC-Co-Cu-BaF ₂ /CaF ₂	Atmospheric plasma spray on mild steel	<ul style="list-style-type: none"> • WC-Co coatings without solid lubricant exhibited the highest steady-state COF of about 0.38 at room temperature. • Coatings with 10 weight % Cu and 10 weight % BaF₂/CaF₂ solid lubricants displayed the lowest steady-state COF about 0.02 at room temperature. • Wear rate of WC-Co is higher ($(25.7 \pm 2.8) \times 10^{-5} \text{mm}^3 \text{N}^{-1} \text{m}^{-1}$) than that of 80W10C10F coating ($(1.3 \pm 0.03) \times 10^{-5} \text{mm}^3 \text{N}^{-1} \text{m}^{-1}$).
Bin et al. (2013)	Graphite/CaF ₂ /TiC/Ni	Plasma spray on 45 carbon steel	<ul style="list-style-type: none"> • COF of composite coatings are in the range of 0.22–0.288, which are reduced by 25.9 to 53% as compared to pure Ni-base alloy coatings • Wear rates of the composite coatings are 18.6-70.1% less as compared to pure Ni-base alloy coatings.
Chen et al. (2013)	NiCrAlY-Ag-Mo	Atmospheric plasma spray on Stainless steel	<ul style="list-style-type: none"> • Coating exhibited low COF around 0.3 which is 50-60% lower as compared to NiCrAlY coating at all test temperatures. • Wear rate of the coating is around $10^{-5} \text{mm}^3/\text{Nm}$ which is 60-70% less as compare to NiCrAlY coating at all test temperatures.
Huang et al. (2014)	NiCr/(Cr ₃ C ₂ -BaF ₂ /CaF ₂)	Plasma spray on low carbon steel	<ul style="list-style-type: none"> • Coating exhibits a peak friction coefficient from 0.78-0.82 at room temperature and 0.3 at 800 °C. • Wear rate of the coating is about $6 \times 10^{-5} \text{mm}^3 \text{N}^{-1} \text{m}^{-1}$ at room temperature and about $2 \times 10^{-5} \text{mm}^3 \text{N}^{-1} \text{m}^{-1}$ at 800 °C temperature.

Ramazani et al. (2014)	Ni(Al)-Cr ₂ O ₃ -Ag-CNT-WS ₂	Atmospheric plasma spray on the carbon steel	<ul style="list-style-type: none"> • Ni(Al)-Cr₂O₃-Ag-CNT-WS₂ coating displayed better frictional behavior as compared to pure NiAl and Ni(Al)-Cr₂O₃ coatings. • Coating with 7 vol.% Ag, CNT, and WS₂ exhibited low COF around 0.3 which is 50-60% less as compared to Ni(Al)-Cr₂O₃ coating at all test temperatures.
Zhang et al. (2016)	NiCoCrAlY-Cr ₂ O ₃ /Ag/Mo	Atmospheric plasma spray on nickel base alloy	<ul style="list-style-type: none"> • NiCoCrAlY-Cr₂O₃-Ag composite coating showed excellent lubricating properties below 600 °C as compared to NiCoCrAlY-Cr₂O₃ coating. Wear rate of NiCoCrAlY-Cr₂O₃-Ag coating is 75% lower than the NiCoCrAlY-Cr₂O₃ coating.
Li et al. (2017)	NiAl-Mo-Ag and NiAl-Cr ₂ O ₃ -Mo-Ag	Atmospheric plasma spray on Inconel 718	<ul style="list-style-type: none"> • Cr₂O₃ addition effectively decreased the wear rate of NiAl-Mo-Ag composite coating by 58%. • Heat treatment enhanced the adhesive strength, microhardness and tribological properties of NiAl-Cr₂O₃-Mo-Ag composite coating.

From the existing literature, it is clear that environmental pollutant like fly ash has not exploited well as a coating material for high-temperature erosion, wear, and oxidation resistant coatings. Hence, present work deals with the development of composite coatings consist of metallic, carbides, solid lubricants and fly ash cenospheres for elevated temperature applications.

1.4 Objectives of the present work

From the foregoing literature survey, clear is the fact that the research reports on fly ash based composite coatings for high-temperature application are scarcely available. Development, characterization and performance analysis of fly ash composite coatings are proposed in the present work. The pursuit of a literature review on thermal spray coatings employing different coating powders prompted a thorough and systematic study on erosion, wear and oxidation behavior at elevated temperature. Thereby the work undertaken pursues the following objectives:

1. Formulation of composite coatings composed of metallic, carbides, fly ash cenospheres and solid lubricants with an improving resistance to erosion, wear, and oxidation.
2. Composite coatings developments by plasma spray process on MDN 321 steel.
3. To investigate the mechanical properties and microstructural characterization of the coatings.
4. To study the high temperature (200, 400 and 600 °C) erosion behaviour of composite coatings under 30 and 90° impact angles.
5. To investigate the oxidation behaviour of composite coatings at 600 °C.
6. To evaluate the wear behaviour of composite coatings at 200, 400 and 600 °C using pin on disc tribometer.

The available studies on thermal sprayed fly ash coatings focused on coatability and mechanical properties of the coatings. However, these studies did not address the coatability of fly ash cenospheres. Cenospheres possess lower density as they are naturally available hallow microspheres. Effect of these low density cenospheres on coating properties needs to be addressed. Further, high temperature erosion, oxidation and wear behavior of cenosphere composite coatings is elaborately discussed in the present work

The scope of the present work includes the development of composite coatings with fly ash cenospheres for high-temperature applications. Cenospheres are blended with $\text{Cr}_3\text{C}_2\text{-NiCr}$, NiCrAlY , WC-Co , MoS_2 , CaF_2 , and CaSO_4 to form the composite coatings. Plasma spraying is carried out with different composition of powders using

constant spray parameters. Such coated samples are characterized using Scanning Electron Microscope (SEM), Energy Dispersive Spectroscopy (EDS) and X-ray diffraction (XRD). Density, micro hardness and the adhesion strength of the coatings are evaluated further. High-temperature erosion, oxidation and wear behavior of the coatings are studied at different testing parameters.

1.5 Outline of the thesis

The systematic study conducted with respect to the above objectives is presented in the thesis. A brief skeletal structure of the thesis is detailed as below.

- Chapter 1 aims at providing necessary details of the research in thermal spray composite coatings along with an exhaustive literature survey followed by objectives of the present work.
- Chapter 2 focuses on the substrate and feedstocks used to develop the composite coatings, coating technique adopted and testing methodology.
- Chapter 3 presents the experimental results of characterization, erosion, oxidation and wear behaviour of the composite coatings at elevated temperature. The results are discussed.
- Chapter 4 highlights the significant conclusions drawn from the results presented earlier.

2 MATERIALS AND METHODS

2.1 Substrate

In the present investigation, MDN 321 steel (AISI equivalent-321) is used as a substrate material which is procured from Mishra Dhatu Nigam Ltd., Hyderabad, India. MDN 321 steel is primarily used in jet engine parts, expansion joints, exhaust manifolds, high temperature chemical production equipment's, fire tube boilers, furnace parts, tube pipes, and pressure vessels. Diamond saw is used to trim the substrate to the required dimension prior to plasma spraying. Samples with 12×12×4 mm dimensions are used for wear studies and 25×20×4 are used for erosion and oxidation studies. The chemical composition of the substrate material is listed in Table 2.1.

Table 2.1 Chemical composition (wt. %) of MDN 321 steel.

Substrate	Composition	C	Si	S	P	Cr	Fe	Ti	Ni
MDN 321	Nominal	0.08	2.00	-	-	18.00	Bal	0.40	11.50
	Actual	0.10	1.46	0.005	0.013	18.13	Bal	0.62	10.36

2.2 Coating feedstock

Commercially available Cr_3C_2 -25NiCr, WC-Co, NiCrAlY, fly ash cenospheres, MoS_2 , CaF_2 and CaSO_4 solid lubricants are utilized as coating feedstocks. The composition of each powder is presented in Table 2.2

Nominal mean particle size distribution of the powders is measured using laser diffraction technique (Cilas, 1064, France) and is reported in Table 2.3. These powders are blended mechanically by weight fraction before getting sprayed. The composition of the powders used for coating preparation is presented in Table 2.4 and Table 2.5.

2.3 Plasma spraying

Plasma spraying is carried out using METCO USA 3MB equipment (Spraymet Surface Technologies Private Limited, Bangalore, India). Prior to spraying, working surface of the substrate is roughened by grit blasting using alumina powder of 150 μm size. The roughened substrates are cleaned using acetone to remove the dust from the surface. Details of spray parameters are listed in Table 2.6.

Table 2.2 Composition of powders.

Coating Powders	Composition	Type	Supplier
Cr ₃ C ₂ -25NiCr	Cr ₃ C ₂ -25(Ni20Cr)	Agglomerated and sintered	PRAXAIR, USA
WC-Co	88WC-12Co	Agglomerated and sintered	Powder Alloy Corporation, USA
NiCrAlY	Ni 22Cr 10Al 1Y	Gas atomized	Powder Alloy Corporation, USA
Cenospheres	SiO ₂ 52-62 %, Al ₂ O ₃ 32-36 %, traces of Fe ₂ O ₃ and TiO ₂	Spherical	Cenospheres India Pvt Ltd, Kolkata
MoS ₂	----	Laboratory reagent grade	Loba Chemie Pvt Ltd, Mumbai, India
CaF ₂	----	Laboratory reagent grade	Loba Chemie Pvt Ltd, Mumbai, India
CaSO ₄	----	Laboratory reagent grade	Loba Chemie Pvt Ltd, Mumbai, India

*As specified by Cenosphere India Pvt. Ltd., Kolkata, India.

Table 2.3 Mean particle size (µm) distribution of powders.

Particle size	Cr ₃ C ₂ -25NiCr	NiCrAlY	WC/Co	Cenospheres*	MoS ₂	CaF ₂	CaSO ₄
D (0.1)	26.91	41.88	23.52	----	0.63	4.27	8.72
D (0.5)	46.49	70.75	38.78	----	5.95	57.52	63.79
D (0.9)	79.31	120.33	64.11	----	29.45	115.52	132.57
0-10%	----	----	----	106	----	----	----
70-90%	----	----	----	63	----	----	----
0-30%	----	----	----	53	----	----	----
Mean	50.35	76.54	41.71	65	10.62	60.30	70.00

*As specified by Cenosphere India Pvt. Ltd., Kolkata, India.

Table 2.4 Composition of coating powders for erosion and oxidation test (wt. %).

Coating	Cr ₃ C ₂ - 25NiCr	NiCrAlY	WC/Co	Cenospheres
Cr ₃ C ₂ -NiCr/Cenosphere	70	----	----	30
NiCrAlY/WC-Co/Cenosphere	----	52.5	17.5	30

Table 2.5 Composition of coating powders for wear test (wt. %).

Coating	Cr ₃ C ₂ - 25NiCr	NiCrAlY	WC/ Co	Cenospheres	MoS ₂	CaF ₂	CaSO ₄
Cr ₃ C ₂ - NiCr/Cenosp here/ MoS ₂ /CaF ₂	50	----	----	30	10	10	----
Cr ₃ C ₂ - NiCr/Cenosp here/ MoS ₂ /CaSO ₄	50	----	----	30	10	----	10
NiCrAlY/W C- Co/Cenosph ere/ MoS ₂ /CaF ₂	----	37.5	12.5	30	10	10	----
NiCrAlY/W C- Co/Cenosph ere/ MoS ₂ /CaSO ₄	----	37.5	12.5	30	10	----	10

Table 2.6 Plasma spray process parameters*.

Argon	Pressure	0.75 MPa
	Flow	40 lpm
Hydrogen	Pressure	0.35 MPa
	Flow	7 lpm
	Current	490 A
	Voltage	60 V
	Powder feed rate	60 g/min
	Stand of distance	100-125 mm

*As provided by Spraymet Surface Technology Pvt. Ltd., Bangalore, India.

2.4 Porosity and density of the coatings

The porosity of the coatings is measured as per (ASTM B276-05) standard. Image analyzer with biovis materials plus software is utilized to determine the porosity values. Twenty fields of view per sample are taken for each coating and the average value is reported. The density of the as-sprayed coatings is measured by the method of water immersion as per (ASTM C135-96) standard using pycnometer as shown in Figure 2.1. The coating is peeled mechanically from the samples in order to measure the density. Minimum weights of the peeled samples are in the range of 1-2 g. The density of the coating is calculated using the following equation.

$$\rho = \frac{(W-p)}{(W_1-p)-(W_2-W)} \quad (1)$$

where, p = weight of the stoppered pycnometer (g), W = weight of the stoppered pycnometer and sample (g), W_1 = weight of the stoppered pycnometer filled with water (g) and W_2 = weight of the stoppered pycnometer, sample, and water (g).

2.5 Surface roughness, microhardness, and adhesion strength test

The surface roughness (Ra) of the as-sprayed coatings is measured using surface roughness tester (SJ-201P, Mitutoyo, Japan) as shown in Figure 2.2. Roughness is measured at 5 different locations and the average value is reported. Microhardness is measured using OMNITECH microhardness tester (Figure 2.3). Vickers microhardness is measured under a 300 g load on the transverse cross section of the coating as well as on the substrate. Total 20 indentations are taken at a different location and the average value is reported.

The adhesion bond strength of the coating is estimated as per (ASTM C633-13) standard (pull-off method). The test is carried out in tension mode using Universal Testing Machine (AG-X plus, Shimadzu hydraulic tensile test machine, Japan) as shown in Figure 2.4 with a strain rate of 0.016 mm/s. The coating deposited on cylindrical samples of diameter 25 mm and the height 25 mm are used for the adhesion strength test. HTK Ultra bond epoxy resin is used as an adhesive to join the coated sample and the counter block. Further, samples are cured at 150 °C for 3 hr in the tubular furnace (Heatron Industrial Heaters, Mangalore, India). The adhesion strength

is estimated by the ratio of maximum load to the cross sectional area and average values of five replicates are reported.



Figure 2.1 Pycnometer.



Figure 2.2 Surface roughness tester.

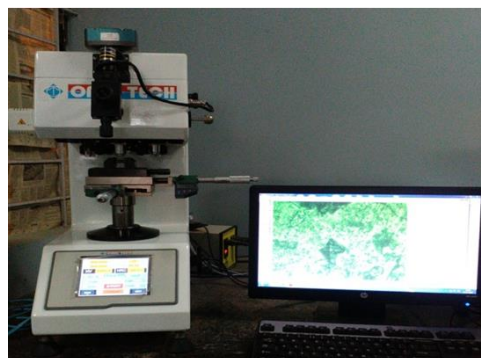


Figure 2.3 Micro hardness tester.



Figure 2.4 Universal testing machine.

2.6 Microstructure and phase analysis

The microstructure of the coated samples is analyzed along the cross-section. Samples are cut along the cross section using the slow cutting machine and cold mounted with the help of acrylic powder and resins. The specimens are polished with 400 to 2000 grit SiC paper and final polishing is done with the help of cloth using superfine diamond paste. Surface morphology and cross sectional microstructure are analyzed by SEM. EDS is used to analyze localized chemical composition. XRD with Ni filter (30 kV and 20 mA with Cu K_{α} radiation) is used to identify the different phases in the powder and in the coatings.

2.7 Solid particle erosion

Erosion test is carried out as outlined in (ASTM G76-13) standard using solid particle air jet erosion tester TR-471-800 (Ducom instruments private limited, Bangalore, India) as presented in Figure 2.5a. Alumina grits are used as an erodent (Figure 2.5b). Schematic presentation of the test setup is presented in Figure 2.5c. Eroderent is fed to the mixing chamber at 2 g/min which gets mixed with hot air flowing through a spiral tube surrounded by tubular heaters. This erodent and air mixture impinges with 30 m/s velocity on the sample which is rigidly fixed in the sample holder. Eroderent velocity is measured by double disc method prior to test. The specimen is heated by the heating elements arranged in the cylindrical manner surrounding the samples as depicted in

Figure 2.5c. The impact angle is set by varying the orientation of the sample holder with respect to the erodent stream. Erosion test conditions are presented in Table 2.7.

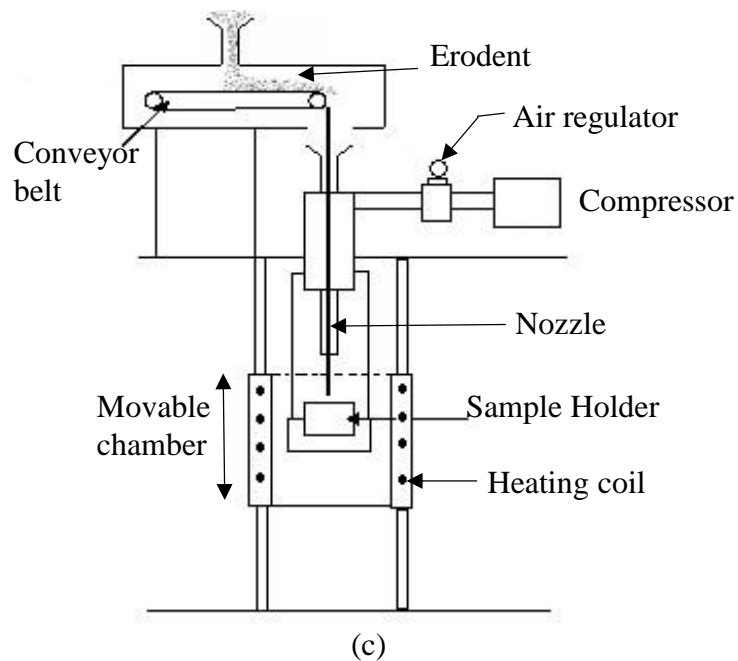
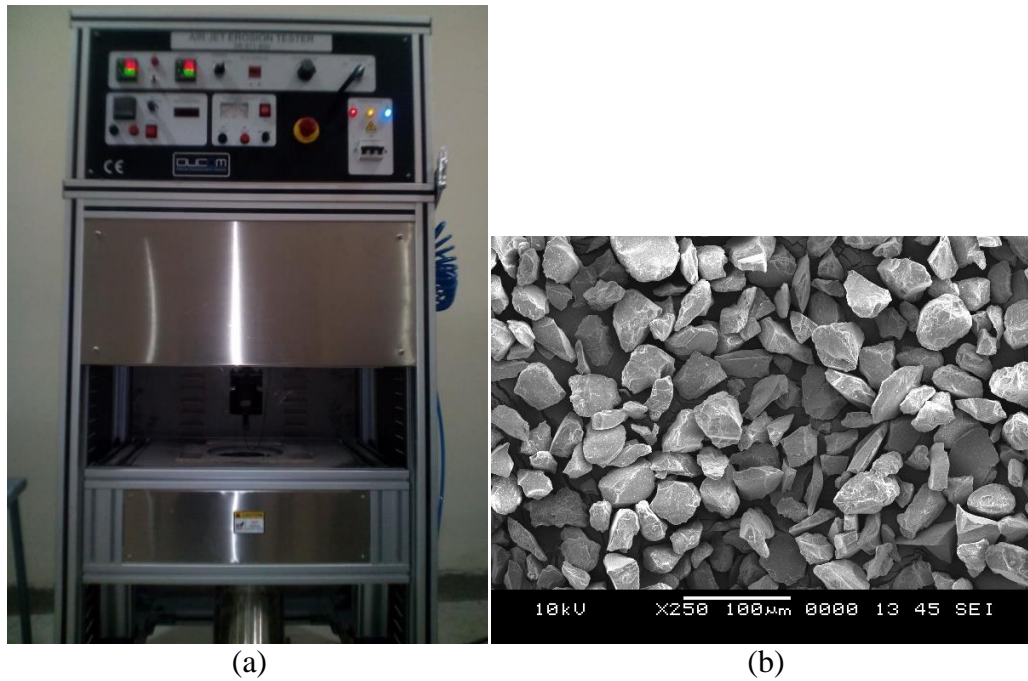


Figure 2.5 (a) Air jet erosion test machine (b) SEM micrograph of alumina erodent (c) schematic presentation of the test setup.

Table 2.7 Erosion test parameters.

Erodent	Alumina
Erodent average size (μm)	50
Particle velocity (m/s)	30
Erodent feed rate (g/min)	2
Impact angle ($^\circ$)	30 and 90
Temperature ($^\circ\text{C}$)	200,400 and 600
Test time (min)	15
Standoff distance (μm)	10
Nozzle diameter (μm)	1.5

Before testing samples are cleaned in acetone, dried and kept in the machine about 15-20 minutes to reach the required test temperature (200, 400 and 600 $^\circ\text{C}$). After every test the samples are cleaned in acetone to remove the erodent particles embedded on the surface, dried and weighed using electronic balance having a resolution of 0.01 mg. The erosion rate is computed by the ratio of mass loss to erodent particles mass. Measurement of volume loss of coating and substrate is carried out using 3D optical non-contact profilometer (Zeta instruments, 20, USA) as shown in Figure 2.6.

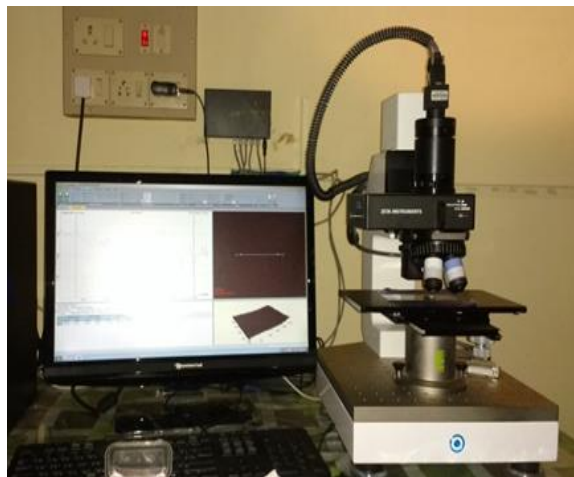


Figure 2.6 3D optical non-contact profilometer.

2.8 Cyclic oxidation

Cyclic oxidation tests are carried out on both substrate and coated samples at 600 °C for 20 cycles using tubular furnace (Heatron Industrial Heaters, Mangalore, India) as shown in Figure 2.7. Prior to the test, the surface area of the sample is measured. Each cycle consists of 1 hour of heating at 600 °C followed by cooling at ambient temperature for 20 minutes. Weight change is recorded for each cycle by electronic balance having a sensitivity of 0.01 mg. Cyclic oxidation is conducted to simulate actual conditions in the thermal power plant (frequent power failures).



Figure 2.7 Tubular furnace.

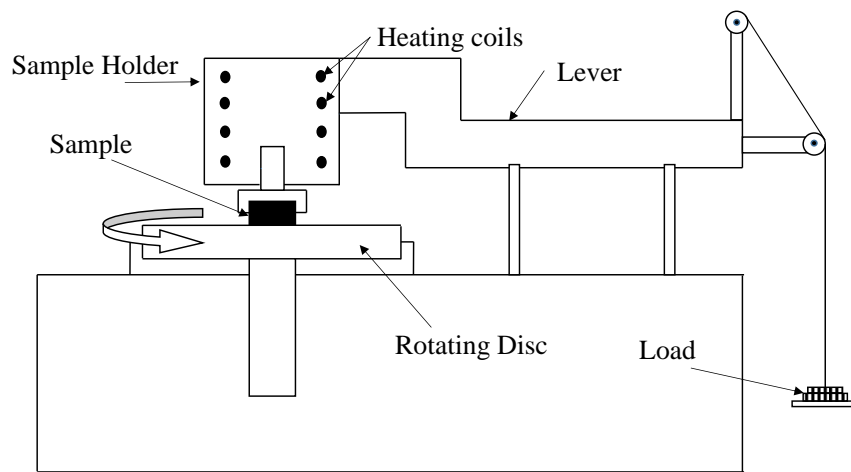
2.9 Sliding wear

Figure 2.8a shows high temperature pin on disc tribometer (TR-20LE-PHM 400-CHM 600, Ducom Instruments Pvt Ltd, Bangalore, India) used for friction and wear measurements. The test is conducted under dry conditions as per (ASTM G99-05) standard. Alumina disc is used as the counter body. Schematic representation of the test setup is presented in Figure 2.8b. Sliding wear tests are conducted with the normal loads of 20 and 40 N at sliding velocity of 1.5 and 2.5 m/s with a constant sliding distance of 3000 m. The test temperatures chosen are 200, 400, 600 °C (Chen et al. 2012, Zhang et al. 2009). A computer-aided data acquisition system is utilized to concurrently record both height loss (using in built displacement transducer) and frictional force. Friction coefficient is computed by dividing the frictional force by normal load. Wear rate is calculated by converting the height loss into volume loss using the pin cross section area and expressed in terms of mm^3/m (Manakari et al. 2015). Subsequent to wear test, the worn surfaces and wear debris are observed through

SEM. The elemental composition of wear debris is determined using EDS. *Results of the tests envisaged here are elaborately discussed in the section to follow.*



(a)



(b)

Figure 2.8 (a) Pin on disc tribometer setup (b) schematic representation of test setup.

3 RESULTS AND DISCUSSION

3.1 Microstructure of MDN 321 steel and morphology of blended coating powders

The optical microscope microstructure of MND 321 steel substrate is shown in Figure 3.1. Marbles reagent is used to etch the sample prior to observe through the optical microscope. Microstructure consists of austenite phase with uniformly distributed carbide particles.

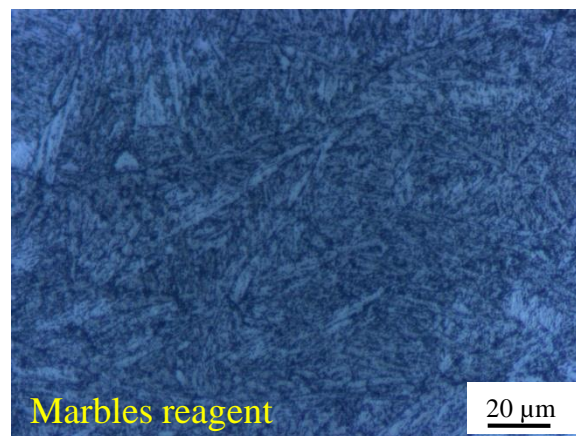


Figure 3.1 Optical micrograph of MDN 321 steel substrate.

Scanning electron micrographs of the blended $\text{Cr}_3\text{C}_2\text{-NiCr/Cenosphere}$ and $\text{NiCrAlY/WC-Co/Cenosphere}$ powders are presented in Figure 3.2. Uniform distribution of all the powders is apparent from Figure 3.2a and Figure 3.2b affirming suitability and feasibility of the mechanical blending adopted.

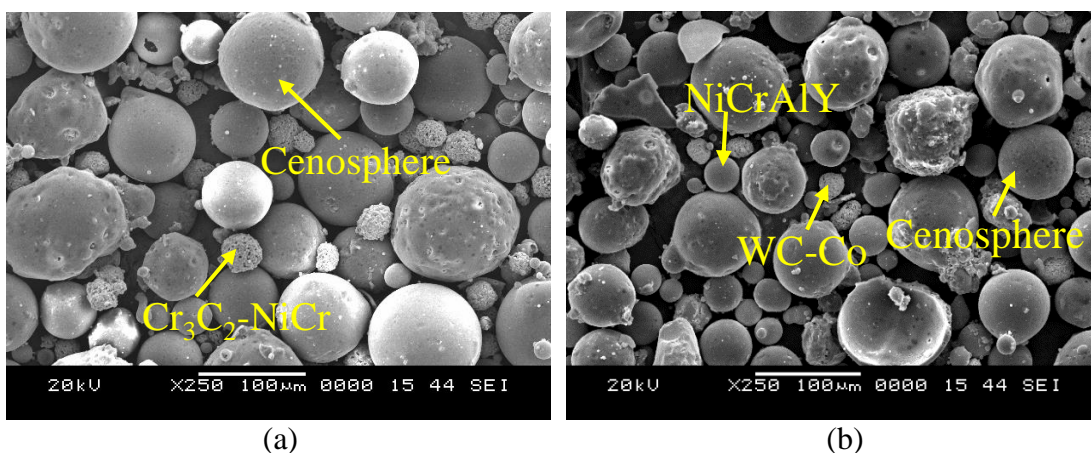


Figure 3.2 Morphology of as blended (a) $\text{Cr}_3\text{C}_2\text{-NiCr/Cenosphere}$ and (b) $\text{NiCrAlY/WC-Co/Cenosphere}$ powders.

Scanning electron micrographs of the blended $\text{Cr}_3\text{C}_2\text{-NiCr/Cenosphere/MoS}_2/\text{CaF}_2$ and $\text{Cr}_3\text{C}_2\text{-NiCr/Cenosphere/MoS}_2/\text{CaSO}_4$ powders are shown in Figure 3.3a and Figure 3.3b respectively. It is observed from the figure that $\text{Cr}_3\text{C}_2\text{-NiCr}$ and cenosphere powders are in spherical shape where in MoS_2 , CaF_2 and CaSO_4 powders are uniformly distributed around these spherical powders.

Figure 3.4a and Figure 3.4b presents morphology of blended $\text{NiCrAlY/WC-Co/Cenosphere/MoS}_2/\text{CaF}_2$ and $\text{NiCrAlY/WC-Co/Cenosphere/MoS}_2/\text{CaSO}_4$ powders. It is observed from the micrograph that all the powders are mixed uniformly. NiCrAlY , WC-Co , and cenospheres are observed to be spherical in shape with MoS_2 , CaF_2 and CaSO_4 present around them.

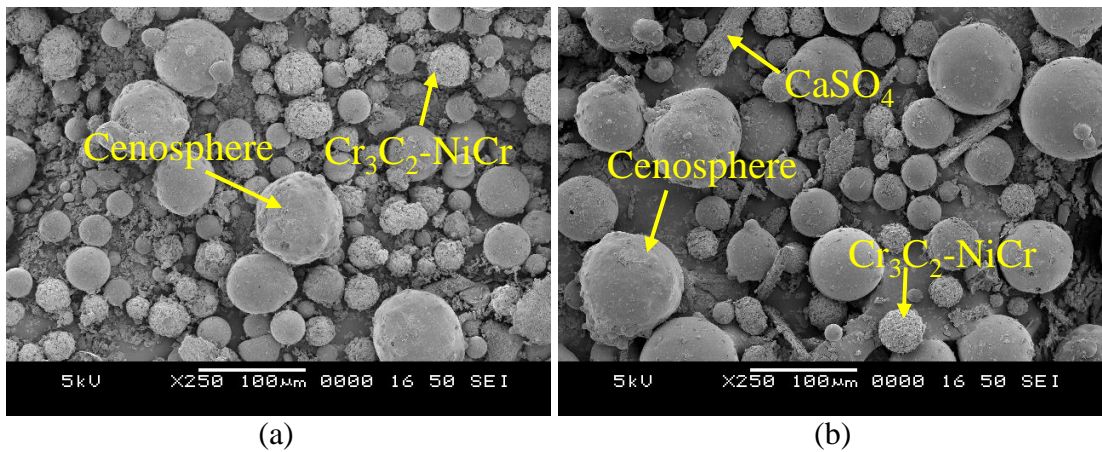


Figure 3.3 Morphology of as blended (a) $\text{Cr}_3\text{C}_2\text{-NiCr/Cenosphere/MoS}_2/\text{CaF}_2$ and (b) $\text{Cr}_3\text{C}_2\text{-NiCr/Cenosphere/MoS}_2/\text{CaSO}_4$ powders.

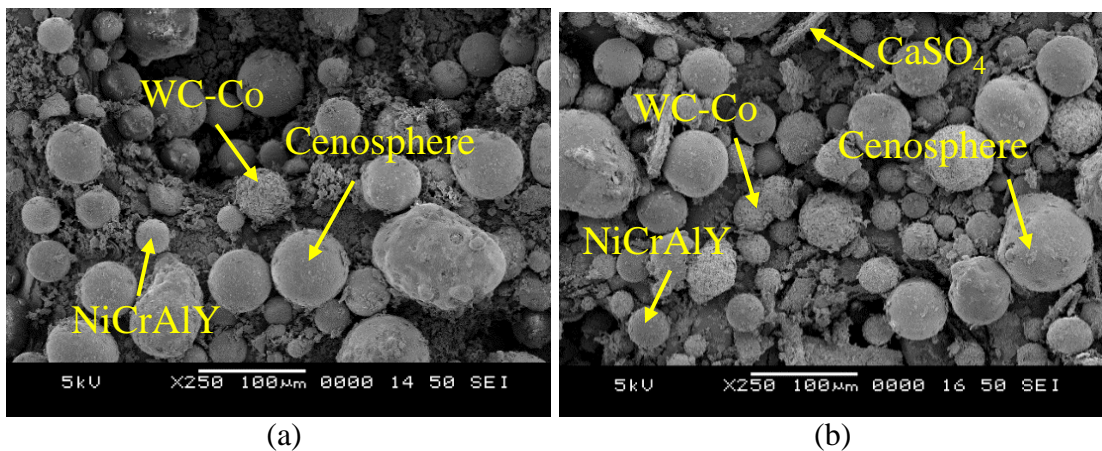


Figure 3.4 Morphology of as blended (a) $\text{NiCrAlY/WC-Co/Cenosphere/MoS}_2/\text{CaF}_2$ (b) $\text{NiCrAlY/WC-Co/Cenosphere/MoS}_2/\text{CaSO}_4$ powders.

3.2 Visual inspection of coated samples

The camera photographs of the as-sprayed coated samples are shown in Figure 3.5. It can be observed that all the coatings are free from surface cracks. Cr_3C_2 -NiCr/Cenosphere coating (Figure 3.5a) is observed to be grey in appearance, NiCrAlY/WC-Co/Cenosphere coating (Figure 3.5b) has light grey color whereas Cr_3C_2 -NiCr/Cenosphere/ MoS_2 / CaF_2 , Cr_3C_2 -NiCr/Cenosphere/ MoS_2 / CaSO_4 , NiCrAlY/WC-Co/Cenosphere / MoS_2 / CaF_2 and NiCrAlY/WC-Co/Cenosphere/ MoS_2 / CaSO_4 coatings (Figure 3.5c-Figure 3.5f) appears in dark grey color.

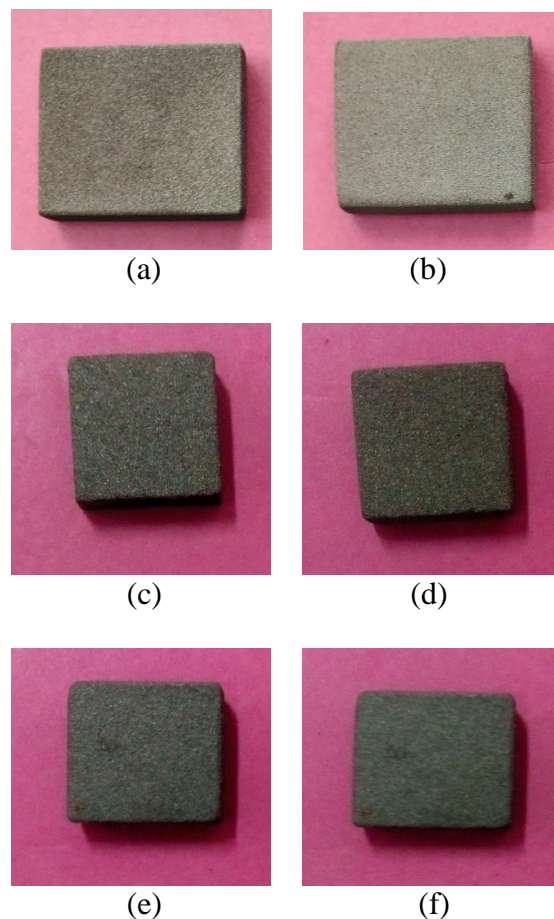


Figure 3.5 The camera photographs of (a) Cr_3C_2 -NiCr/Cenosphere (b) NiCrAlY/WC-Co/Cenosphere (c) Cr_3C_2 -NiCr/Cenosphere/ MoS_2 / CaF_2 (d) Cr_3C_2 -NiCr/Cenosphere/ MoS_2 / CaSO_4 (e) NiCrAlY/WC-Co/Cenosphere/ MoS_2 / CaF_2 and (f) NiCrAlY/WC-Co/Cenosphere/ MoS_2 / CaSO_4 coatings.

3.3 Porosity and density of the coatings

The porosity of the coatings plays an important role in wear, erosion and oxidation studies. Increase in porosity decreases the erosion and oxidation resistance of the coatings. Presence of unmelted/semi-melted particles in the coatings increases the porosity of the coatings. The porosity and density of the coatings are estimated as per the procedure outlined in Section 2.4 and the measured values are reported in Table 3.1.

Table 3.1 Porosity and density of the coatings.

Coating	Porosity (%)	Density (g/cm ³)
Cr ₃ C ₂ -NiCr/Cenosphere	3.49±0.25	3.63±0.20
NiCrAlY/WC-Co/Cenosphere	4.00±0.30	2.90±0.12
Cr ₃ C ₂ -NiCr/Cenosphere/MoS ₂ /CaF ₂	3.80±0.28	3.34±0.25
Cr ₃ C ₂ -NiCr/Cenosphere/MoS ₂ /CaSO ₄	3.70±0.21	3.20±0.15
NiCrAlY/WC-Co/Cenosphere/MoS ₂ /CaF ₂	4.10±0.32	2.78±0.13
NiCrAlY/WC-Co/Cenosphere/MoS ₂ /CaSO ₄	4.00±0.30	2.65±0.15

3.4 Surface roughness, microhardness, and adhesion strength

Surface roughness, microhardness and adhesion strength values of the coatings are listed in Table 3.2. Microhardness is measured across the substrate coating interface. Microhardness of the substrate is found to be 190±10 Hv. Cr₃C₂-NiCr/Cenosphere coating registered higher microhardness as compared to other coatings owing to the higher hardness of Cr₃C₂-NiCr. NiCrAlY/WC-Co/Cenosphere coating displayed lower hardness due to the presence of low hardness NiCrAlY matrix. Similar microhardness values are reported by Somasundaram et al. (2014) for HVOF sprayed WC-Co-NiCrAlY coating. Cr₃C₂-NiCr/Cenosphere/MoS₂/CaF₂, Cr₃C₂-NiCr/Cenosphere/MoS₂/CaSO₄, NiCrAlY/WC-Co/Cenosphere/MoS₂/CaF₂ and NiCrAlY/WC-Co/Cenosphere/MoS₂/CaSO₄ coatings exhibited lower hardness as compared to Cr₃C₂-NiCr/Cenosphere and NiCrAlY/WC-Co/Cenosphere coatings due to the presence of lower hardness MoS₂, CaF₂ and CaSO₄ solid lubricants.

The durability of the coatings depends on the adhesion strength between the substrate and coating. Adhesion strength of the coatings estimated using UTM is listed in Table 3.2. Cr₃C₂-NiCr/Cenosphere and NiCrAlY/WC-Co/Cenosphere coatings registered adhesion strength of 10.60±2.0 and 8.4±1.2 MPa respectively. Comparative estimations of adhesion strength are accounted for by (Behera and Mishra 2012, Mishra et al. 2006). Fractured surface morphology of the coatings after the adhesion strength is presented in Figure 3.6. Fractured surfaces of Cr₃C₂-NiCr/Cenosphere and NiCrAlY/WC-Co/Cenosphere coatings reveals the adhesive failure as it occurred between the substrate and coating (Figure 3.6a and Figure 3.6b).

Table 3.2 Surface roughness, microhardness, and adhesion strength values.

Coating	Roughness		Microhardness (HV)	Adhesion strength (MPa)
	(Ra)	(Rz)		
Cr ₃ C ₂ -NiCr/Cenosphere	12.00±0.6	56.25±1.0	1134±52	10.6±2.0
NiCrAlY/WC-Co/Cenosphere	11.27±0.8	52.40±0.9	0428±48	08.4±1.2
Cr ₃ C ₂ - NiCr/Cenosphere/MoS ₂ /CaF ₂	14.00±1.1	69.10±1.5	0823±35	14.3±2.0
Cr ₃ C ₂ - NiCr/Cenosphere/MoS ₂ /CaSO ₄	14.40±1.4	71.00±2.0	0848±30	18.1±2.2
NiCrAlY/WC-Co/Cenosphere /MoS ₂ /CaF ₂	14.30±1.3	70.20±2.0	0352±30	10.5±1.7
NiCrAlY/WC-Co/Cenosphere /MoS ₂ /CaSO ₄	14.70±1.6	72.15±2.0	0370±25	12.0±2.1

From Figure 3.6c, Figure 3.6d, Figure 3.6e and Figure 3.6f it can be seen that for Cr₃C₂-NiCr/Cenosphere/MoS₂/CaF₂, Cr₃C₂-NiCr/Cenosphere/MoS₂/CaSO₄, NiCrAlY/WC-Co/Cenosphere/MoS₂/CaF₂ and NiCrAlY/WC-Co/Cenosphere /MoS₂/CaSO₄ coatings fracture within the coating interface exhibiting cohesive coating failure. This implies that the adhesion strength of the NiCr bond coat to the substrate is higher than the cohesive strength of the coating. Cohesive failure of coatings is due to the lower impact force of low-density cenospheres and solid lubricants during the spraying process. This lower impact force decreases the bonding strength within the coating constituents and resulting in cohesive failure (Zhang et al. 2009).

3.5 Surface morphology and cross sectional microstructure of the coatings

Surface morphology of $\text{Cr}_3\text{C}_2\text{-NiCr/Cenosphere}$ coating along with the EDS composition analysis at the selected points on the surface is presented in Figure 3.7. The surface morphology of the as-sprayed $\text{Cr}_3\text{C}_2\text{-NiCr/Cenosphere}$ coating consists of a melted matrix, semi-melted particles, unmelted particles, and pores. The pores are formed during solidification and due to fracture of cenospheres during splat formation. EDS point analysis at point A is rich in chromium and nickel representing the matrix region. Point B is rich in aluminum and silicon and represents cenosphere particle.

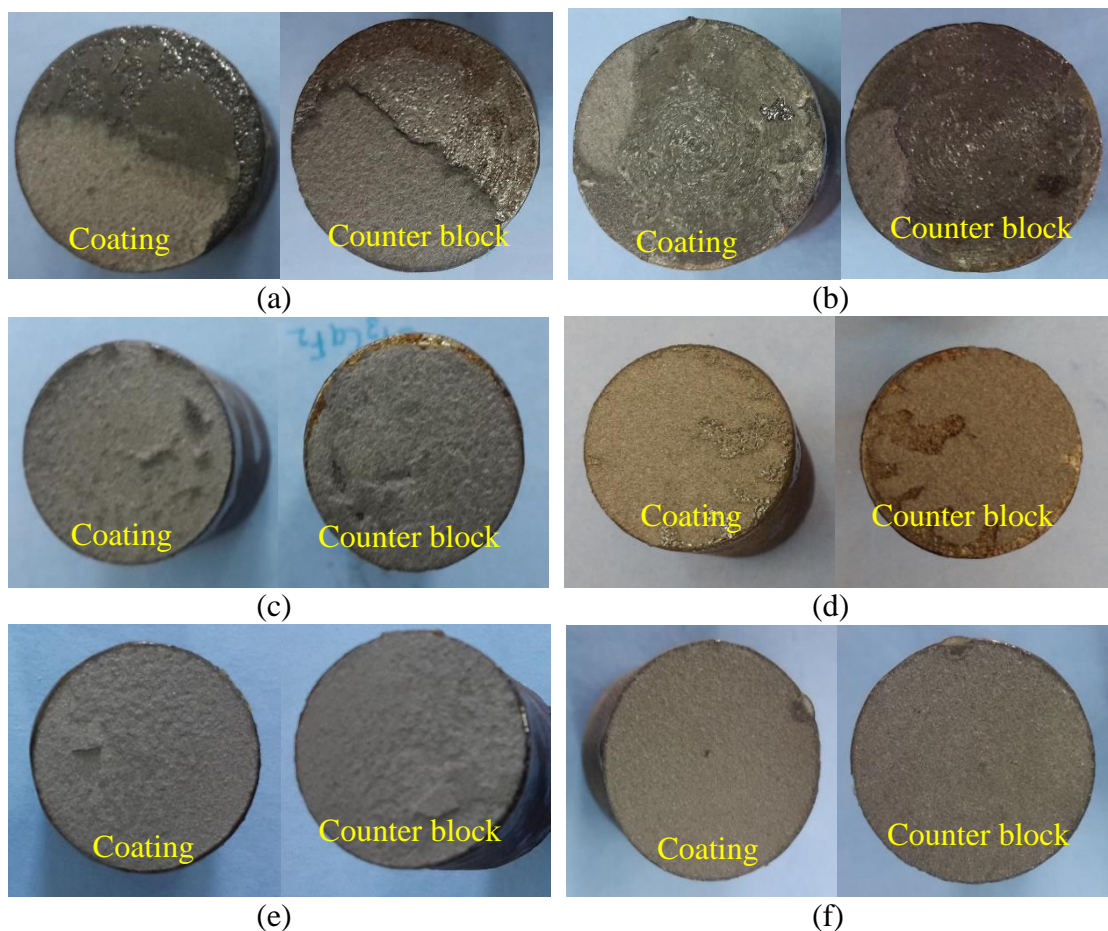


Figure 3.6 Fractured surfaces of (a) $\text{Cr}_3\text{C}_2\text{-NiCr/Cenosphere}$ (b) $\text{NiCrAlY/WC-Co/Cenosphere}$ (c) $\text{Cr}_3\text{C}_2\text{-NiCr/Cenosphere/MoS}_2\text{/CaF}_2$ (d) $\text{Cr}_3\text{C}_2\text{-NiCr/Cenosphere/MoS}_2\text{/CaSO}_4$ (e) $\text{NiCrAlY/WC-Co/Cenosphere/MoS}_2\text{/CaF}_2$ and (f) $\text{NiCrAlY/WC-Co/Cenosphere /MoS}_2\text{/CaSO}_4$ coatings.

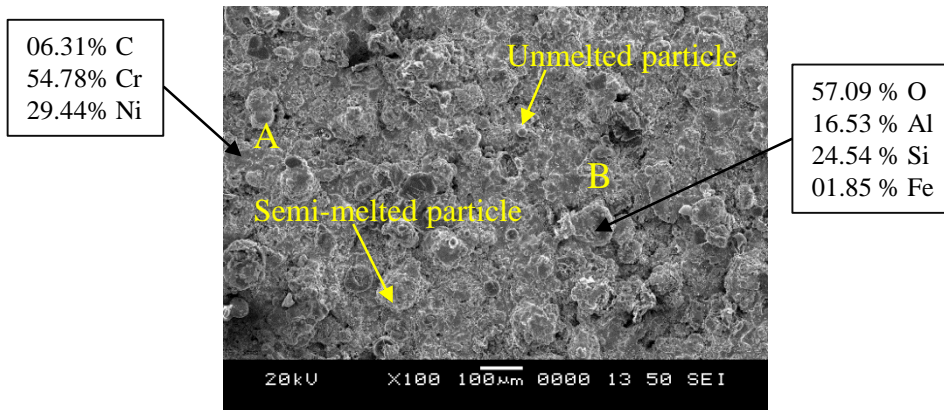


Figure 3.7 Surface morphology of $\text{Cr}_3\text{C}_2\text{-NiCr/Cenosphere}$ coating along with the EDS composition analysis.

Surface morphology of $\text{NiCrAlY/WC-Co/Cenosphere}$ coating along with the EDS composition analysis, at the selected points on the surface, is depicted in Figure 3.8. The surface morphology of coating consists of a matrix, semi-melted particles, unmelted particles, and pores. EDS point analysis at point A and B represents the matrix region and cenosphere particle respectively.

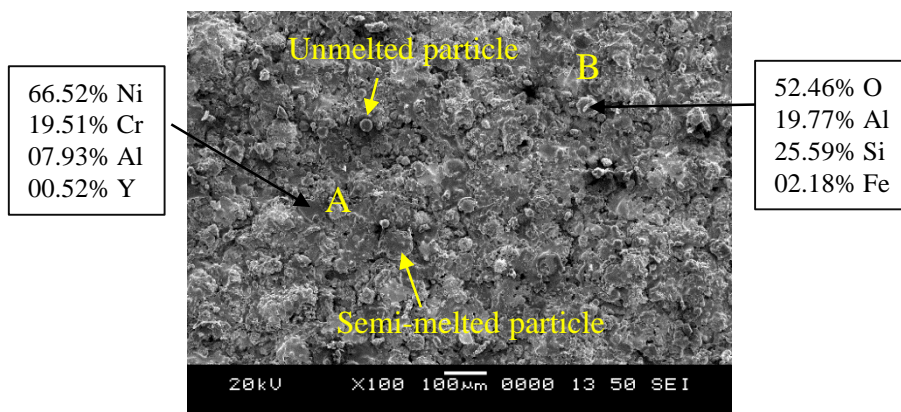


Figure 3.8 Surface morphology of $\text{NiCrAlY/WC-Co/Cenosphere}$ coating along with the EDS composition analysis.

Figure 3.9 presents surface morphologies of $\text{Cr}_3\text{C}_2\text{-NiCr/Cenosphere/MoS}_2\text{/CaF}_2$, $\text{Cr}_3\text{C}_2\text{-NiCr/Cenosphere/MoS}_2\text{/CaSO}_4$, $\text{NiCrAlY/WC-Co/Cenosphere/MoS}_2\text{/CaF}_2$ and $\text{NiCrAlY/WC-Co/Cenosphere/MoS}_2\text{/CaSO}_4$ coatings. From the figure, it is observed that the coatings surface consist of a melted matrix, semi-melted particles, unmelted particles and a small amount of pores.

Scanning electron micrographs of $\text{Cr}_3\text{C}_2\text{-NiCr/Cenosphere}$ and $\text{NiCrAlY/WC-Co/Cenosphere}$ coatings obtained along the cross section is depicted by Figure 3.10. The average thickness of $\text{Cr}_3\text{C}_2\text{-NiCr/Cenosphere}$ coating is 400-450 μm and $\text{NiCrAlY/WC-Co/Cenosphere}$ coating is 350-400 μm as seen in Figure 3.10a and Figure 3.10c respectively. Adhesion of the coating to the substrate is good with well dispersion of cenospheres as seen from these micrographs.

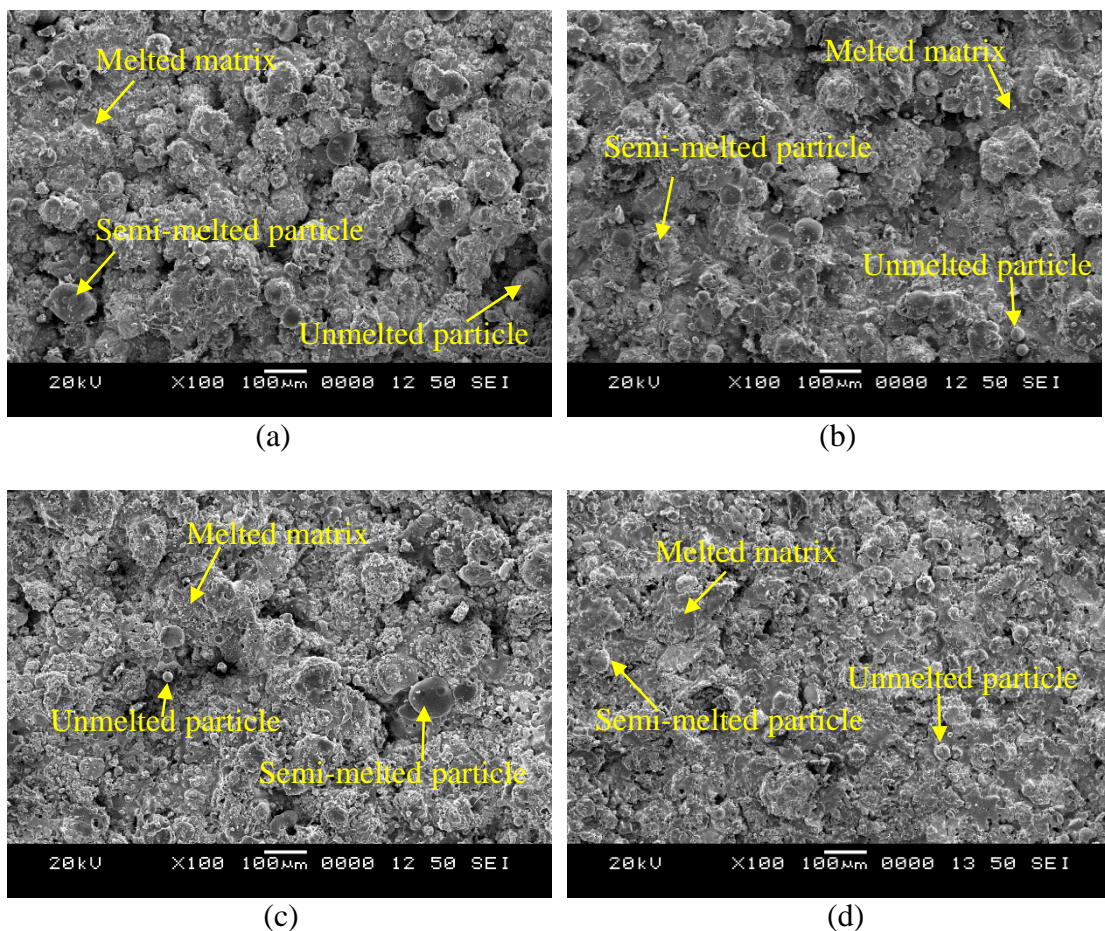


Figure 3.9 Surface morphologies of (a) $\text{Cr}_3\text{C}_2\text{-NiCr/Cenosphere/MoS}_2\text{/CaF}_2$ (b) $\text{Cr}_3\text{C}_2\text{-NiCr/Cenosphere/MoS}_2\text{/CaSO}_4$ (c) $\text{NiCrAlY/WC-Co/Cenosphere/MoS}_2\text{/CaF}_2$ and (d) $\text{NiCrAlY/WC-Co/Cenosphere /MoS}_2\text{/CaSO}_4$ coatings.

Micrograph of the circled zone in Figure 3.10a is presented in Figure 3.10b and marked zone in Figure 3.10c is presented in Figure 3.10d respectively at higher magnifications. Lamellar dense packed structure of $\text{Cr}_3\text{C}_2\text{-NiCr}$ and NiCrAlY/WC-Co coating is evident from the Figure 3.10a and Figure 3.10c. Constituents present are marked in

micrograph Figure 3.10b as 1 - NiCr solid solution matrix, 2 - Cr_3C_2 particles embedded in NiCr matrix and 3 - cenospheres particles based on the EDS analysis of Figure 3.10b and is presented in Table 3.3. On the similar lines constituents present are marked in micrograph Figure 3.10d as 1 - NiCrAlY solid solution matrix, 2 - WC-Co matrix and 3 - cenosphere particles based on the EDS analysis of Figure 3.10d and is presented in Table 3.4.

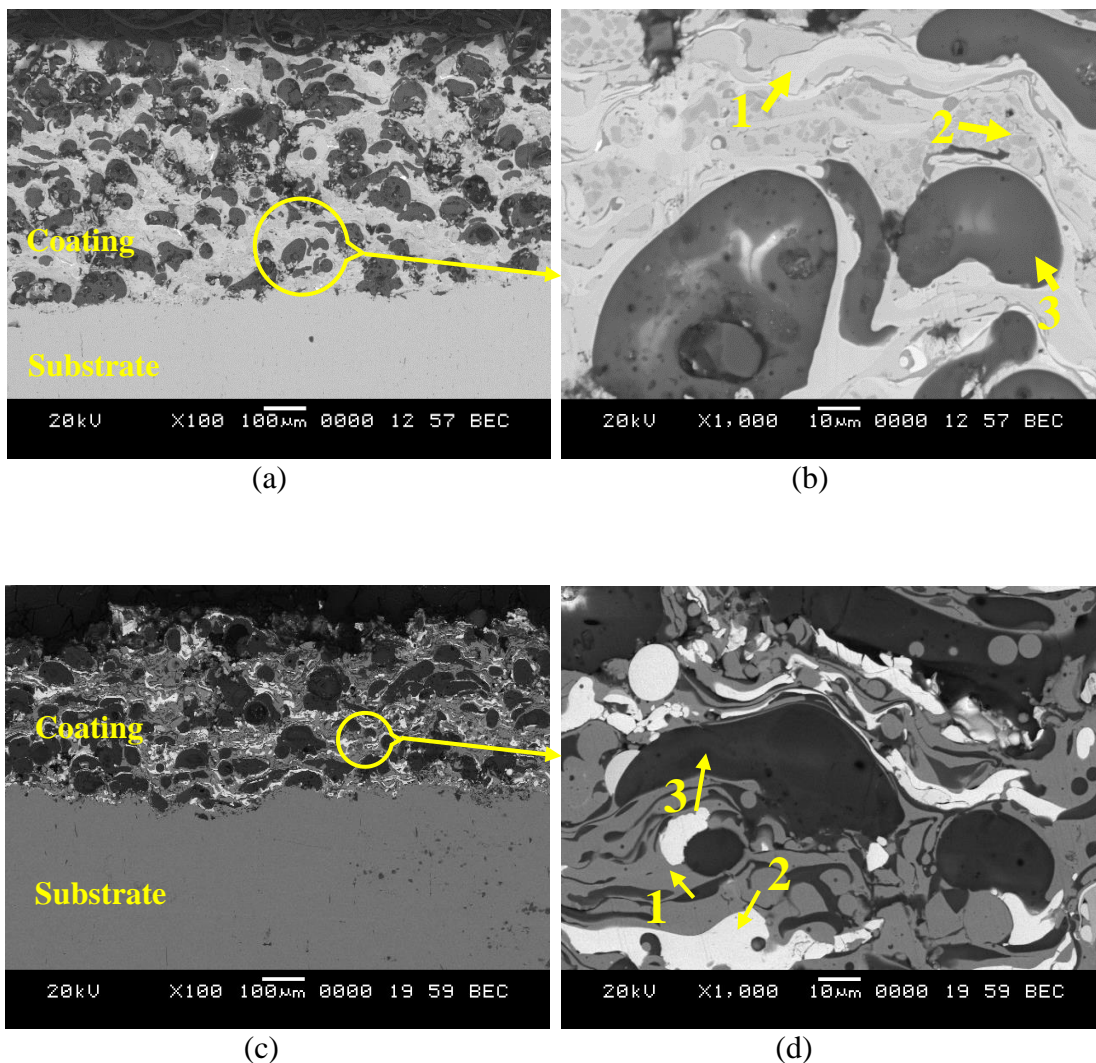


Figure 3.10 Cross sectional SEM images of (a) Cr_3C_2 -NiCr/cenosphere coating at lower magnification (b) circled area of (a) at higher magnification and (c) NiCrAlY/WC-Co/cenosphere coating at lower magnification (d) circled area of (c) at higher magnification.

Table 3.3 EDS analysis of Cr₃C₂-NiCr/Cenosphere coating at the designated point in Figure 3.6b.

Element	Oxide	Phase 1	Phase 2	Phase 3
----	SiO ₂	----	----	60.70
----	Al ₂ O ₃	----	----	36.24
----	Fe ₂ O ₃	----	----	3.04
C	----	04.39	14.05	----
Cr	----	19.27	60.84	----
Ni	----	74.67	25.11	----

Table 3.4 EDS analysis of NiCrAlY/WC-Co/Cenosphere coating at the designated point in Figure 3.6d.

Element	Oxide	Phase 1	Phase 2	Phase 3
----	SiO ₂	----	----	57.50
----	Al ₂ O ₃	----	----	39.23
----	Fe ₂ O ₃	----	----	3.26
Al	----	1.75	----	----
C	----	----	08.43	----
Cr	----	20.27	----	----
Ni	----	77.46	----	----
Y	----	0.52	----	----
W	----	----	79.40	----
Co	----	----	12.17	----

Scanning electron micrographs of a polished cross section of Cr₃C₂-NiCr/Cenosphere/MoS₂/CaF₂ and Cr₃C₂-NiCr/Cenosphere/MoS₂/CaSO₄ coatings are presented in Figure 3.11. The NiCr bond coat well adheres to substrate as well as coating as seen from Figure 3.11a and Figure 3.11c. The average thickness of bond coat and the top coat are in the range of 100 and 400 μm respectively.

The marked area in Figure 3.11a and Figure 3.11c is enlarged and presented in Figure 3.11b and Figure 3.11d respectively. Coating constituents are distributed uniformly with fully melted spalts, some semi melted and unmelted particles that are bonded to each other tightly. From Figure 3.11b and Figure 3.11d, it is seen that coatings mainly consist of cenosphere phase (dark gray) and Cr₃C₂-NiCr phase (light gray) along with MoS₂, CaF₂, and CaSO₄ phases.

Figure 3.12 shows scanning electron micrographs of polished cross-section of NiCrAlY/WC-Co/Cenosphere/MoS₂/CaF₂ and NiCrAlY/WC-Co/Cenosphere/MoS₂/CaSO₄ coatings. The NiCr bond coat well adheres with substrate and coating, increasing the adhesive strength between the substrate and coating. The average thickness of bond coat and coatings are 100 and 400 μm respectively for both the coatings. The marked area in Figure 3.12a and Figure 3.12c is enlarged and presented in Figure 3.12b and Figure 3.12d respectively for clarity.

From Figure 3.12b and Figure 3.12d, it is observed that coating constituents are distributed uniformly with fully melted splats and some semi melted particles which are bonded together. Coatings mainly consist of cenosphere phase (dark gray), NiCrAlY phase (light gray) and WC-Co phase (white colour) along with MoS₂, CaF₂, and CaSO₄ phases.

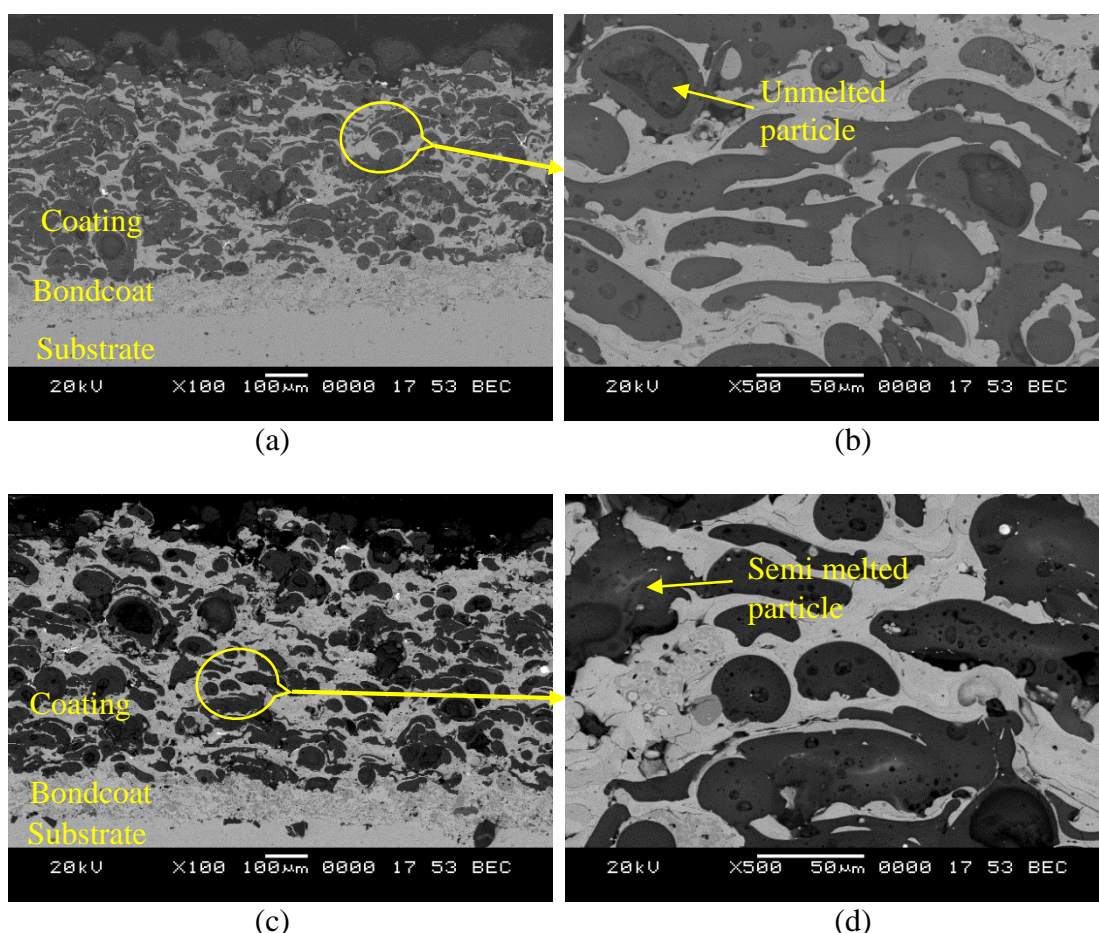


Figure 3.11 Cross sectional SEM images of (a), (b) Cr₃C₂-NiCr/Cenosphere/MoS₂/CaF₂ coating; (c), (d) Cr₃C₂-NiCr/Cenosphere/MoS₂/CaSO₄ coating.

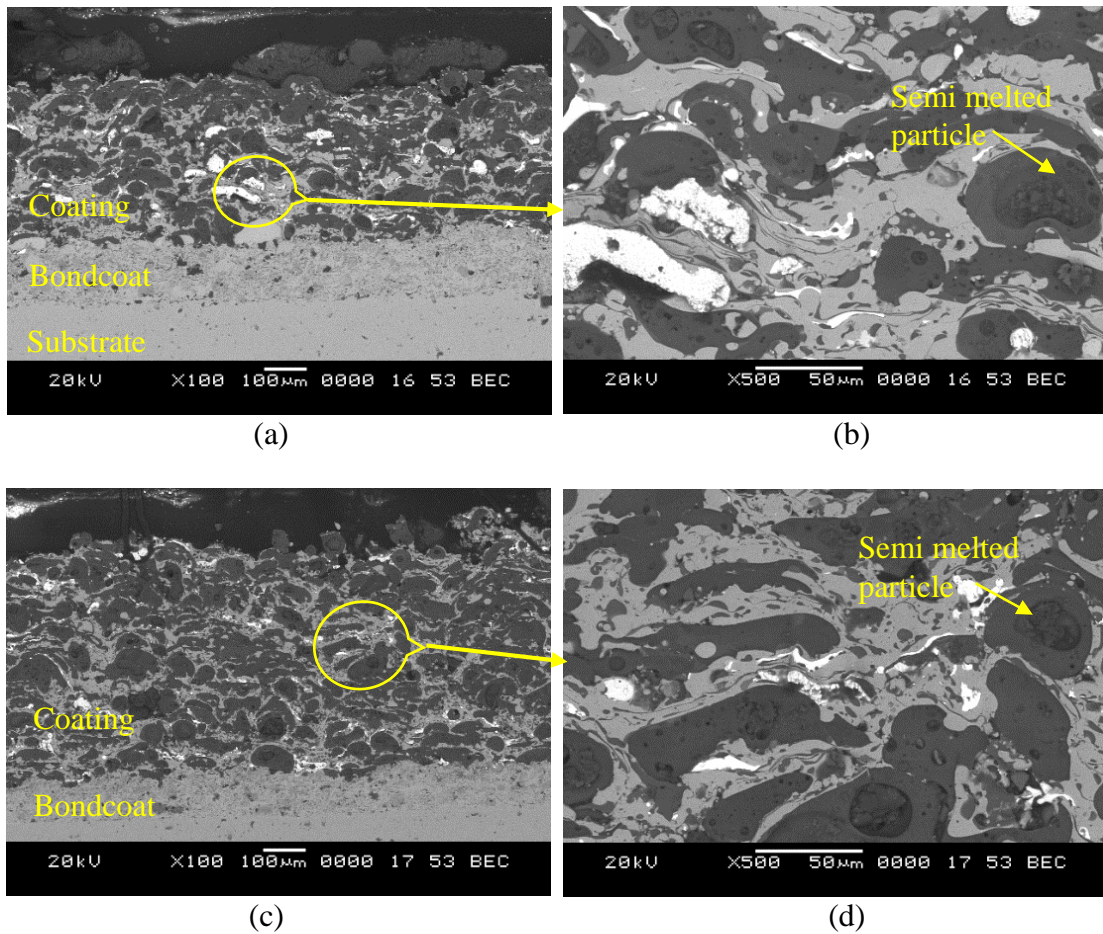


Figure 3.12 Cross sectional SEM images of (a), (b) NiCrAlY/WC-Co/Cenosphere/MoS₂/CaF₂ coating; (c), (d) NiCrAlY/WC-Co/Cenosphere/MoS₂/CaSO₄ coating.

3.6 Phase analysis

The X-ray diffraction pattern of Cr₃C₂-NiCr/Cenosphere blended powder and as-coated sample is shown in Figure 3.13. Distinct major peaks of 3Al₂O₃.2SiO₂, Al₂SiO₅ and SiO₂ and minor peaks of Cr₃C₂, Al₂O₃ are observed in blended powder. The slightly broadened peaks are observed in the coated samples due to the differential dissolution of carbides in NiCr binder. Cr₂₃C₆, Cr and Ni are major peaks while SiO₂ and Al₂SiO₅ are minor peaks found in the coated sample.

Figure 3.14 presents the XRD of NiCrAlY/WC-Co/Cenosphere blended powder and as-coated sample. XRD pattern of blended powder consists of Al₂O₃, SiO₂ and AlNi major phases and minor phases of 3Al₂O₃.2SiO₂ and WC. XRD pattern of coating depicts Al₂O₃ and AlNi as major phases and W₂C as a minor phase. Decarburization of

WC during plasma spraying results W_2C due to higher temperatures in the plasma spray process.

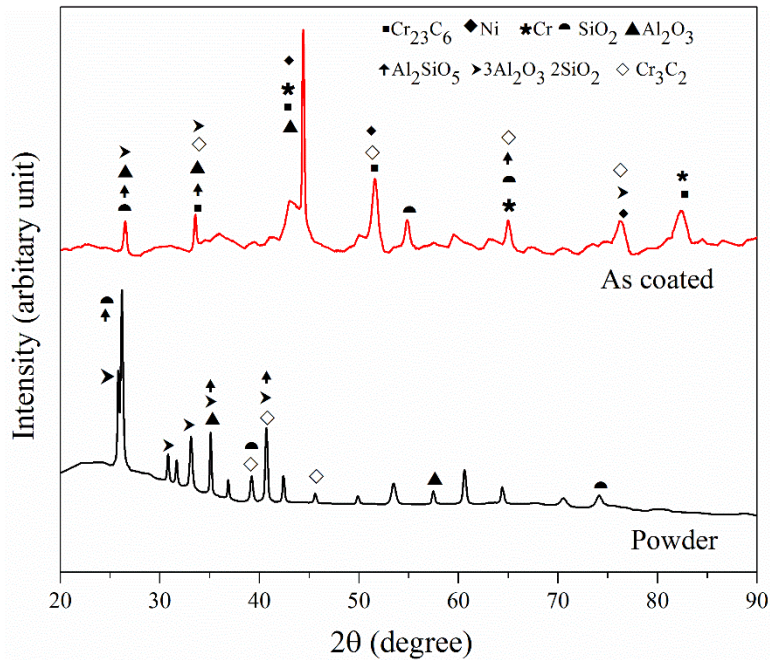


Figure 3.13 XRD pattern of as blended powder and Cr_3C_2 -NiCr/Cenosphere coating.

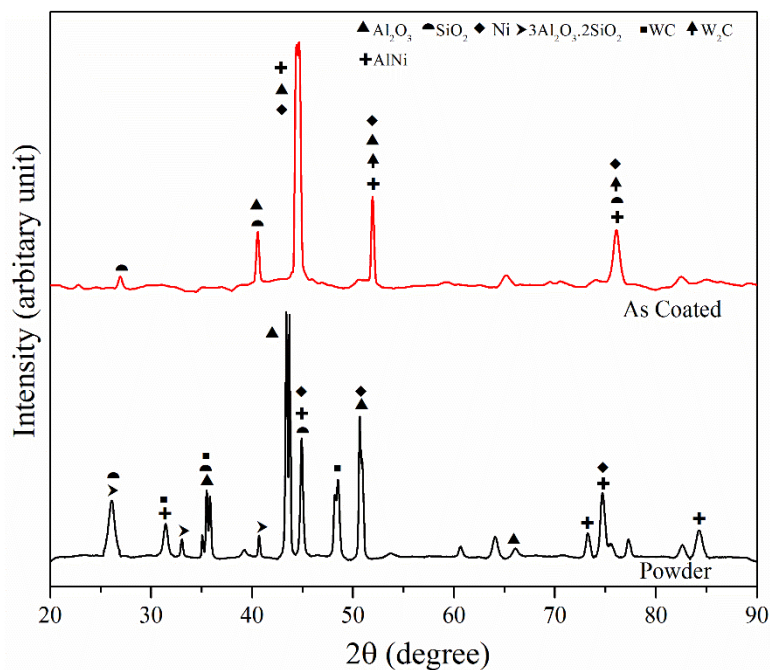


Figure 3.14 XRD pattern of as blended powder and NiCrAlY/WC-Co/Cenosphere coating.

The X-ray diffraction pattern of $\text{Cr}_3\text{C}_2\text{-NiCr/Cenosphere/MoS}_2\text{/CaF}_2$ and $\text{Cr}_3\text{C}_2\text{-NiCr/Cenosphere/MoS}_2\text{/CaSO}_4$ blended powder and as sprayed coatings are presented in Figure 3.15 and Figure 3.16 respectively. It is observed that the blended powder of $\text{Cr}_3\text{C}_2\text{-NiCr/Cenosphere/MoS}_2\text{/CaF}_2$ (Figure 3.15) mainly consist of Ni, SiO_2 , Al_2O_3 , and Cr_3C_2 as major phases along with minor phases of $3\text{Al}_2\text{O}_3.2\text{SiO}_2$, MoS_2 and CaF_2 . The XRD pattern of as deposited $\text{Cr}_3\text{C}_2\text{-NiCr/Cenosphere/MoS}_2\text{/CaF}_2$ (Figure 3.15) coating consist of Al_2O_3 and Ni as a major phases while, SiO_2 , Cr_3C_2 , MoS_2 , and CaF_2 as a minor phases. Similar phases are observed in the XRD pattern of $\text{Cr}_3\text{C}_2\text{-NiCr/Cenosphere/MoS}_2\text{/CaSO}_4$ blended powder and as a sprayed coating (Figure 3.16) as seen in $\text{Cr}_3\text{C}_2\text{-NiCr/Cenosphere/MoS}_2\text{/CaF}_2$ except CaF_2 , which is replaced by CaSO_4 .

Figure 3.17 and Figure 3.18 shows the XRD pattern of $\text{NiCrAlY/WC-Co/Cenosphere/MoS}_2\text{/CaF}_2$ and $\text{NiCrAlY/WC-Co/Cenosphere/MoS}_2\text{/CaSO}_4$ blended powder and as sprayed coatings respectively. The results depict that the blended powder of $\text{NiCrAlY/WC-Co/Cenosphere/MoS}_2\text{/CaF}_2$ (Figure 3.17) mainly consist of Ni, SiO_2 , Al_2O_3 phases along with minor phases of $3\text{Al}_2\text{O}_3.2\text{SiO}_2$, WC, MoS_2 and CaF_2 .

The XRD pattern of as deposited $\text{NiCrAlY/WC-Co/Cenosphere/MoS}_2\text{/CaF}_2$ coating consists of Al_2O_3 and AlNi_3 as a major phases and MoS_2 , CaF_2 and W_2C as a minor phases. W_2C is detected in the as deposited coating owing to the decarburization of WC during plasma spraying. WC decomposes significantly into W_2C during spraying owing to higher temperatures in the plasma spray process. Similar phases are observed in the XRD pattern of $\text{NiCrAlY/WC-Co/Cenosphere/MoS}_2\text{/CaSO}_4$ blended powder and as a sprayed coating (Figure 3.18) as seen in $\text{NiCrAlY/WC-Co/Cenosphere/MoS}_2\text{/CaF}_2$ except CaF_2 that is replaced by CaSO_4 .

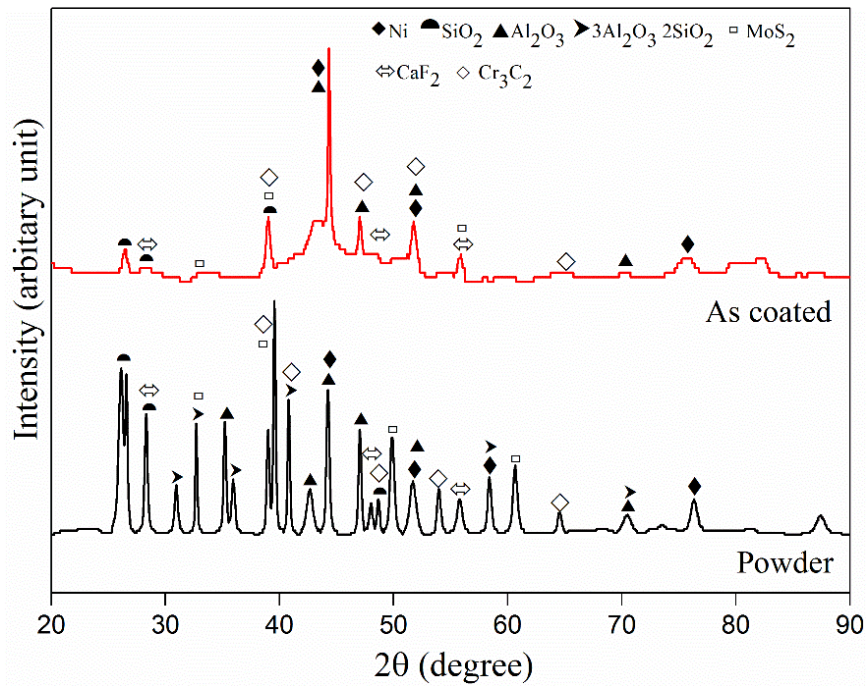


Figure 3.15 XRD pattern of as blended powder and Cr₃C₂-NiCr/Cenosphere/MoS₂/CaF₂ coating.

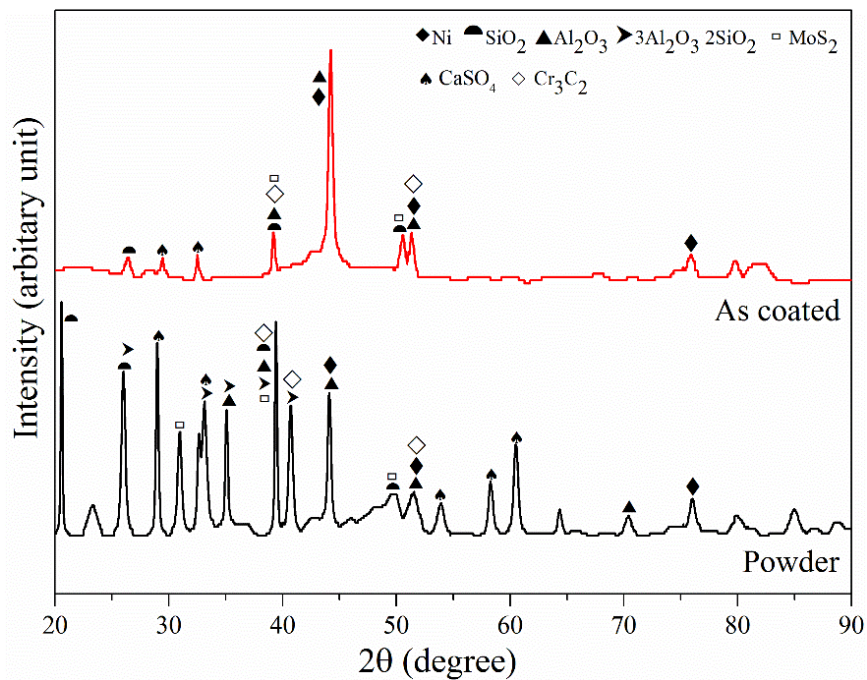


Figure 3.16 XRD pattern of as blended powder and Cr₃C₂-NiCr/Cenosphere/MoS₂/CaSO₄ coating.

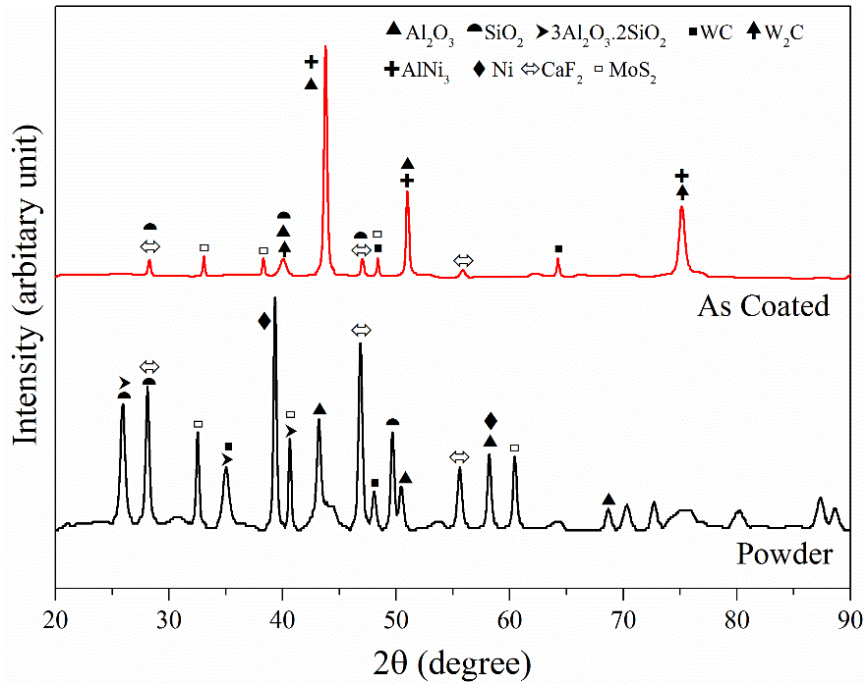


Figure 3.17 XRD pattern of as blended powder and NiCrAlY/WC-Co/Cenosphere/MoS₂/CaF₂ coating.

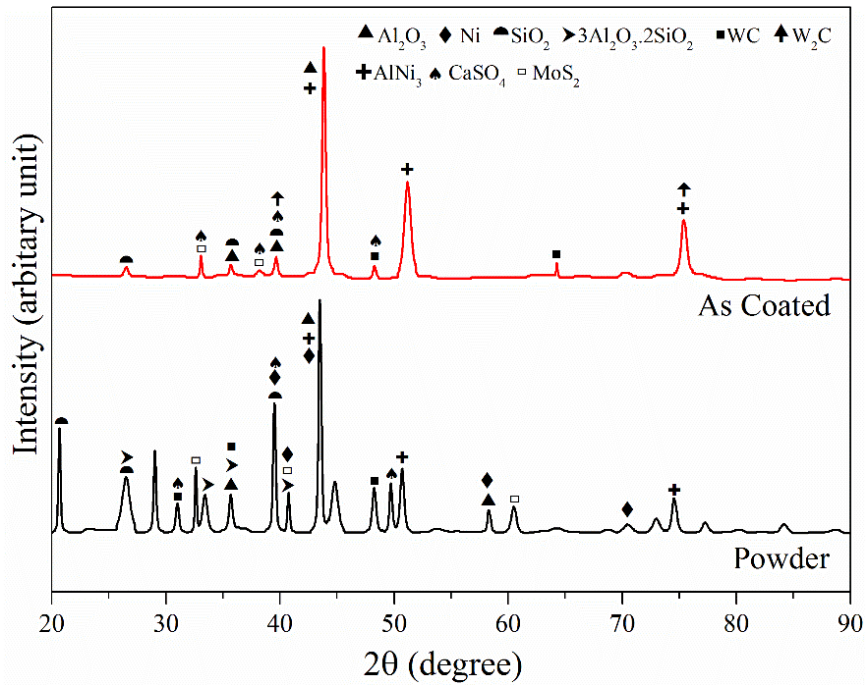


Figure 3.18 XRD pattern of as blended powder and NiCrAlY/WC-Co/Cenosphere/MoS₂/CaSO₄ coating.

3.7 Solid particle erosion studies

Erosion is the material removal phenomena resulting from solid particles impingement on the surface. Figure 3.19a and Figure 3.19b show the schematic diagram of erosion scar produced on the eroded surface at 30 and 90° impact angles respectively. At 30° impact angle (Figure 3.19a) erodent particle slides on the surface thereby remove the material across the larger area as compared to 90° impact angle. Region A (Figure 3.19) is called as a localized area where erodent particles are in direct contact with the surface and maximum material is removed from this zone. Region B is called as an elastically loaded region and the minimum material is removed from this zone.

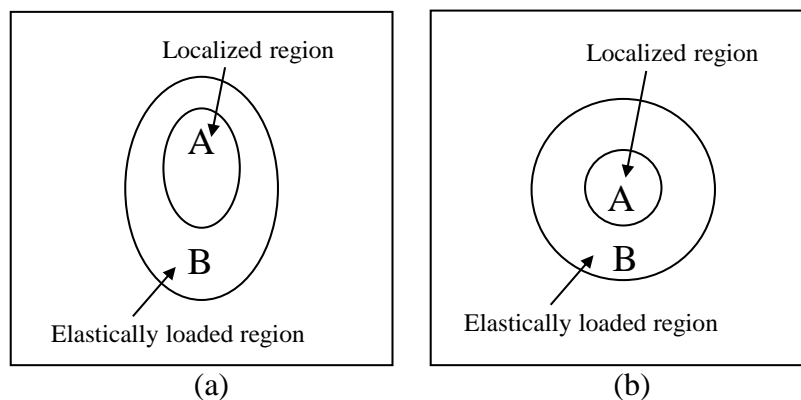


Figure 3.19 Schematic diagram showing the erosion scar produced on typical eroded surface at (a) 30 and (b) 90° impact angles.

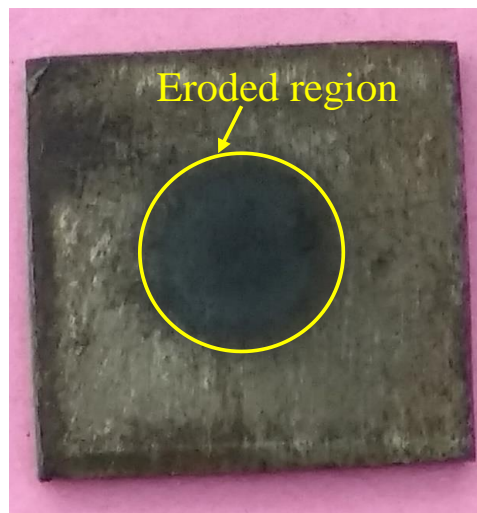
3.7.1 Erosion behaviour of MDN 321 steel substrate

Figure 3.20a and Figure 3.20b exhibits the camera photographs of the eroded MDN 321 steel at 600 °C with 30 and 90° impact angles respectively. It is observed from the photographs that eroded region is maximum for 30° impact angle as compared to 90° impact angle. This might be because of sliding action at 30° impact angle covering the maximum region. Eroded surface 3-D profiles of MDN 321 steel at 30 and 90° impact angles with different temperatures are presented in Figure 3.21 and Figure 3.22 respectively. The large crater is observed at 90° impact angle indicating maximum material removal leading to higher erosion volume loss. Effect of temperature on the erosion rate and volume loss is presented in Figure 3.23a and Figure 3.23b respectively. Erosion rate and volume loss increases with increase in the test temperature and impact angle, more prominent being at higher values (Figure 3.23a and Figure 3.23b). Erosion

volume loss at 600 °C is approximately 3.5 and 2.5 times higher than at 200 °C for 30 and 90° impact angles respectively. Increase in the test temperature results in a decrease of substrate hardness owing to the annealing effect. At higher temperatures, the formed oxide layer is insufficient to resist erodent impact resulting in oxide layer cracking and its subsequent removal. Hence increasing volume loss is noted with the rise in test temperature.

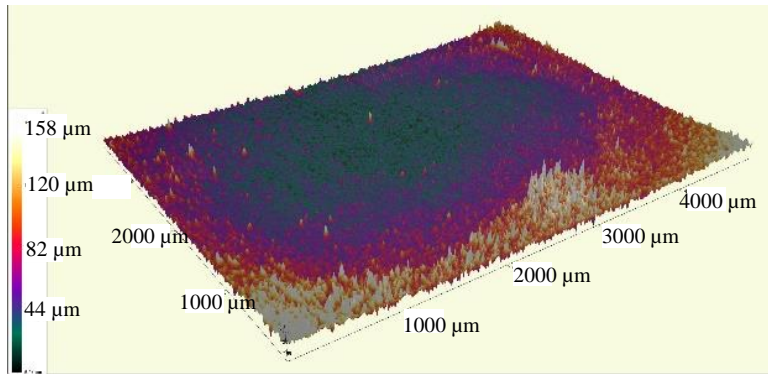


(a)

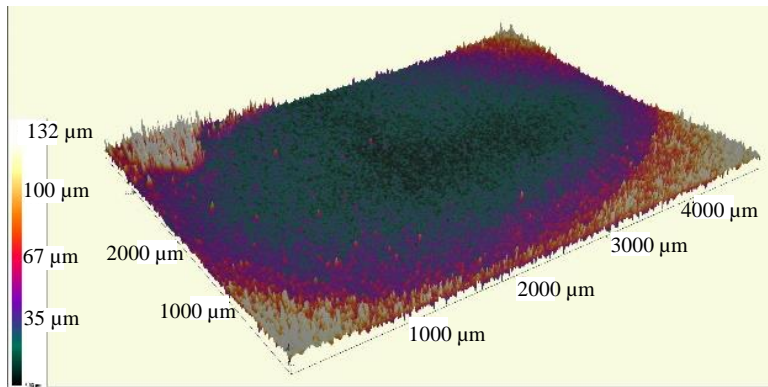


(b)

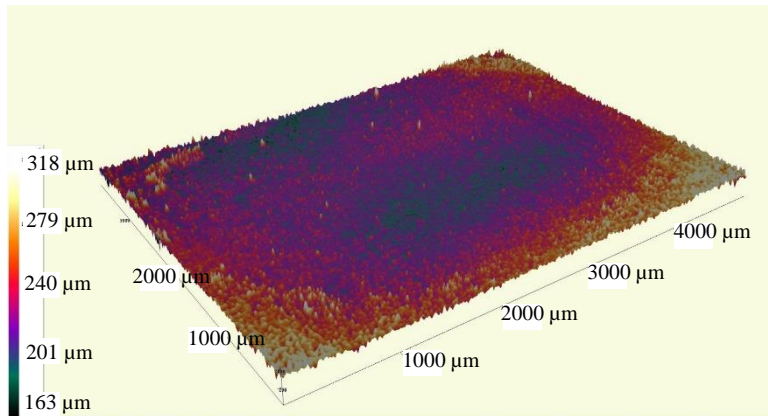
Figure 3.20 The camera photographs of the eroded MDN 321 steel at 600 °C with (a) 30 and (b) 90° impact angles.



(a)



(b)



(c)

Figure 3.21 Eroded surface 3-D profile of MDN 321 steel at (a) 200 (b) 400 and (c) 600 °C with 30° impact angle.

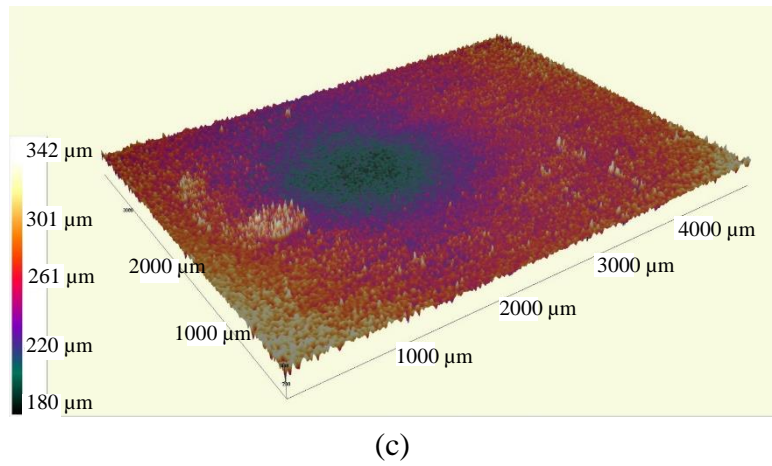
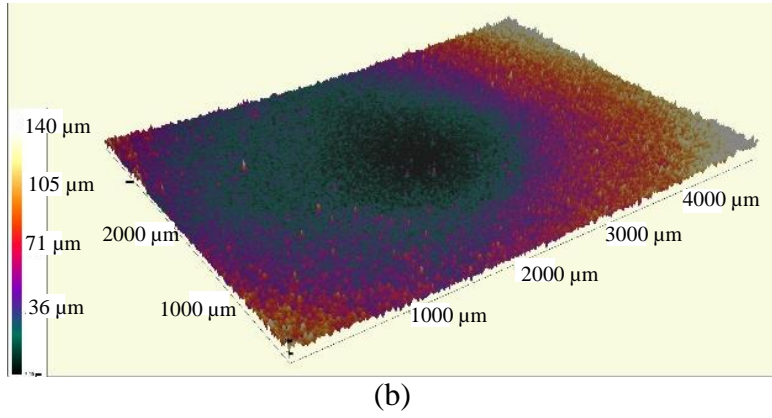
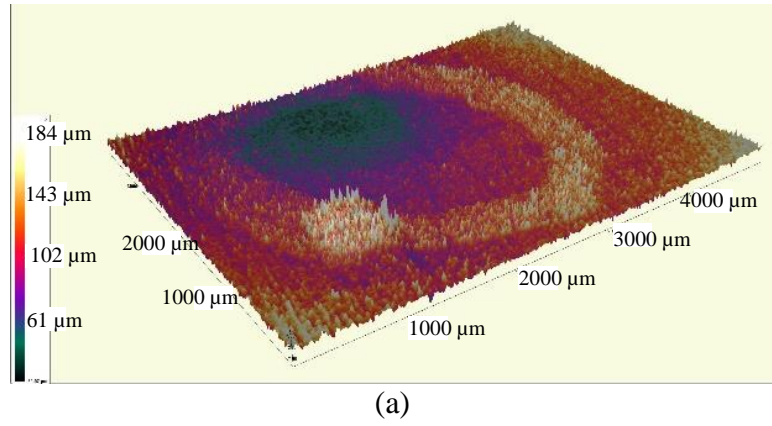
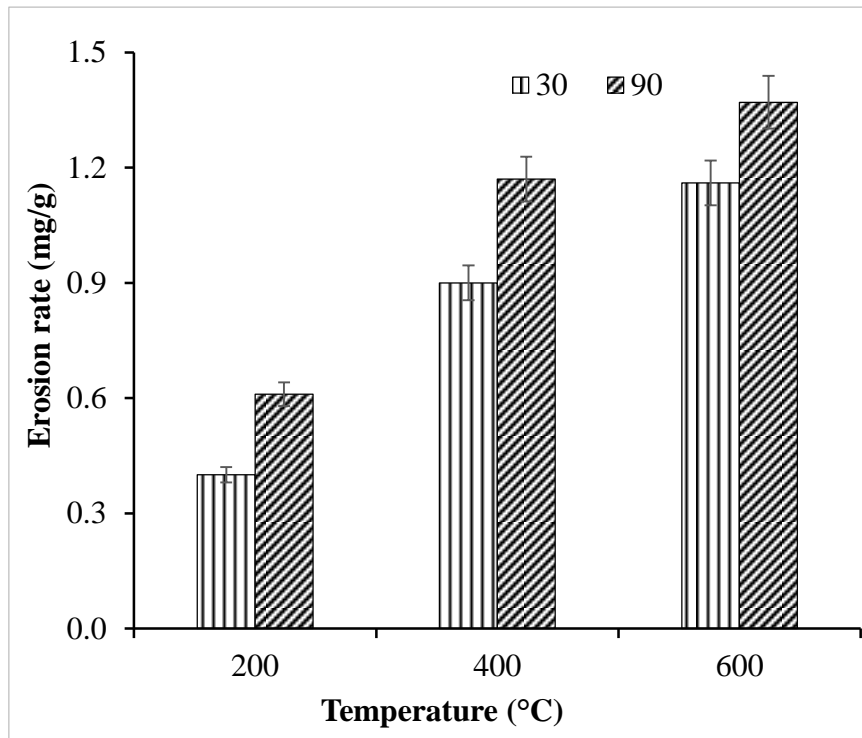
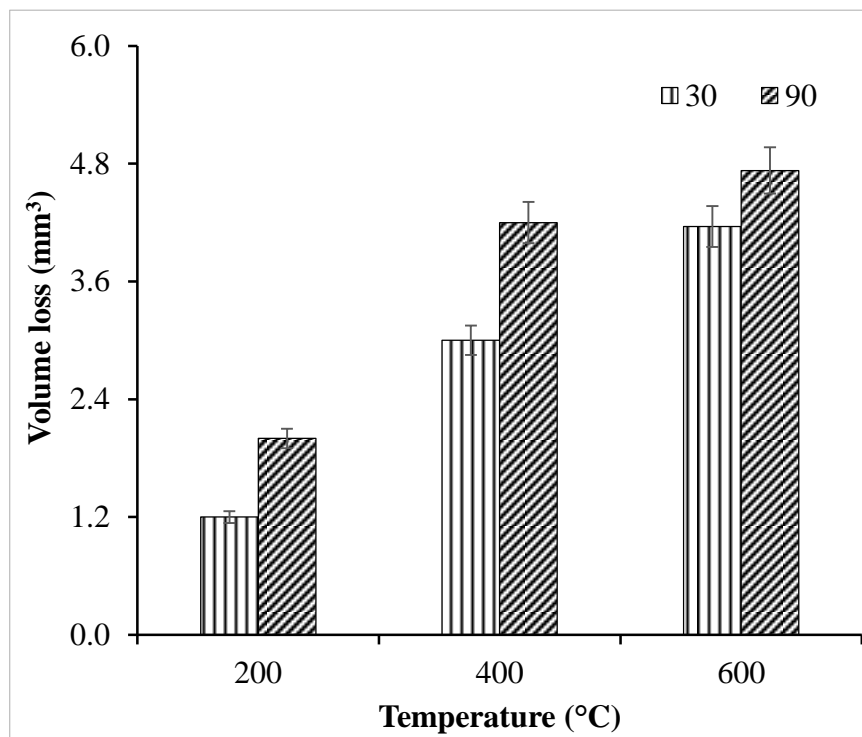


Figure 3.22 Eroded surface 3-D profile of MDN 321 steel at (a) 200 (b) 400 and (c) 600 °C with 90° impact angle.



(a)



(b)

Figure 3.23 (a) erosion rate and (b) volume loss of MDN 321 steel as a function of temperature at 30 and 90° impact angles.

Morphology of the eroded MDN 321 steel surface at 30 and 90° impact angles are shown in Figure 3.24 and Figure 3.25 respectively with different temperatures. Maximum material loss takes place in ductile mode at low impact angles whereas higher impact angle governs material removal in brittle mode (Ramachandran et al. 2013). From Figure 3.24 it is observed that material has undergone severe plastic deformation which results in ploughing and forms lip at the exit end of the erodent. With subsequent impacts, these highly strained lips are vulnerable to get removed as micro-platelets. Some grooves and cracks are also observed in the micrograph. At higher temperature, hardness of the substrate decreases and as the erodent particle slides, material gets deformed to get removed subsequently. At 90° impact angle (Figure 3.25), craters are observed. As erodent particles impact the surface, the crack gets initiated resulting in oxide layer fragmentation (Figure 3.25). With the subsequent impact of erodent, fragments of the oxide layer are removed from the surface in the form of micro-platelets producing craters.

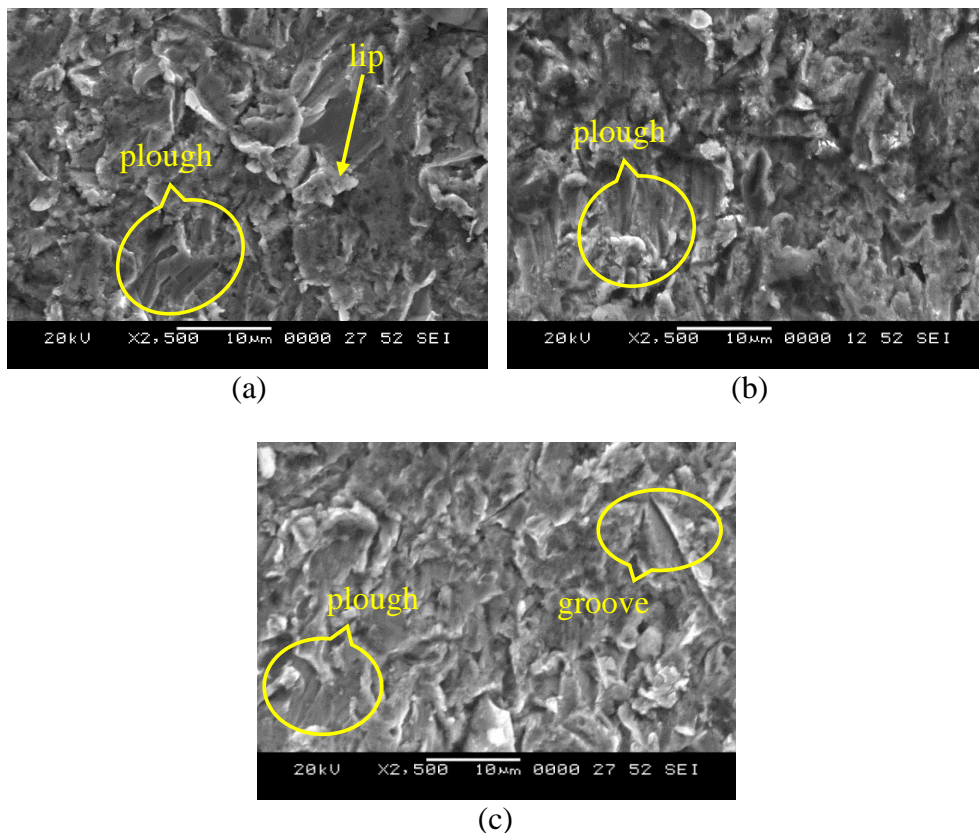


Figure 3.24 Eroded surface SEM micrographs of MDN 321 steel at (a) 200 (b) 400 and (c) 600 °C with 30° impact angle.

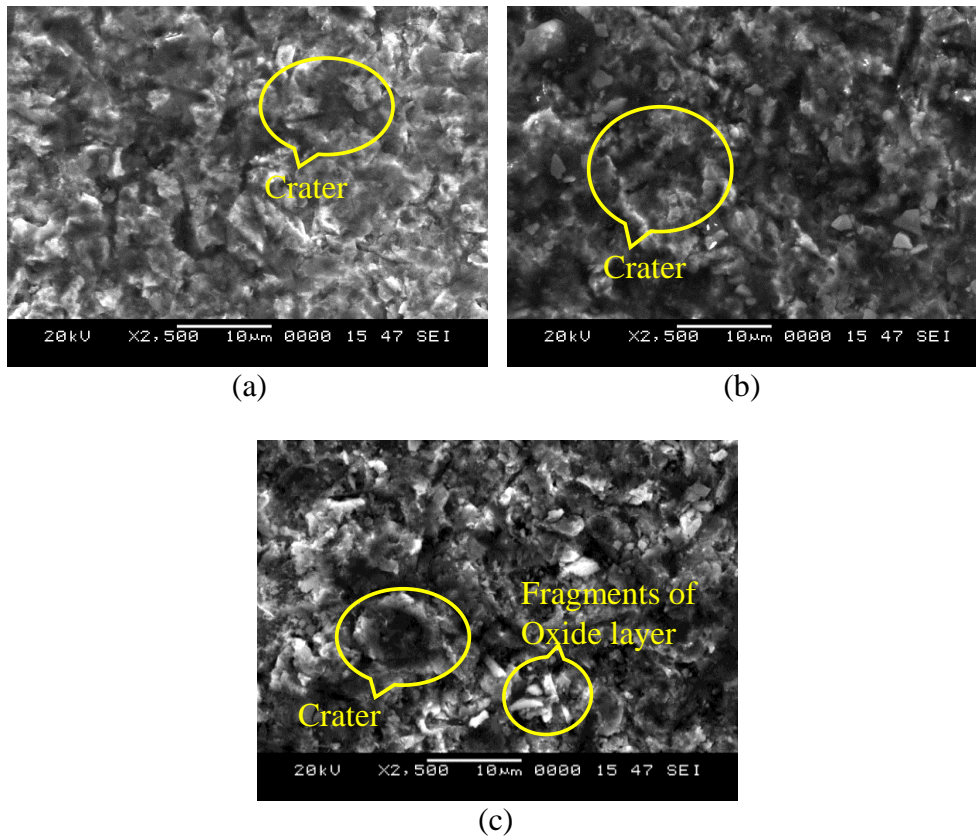


Figure 3.25 Eroded surface SEM micrographs of MDN 321 steel at (a) 200 (b) 400 and (c) 600 °C with 90° impact angle.

3.7.2 Erosion behaviour of Cr₃C₂-NiCr/Cenosphere coating

Figure 3.26a and Figure 3.26b depict the camera photographs of the eroded coating at 600 °C with 30 and 90° impact angles respectively. It is observed from the photographs that eroded region is maximum for 30° impact angle as compared to 90° impact angle. Eroded surface 3-D profiles of coating at 30 and 90° impact angles with different temperatures are presented in Figure 3.27 and Figure 3.28 respectively. The material is removed in a larger area at 30° impact angle (Figure 3.27) indicates erodent particle slides on the surface during the erosion test wherein at 90° impact angle, the material is removed from the smaller area with more crater depth indicating the absence of sliding phenomena.

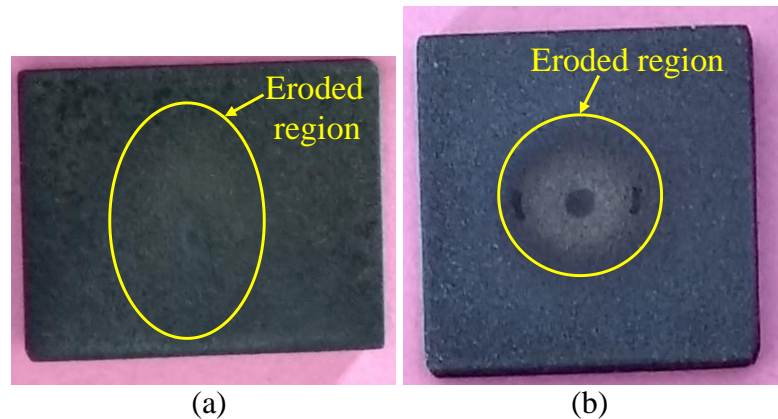
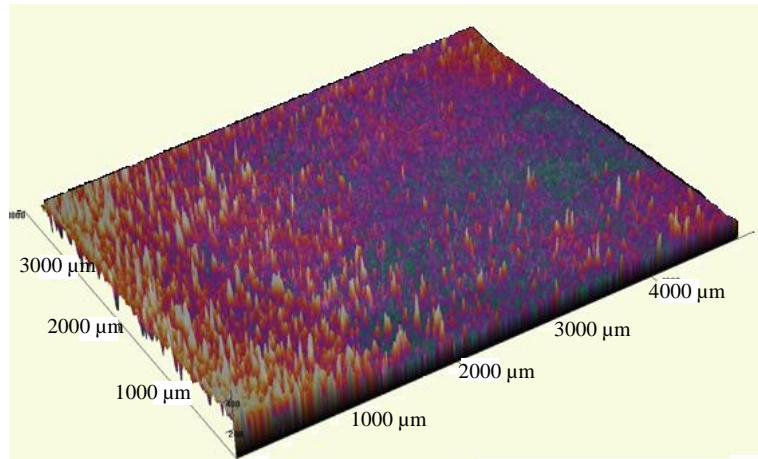


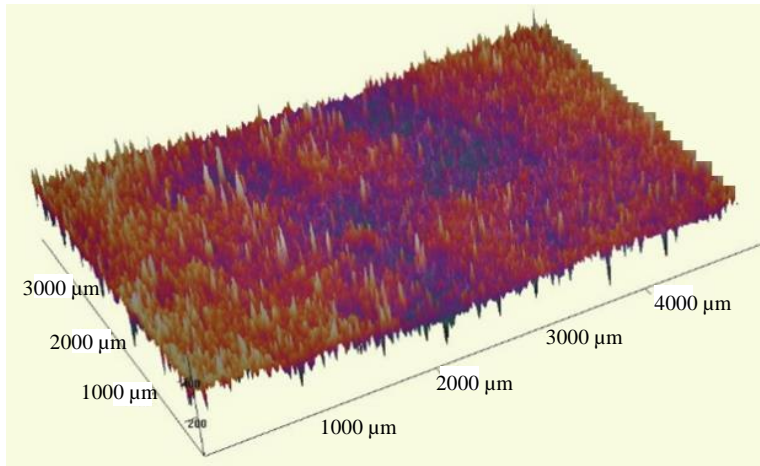
Figure 3.26 The camera photographs of the eroded $\text{Cr}_3\text{C}_2\text{-NiCr/Cenosphere}$ coating at $600\text{ }^\circ\text{C}$ with (a) 30° and (b) 90° impact angles.

The effect of temperature on the erosion rate and volume loss of the coating is demonstrated in Figure 3.29a and Figure 3.29b respectively. It is observed that the erosion rate and volume loss of the coating diminish with increment in temperature for both the impact angles. The erosion rate and volume loss of the coating are lower at 30° in comparison to 90° impact angle. Comparable outcomes are accounted for by Yang et al. (2008) for $\text{Cr}_3\text{C}_2\text{-NiCr}$ coating for boiler tube application. The erosion volume loss at $600\text{ }^\circ\text{C}$ is noted to be 4 times less than that observed at $200\text{ }^\circ\text{C}$. The decline in the erosion volume loss with temperature rise is credited to higher hardness and temperature stability of the constituents present in the coating. At higher temperature ductility of the coating increases, prompting plastic deformation of NiCr binder phase. This reduces the localized brittle cracking of binder phase and hard particles interface (Wang and Shui 2002). In addition, a protective oxide layer of Cr_2O_3 , NiCr_2O_4 , and NiO has been formed at higher temperatures reducing further coating volume loss.

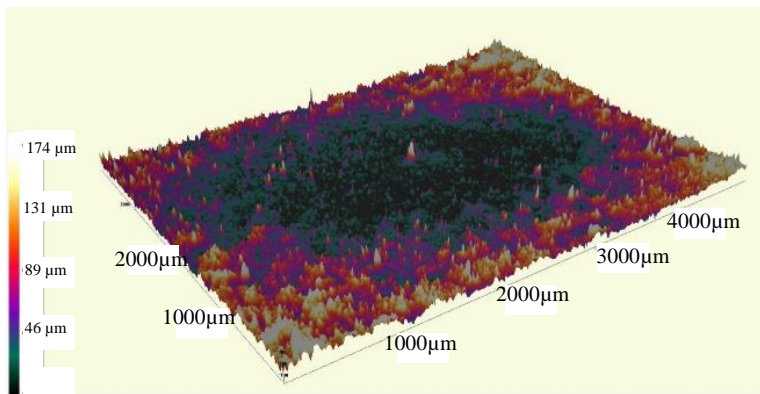
The erosion volume loss at 90° impact angle is more than that at 30° at all the test temperatures, inferring brittle mode of material removal. At 90° impact angle, the region of contact is less for erodent particles and because of strain localization, oxide layer fails to resist impact load by formations of fragments leading to cracks. Accordingly, erosion volume loss is apparently increased.



(a)

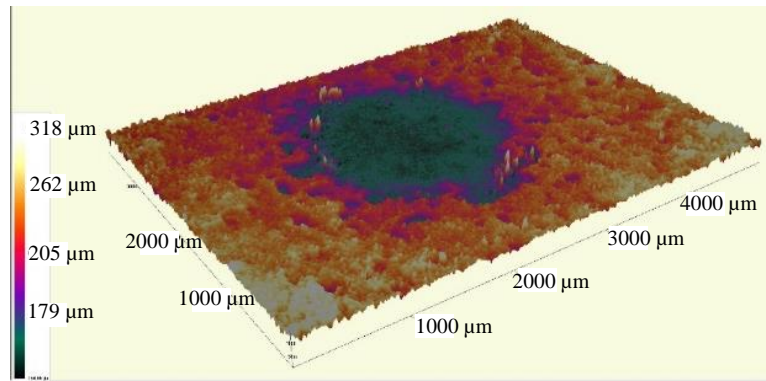


(b)

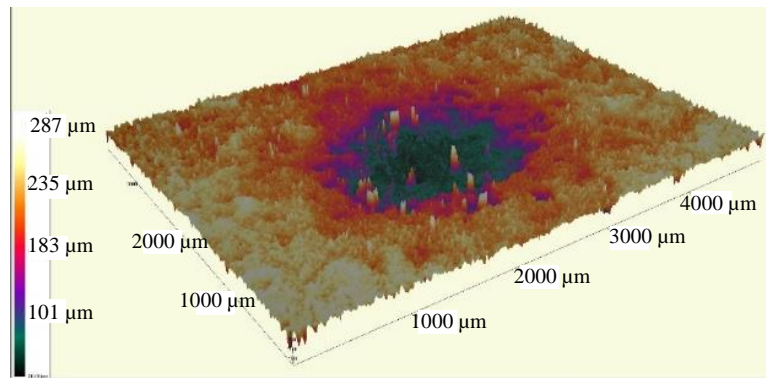


(c)

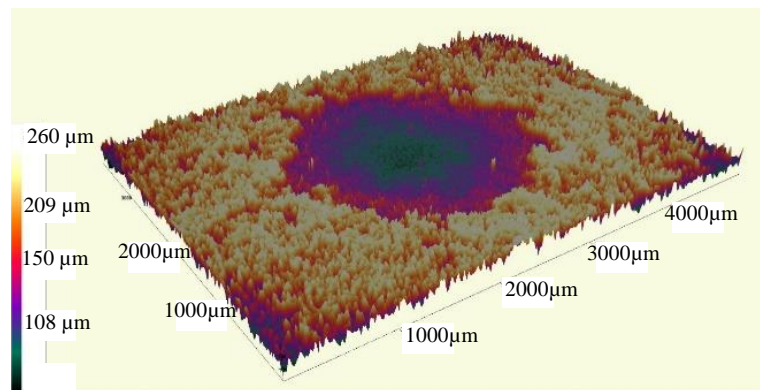
Figure 3.27 Eroded surface 3-D profile of $\text{Cr}_3\text{C}_2\text{-NiCr/Cenosphere}$ coating at (a) 200 (b) 400 and (c) 600 °C with 30° impact angle.



(a)

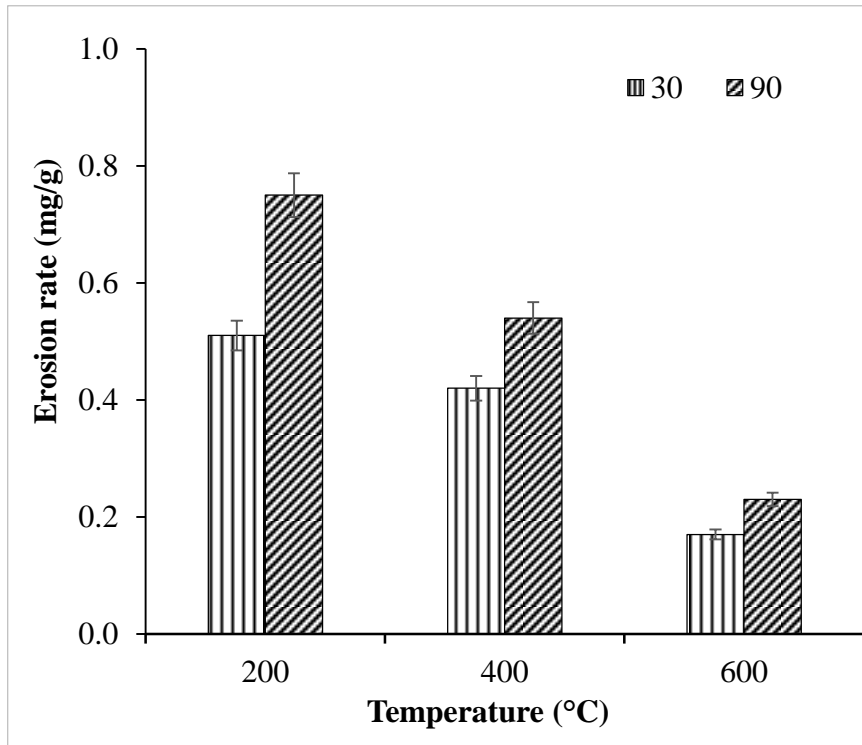


(b)

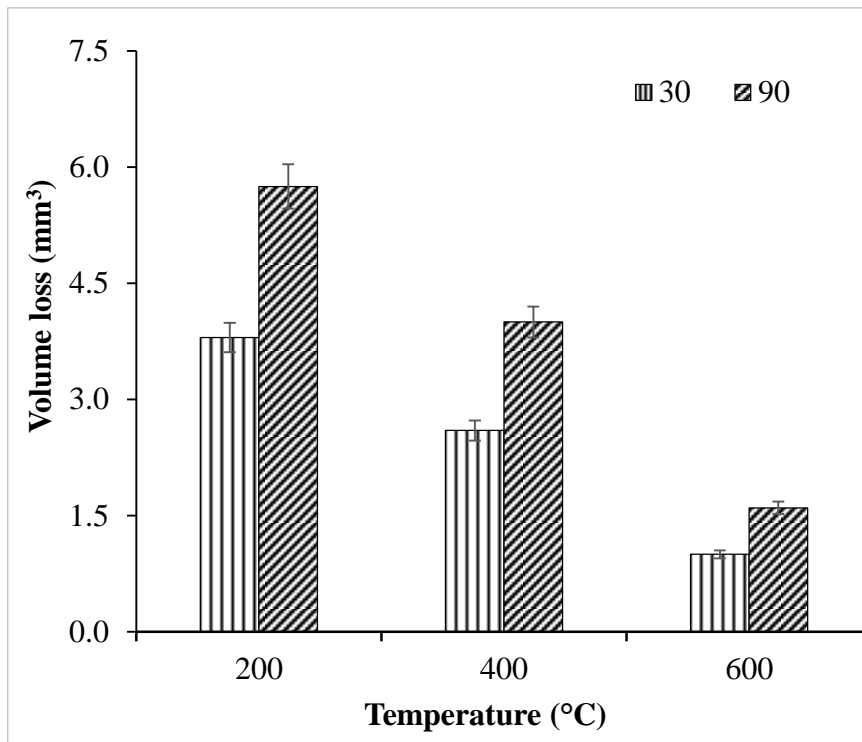


(c)

Figure 3.28 Eroded surface 3-D profile of $\text{Cr}_3\text{C}_2\text{-NiCr/Cenosphere}$ coating at (a) 200 (b) 400 and (c) 600 °C with 90° impact angle.



(a)



(b)

Figure 3.29 (a) erosion rate and (b) volume loss of Cr₃C₂-NiCr/Cenosphere coating as a function of temperature at 30 and 90° impact angles.

Eroded coating XRD pattern of $\text{Cr}_3\text{C}_2\text{-NiCr/Cenosphere}$ coating at 200, 400 and 600 °C are presented in Figure 3.30. Cr, Ni, and Al_2O_3 are major peaks while SiO_2 , $\text{Al}_2\text{O}_3 \cdot 2\text{SiO}_2$, and Al_2SiO_5 are minor peaks. Considerable difference in intensity is not observed for the highest intensity peaks at 200, 400 and 600 °C. There is no evidence of oxide formation at 200 °C. Nevertheless, at elevated temperatures, oxides of active elements of the coating are seen to be formed. NiCr_2O_4 is observed to be formed at 400 °C whereas the presence of Cr_2O_3 , NiCr_2O_4 , NiCrO_3 , and NiO are observed at 600 °C.

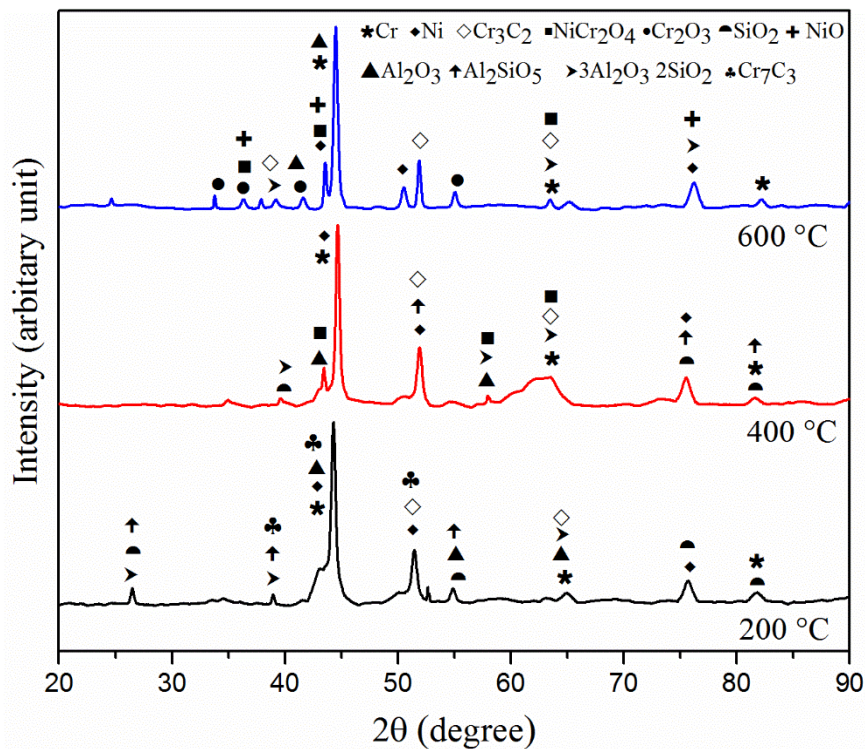


Figure 3.30 XRD pattern of eroded $\text{Cr}_3\text{C}_2\text{-NiCr/Cenosphere}$ coating at different temperatures.

Figure 3.31 shows the morphology of the eroded $\text{Cr}_3\text{C}_2\text{-NiCr/Cenosphere}$ coating surface at 30° impact angle with different temperatures. At this lower angle, hard erodent particles slide on the surface and being in contact for a longer time, form lips by ploughing the binder region. With subsequent impacts, these highly strained lips are vulnerable to get removed as micro-platelets. The EDS analysis at point ‘1’ (ploughing location) in Figure 3.31c confirms the NiCr rich binder phase. In addition, ploughing of the relatively softer binder phase exposes the hard particles to the erodent and further

gouged out by repeated hammering impact of erodent particles leading to small craters formation.

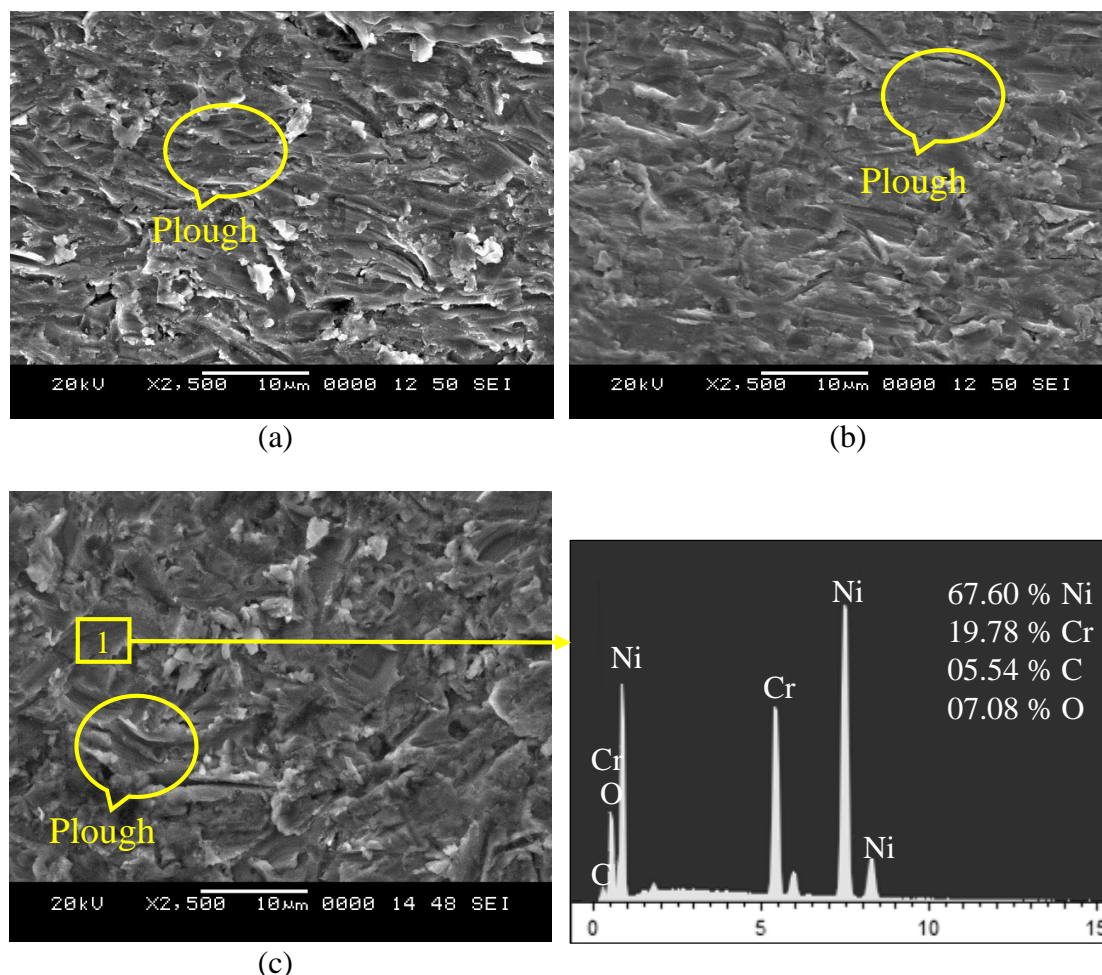


Figure 3.31 Eroded surface SEM micrographs of $\text{Cr}_3\text{C}_2\text{-NiCr/Cenosphere}$ coating at (a) 200 (b) 400 and (c) 600 °C with 30° impact angle.

Morphology of the eroded $\text{Cr}_3\text{C}_2\text{-NiCr/Cenosphere}$ coating surface at 90° impact angle with different temperatures are presented in Figure 3.32. The maximum volume loss has occurred at this angle inferring coating removal by the brittle mechanism. The coating is removed by cracking and chipping owing to strain localization at higher impact angle, which is resulted in the formation of craters as seen in Figure 3.32c. Initially, cracks generate at the interface of the matrix and hard particles as an only one-third interface area are bonded together in plasma spray coatings while remaining area acts as interlamellar gaps which can be considered as pre-existing cracks (Ji et al.

2007). EDS analysis (Figure 3.32c) at point 1 confirms hard particle region, where the indentation mark is formed. With the progress of erosion by erodent, particles cracks are developed and results in chipping of hard particles leading to formation of crater as observed in the micrograph.

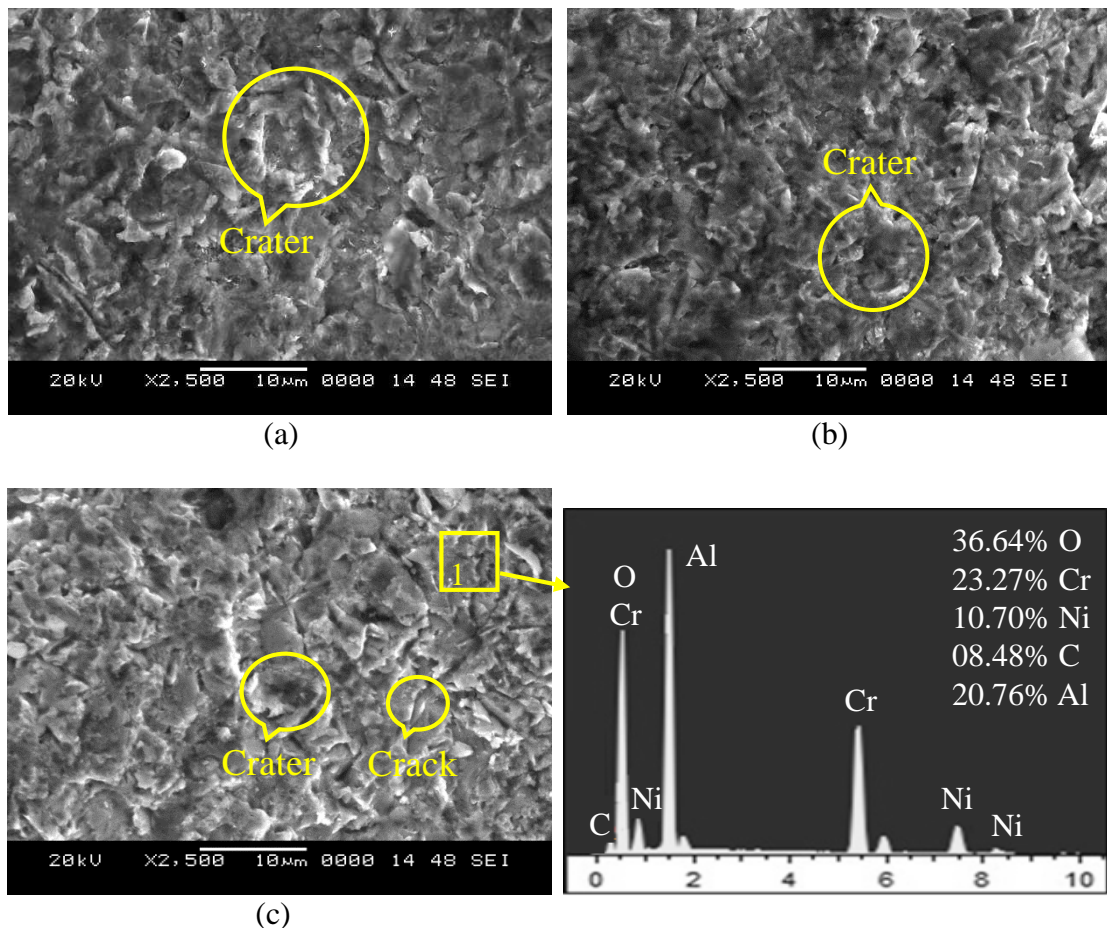
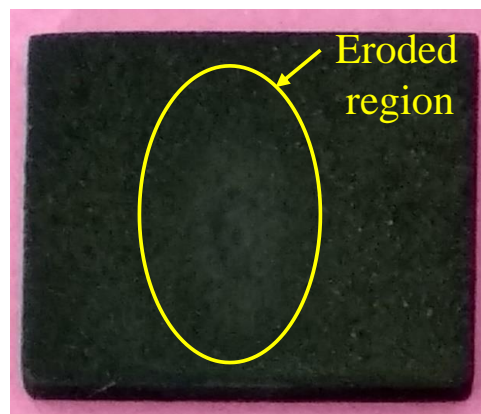


Figure 3.32 Eroded surface SEM micrographs of $\text{Cr}_3\text{C}_2\text{-NiCr/Cenosphere}$ coating at (a) 200 (b) 400 and (c) 600 °C with 90° impact angle.

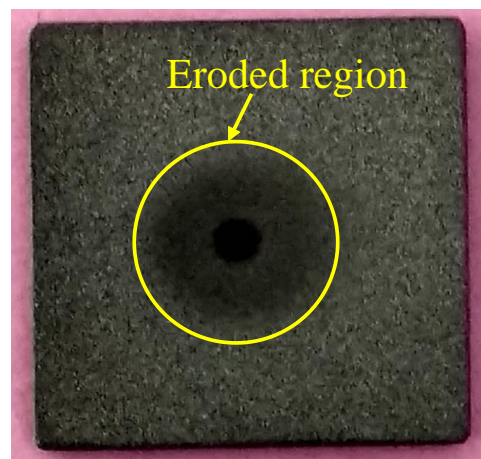
3.7.3 Erosion behaviour of NiCrAlY/WC-Co/Cenosphere coating

Figure 3.33a and Figure 3.33b exhibits the camera photographs of the eroded coating at 600 °C with 30 and 90° impact angles. It is observed from the photographs that eroded region is maximum for 30° impact angle as compared to 90° impact angle. 3-D profiles of eroded coating surface at 30 and 90° impact angles with different temperatures are presented in Figure 3.34 and Figure 3.35 respectively.

The material is removed in a larger area at 30° impact angle (Figure 3.34) indicates erodent particle slides on the surface during the erosion test wherein at 90° impact angle material is removed in a smaller area with more depth of the crater indicates erodent impinging the surface without sliding on the surface.

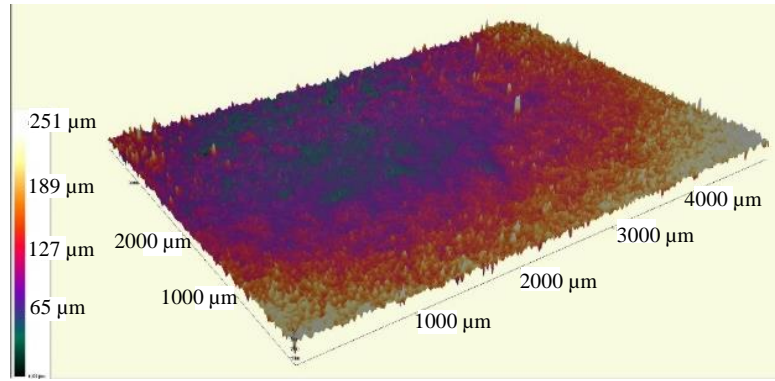


(a)

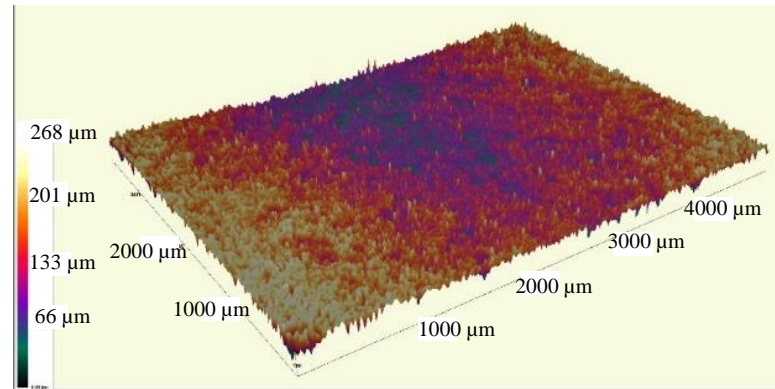


(b)

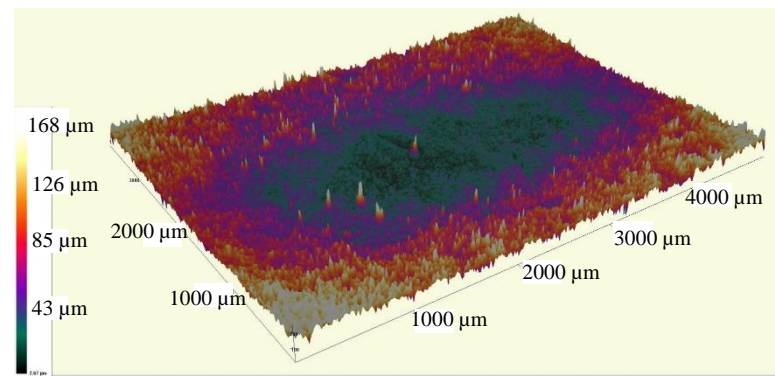
Figure 3.33 The camera photographs of the eroded NiCrAlY/WC-Co/Cenosphere coating at 600 °C with (a) 30 and (b) 90° impact angles.



(a)

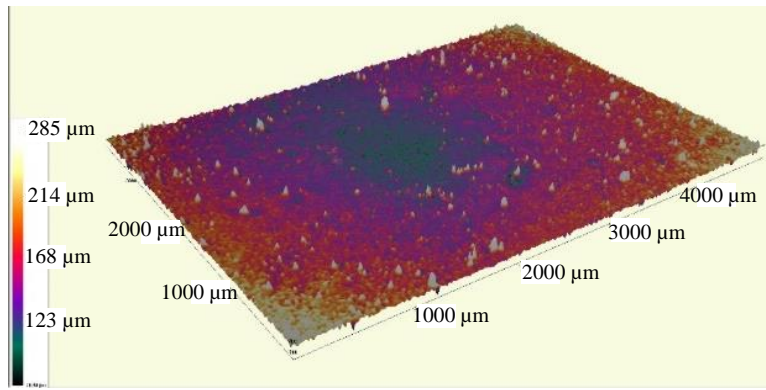


(b)

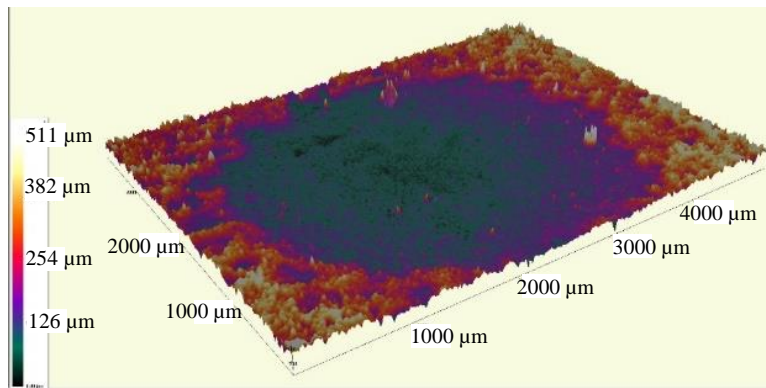


(c)

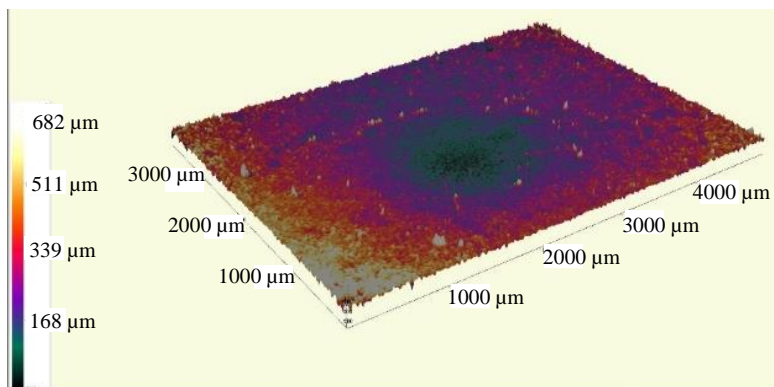
Figure 3.34 Eroded surface 3-D profile of NiCrAlY/WC-Co/Cenosphere coating at (a) 200 (b) 400 and (c) 600 °C with 30° impact angle.



(a)



(b)

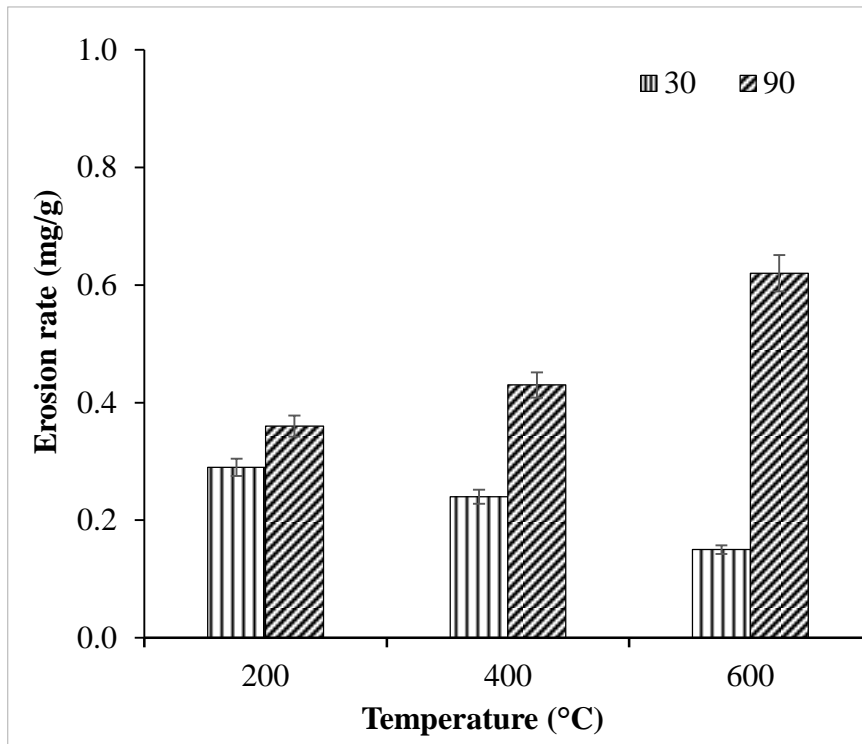


(c)

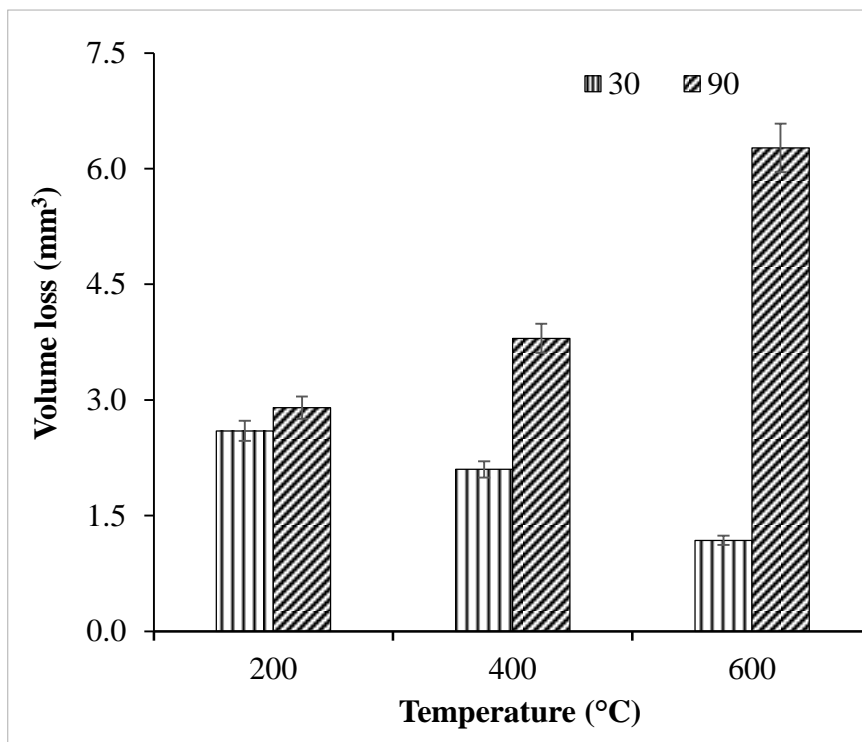
Figure 3.35 Eroded surface 3-D profile of NiCrAlY/WC-Co/Cenosphere coating at (a) 200 (b) 400 and (c) 600 °C with 90° impact angle.

Effect of temperature on the erosion rate and volume loss is presented in Figure 3.36a and Figure 3.36b respectively. At 200°C there is no significant difference in the erosion volume loss (Figure 3.36b) between 30 and 90° impact angles implying neither ductile nor brittle behavior of coating. Similar results are reported by Mishra et al. (2008) for plasma sprayed NiCrAlY coating at room temperature. On the contrary, at higher temperatures, i.e. at 400 and 600 °C, a significant difference in volume loss is observed for both the impact angles. The erosion volume loss at 90° impact angle is higher than that at 30° implying brittle mode of erosion. Praveen et al. (2015) observed the similar behavior for plasma sprayed NiCrSiB/Al₂O₃ coating tested at 450 °C.

Erosion volume loss at 30° impact angle decreased with an increase in test temperature. The volume loss at 600 °C is half the value as observed at 200 °C. At lower impact of 30°, an erodent particle slide on the surface and ploughs the material. Further, as the test temperature increases, the material becomes soft leading to rise in ductility. Coating deforms plastically due to ductility rise and further prevents cracking, in turn, improving erosion resistance. Better erosion resistance at a higher temperature under lower impact angle is due to higher coating hardness (Kulu and Pihl 2002). At lower impact angle, erodent particles slide without initiating brittle cracks in the protective oxide layer leading to higher coating hardness. Erosion volume loss at 90° impact angle is higher at elevated temperature as the area of contact is minimum for erodent particles compared to lower impact angle. Oxide layer being brittle, fractures in fragments leading to multiple cracks. In addition, the presence of W₂C phase at a higher temperature leads to the embrittlement of coating surface leading to the brittle mode of fracture.



(a)



(b)

Figure 3.36 (a) erosion rate and (b) volume loss of NiCrAlY/WC-Co/Cenosphere coating as a function of temperature at 30 and 90° impact angles.

Figure 3.37 depicts the XRD pattern of eroded samples at 200, 400 and 600 °C. XRD pattern consists of AlNi, Al₂O₃, and SiO₂ as major phases and W₂C minor phase. As seen in Figure 3.37 similar patterns are seen at all the temperatures. NiO, NiAl₂O₄, Al₂O₃, and CoWO₄ are observed at 600 °C due to oxidation. These oxides form a protective layer and resist erosion at elevated temperature.

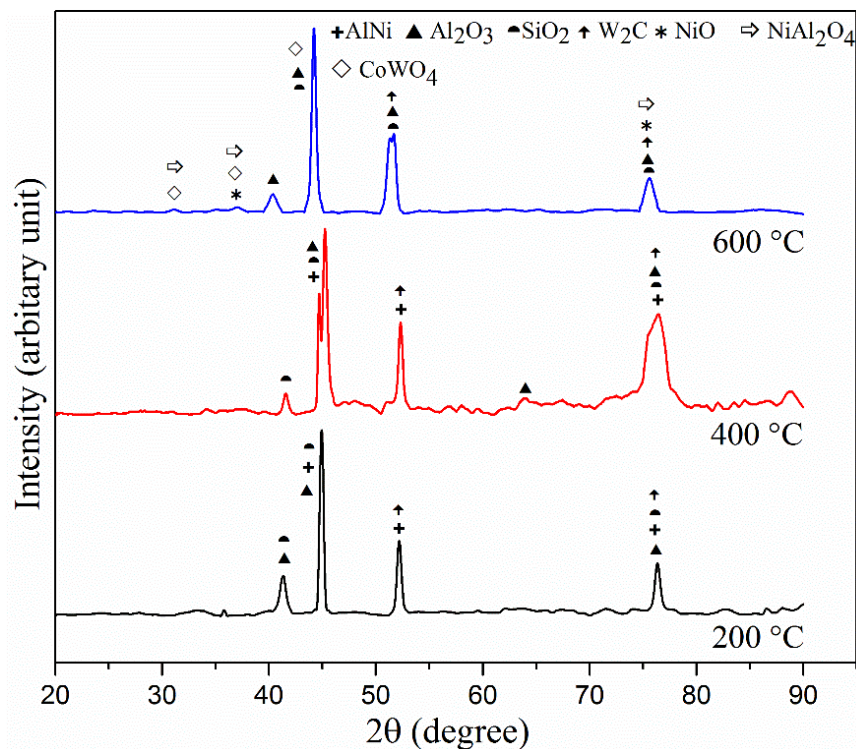


Figure 3.37 XRD pattern of eroded NiCrAlY/WC-Co/Cenosphere coating at different temperatures.

Morphology of the eroded NiCrAlY/WC-Co/Cenosphere coating surfaces at 30° impact angle with different temperatures is exhibited by Figure 3.38. A number of grooves and lips are observed at this angle indicating material removal by ploughing and micro cutting. At lower impact angles, hard erodent particles slide on the surface and being in contact for a long time leads to micro ploughing of the relatively soft binder phase. EDS analysis (Figure 3.38c) at point 1 confirms the NiCr rich binder matrix where ploughing took place. Such ploughing exposes harder particles to the erodent and subsequently gouged out by repeated hammering effect of erodent particles. This, in turn, initiates small cracks across the boundary of the matrix and hard

particles creating smaller size craters. Murthy et al. 2001, Ramesh et al. 2010 reported similar pullout phenomena in WC-Co/NiCrFeSiB and WC-Co-Cr coating.

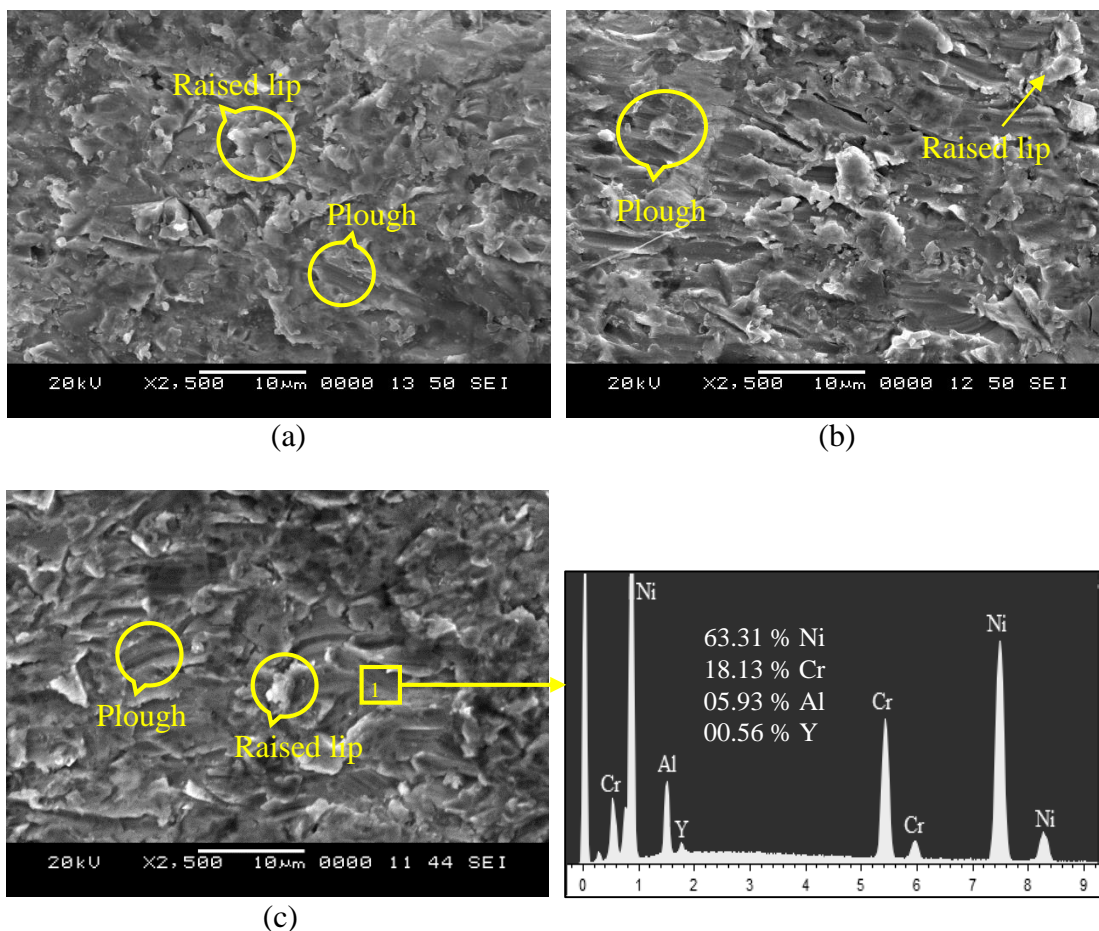


Figure 3.38 Eroded surface SEM micrographs of NiCrAlY/WC-Co/Cenosphere coating at (a) 200 (b) 400 and (c) 600 °C with 30° impact angle.

Figure 3.39 depicts the morphology of the eroded NiCrAlY/WC-Co/Cenosphere coating surface at 90° impact angle with different temperatures. The maximum erosion volume loss occurred at higher impact angle implying a brittle mode of material removal. Craters and cracks are observed due to strain localization leading to brittle fracture of splats. Cracks are generated at the interface of the matrix and hard particles as an only one-third interface area are bonded together in plasma spray coatings while remaining area acts as interlamellar gaps which can be treated as pre-existing cracks (Ji et al. 2007). With the progress of erosion, radial and lateral cracks are developed on the surface and sub-surface of the coating. These cracks interlock with the pre-existing

non bonded area and remove the lamella or lamellae. EDS analysis (Figure 3.39c) at point 1 confirms the cenosphere particle owing to the presence of Al and Si oxides. Crack gets initiated at the particle boundary leading to particle removal by repetitive erodent impact.

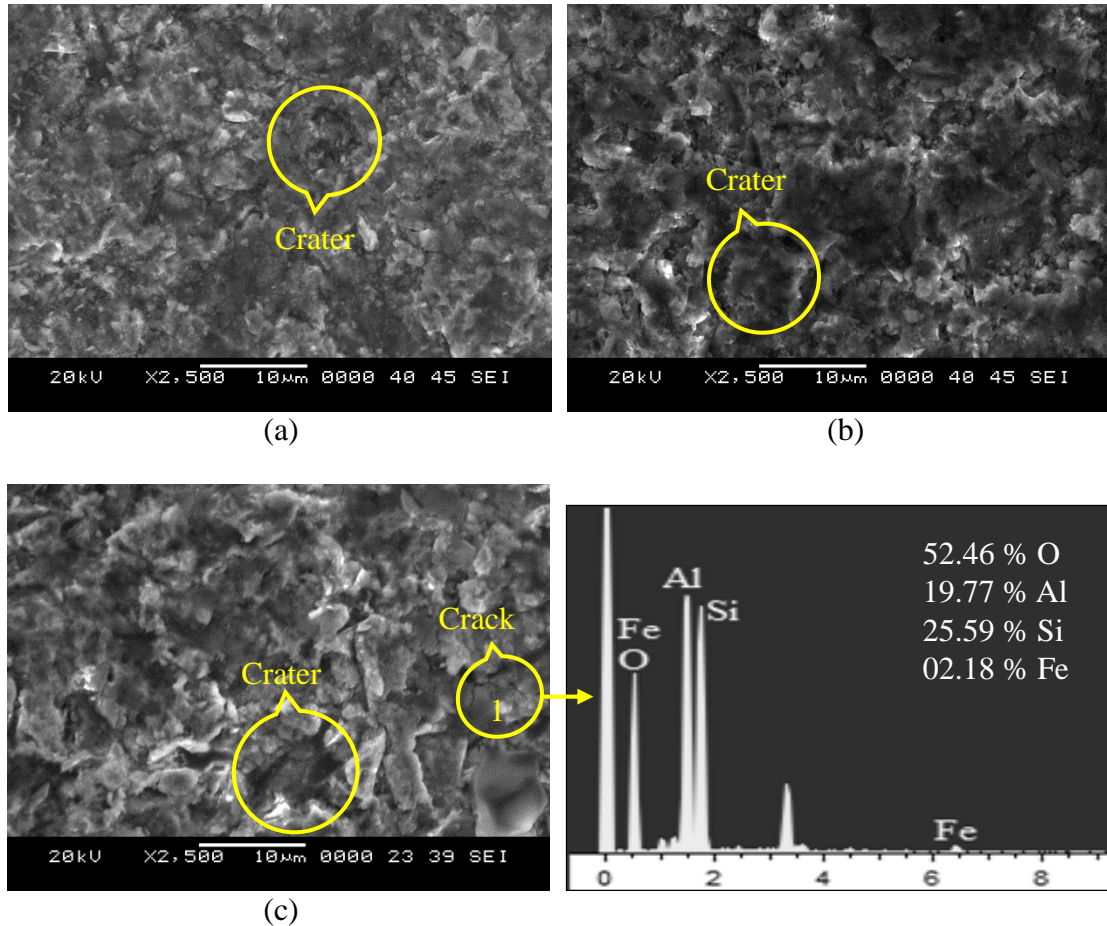
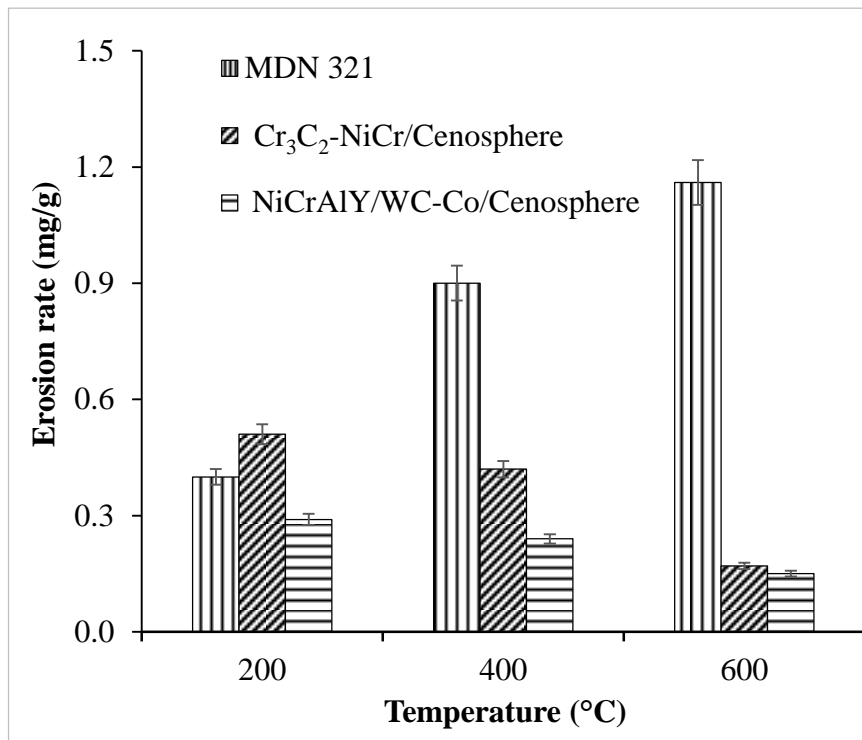


Figure 3.39 Eroded surface SEM micrographs of NiCrAlY/WC-Co/Cenosphere coating at (a) 200 (b) 400 and (c) 600 °C with 90° impact angle.

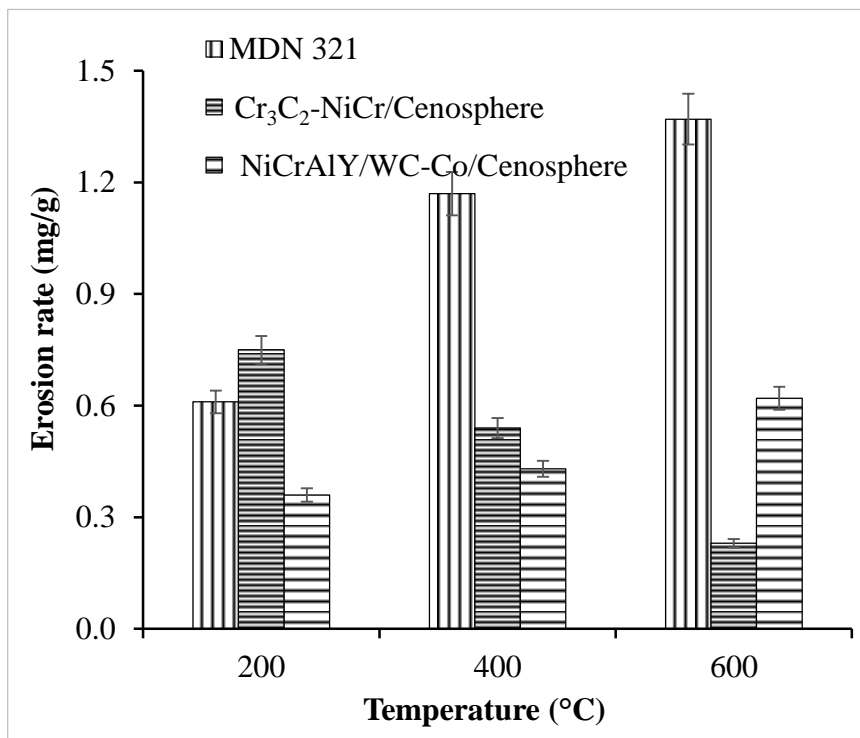
3.7.4 Comparative discussion

Figure 3.40 presents the erosion rate of MDN 321 steel, Cr₃C₂-NiCr/Cenosphere, and NiCrAlY/WC-Co/Cenosphere coatings as a function of temperature at 30 and 90° impact angles respectively. Both the coatings registered lower erosion rate at 30 and 90° impact angles as compared to MDN 321 steel is attributed to high hardness of the coatings, high-temperature stability of the coating constituents and oxidation resistance of the coatings (Kulu and Pihl 2002). Relative erosion resistance of the MDN 321 steel and coatings can be arranged in the following sequence:

NiCrAlY/WC-Co/Cenosphere coating > Cr₃C₂-NiCr/Cenosphere coating > MDN 321 steel.



(a)



(b)

Figure 3.40 Erosion rate of MDN 321 steel, Cr₃C₂-NiCr/Cenosphere and NiCrAlY/WC-Co/Cenosphere coatings as a function of temperature at (a) 30 and (b) 90° impact angles.

NiCrAlY/WC-Co/Cenosphere coating exhibited higher erosion resistance. Similar higher erosion resistance of the WC-12Co coating is reported in the literature (Vicenzi et al. 2006) as compared to Cr₃C₂-NiCr and WC-CrC-Ni. At higher temperature materials become soft leading to rise in ductility. Coating deforms plastically due to ductility rise and further prevents cracking and improves the erosion resistance. NiCrAlY/WC-Co/Cenosphere coating consists of NiCrAlY matrix and WC-Co hard reinforcement. During erosion, NiCrAlY matrix deforms plastically due to the ductility of the matrix and hard WC-Co reinforcement resist the matrix plough thereby reduces the erosion loss. In case of Cr₃C₂-NiCr/Cenosphere coating, the percentage of NiCr matrix is less as compared to NiCrAlY matrix that leads to the localized brittle cracking of the binder phase and hard particle interface and removes the maximum material.

3.8 Oxidation Studies

3.8.1 Visual observations

Camera photographs of the MDN 321 steel, Cr₃C₂-NiCr/Cenosphere, and NiCrAlY/WC-Co/Cenosphere coatings subjected to cyclic oxidation in air at 600 °C for 20 cycles are presented in Figure 3.41. At the end of the oxidation cycles, dark brown and reddish brown color oxide scale is noticed on the surface of Cr₃C₂-NiCr/Cenosphere and NiCrAlY/WC-Co/Cenosphere coatings respectively. Coatings are seen to be in good contact with the substrate during the course of cyclic oxidation studies. The oxide scale is found to be compact, smooth and no spalling or cracks are seen.

3.8.2 Thermogravimetric behaviour

The plots of cumulative weight gain and weight gain square as a function of a number of cycles of MDN 321 steel, Cr₃C₂-NiCr/Cenosphere, and NiCrAlY/WC-Co/Cenosphere coatings are presented in Figure 3.42a and Figure 3.42b respectively. The rapid increase in the weight gain is observed in the initial 5 cycles, thereafter a gradual increase in weight gain is observed for the remaining cycles. The weight gain after 20 cycles for MDN 321 steel, Cr₃C₂-NiCr/Cenosphere and NiCrAlY/WC-Co/Cenosphere coatings is 0.85, 0.77 and 0.74 mg/cm² respectively. Both the coatings

exhibited lower weight gain as compared to MDN 321 steel owing to the formation of a protective oxide layer on the surface. Figure 3.42b depicts the plot of weight gain square versus a number of cycles. The oxidation behavior of substrate as well as coatings is parabolic in nature up to 20 cycles. Kinetics of oxidation is approximated by the parabolic rate law. The parabolic rate constant (K_p) (Sahu et al. 2010) is calculated using the linear least square fit method in the form of :

$$\left(\frac{dW}{A}\right)^2 = K_p \times t \quad (2)$$

where, dW/A is the weight gain per unit area, t is the oxidized time in seconds. The parabolic rate constants (K_p in $10^{-10} \text{g}^2 \text{cm}^{-4} \text{s}^{-1}$) for MDN 321 steel, Cr_3C_2 -NiCr/Cenosphere and NiCrAlY/WC-Co/cenosphere coatings is 0.099, 0.0317 and 0.0282 respectively.

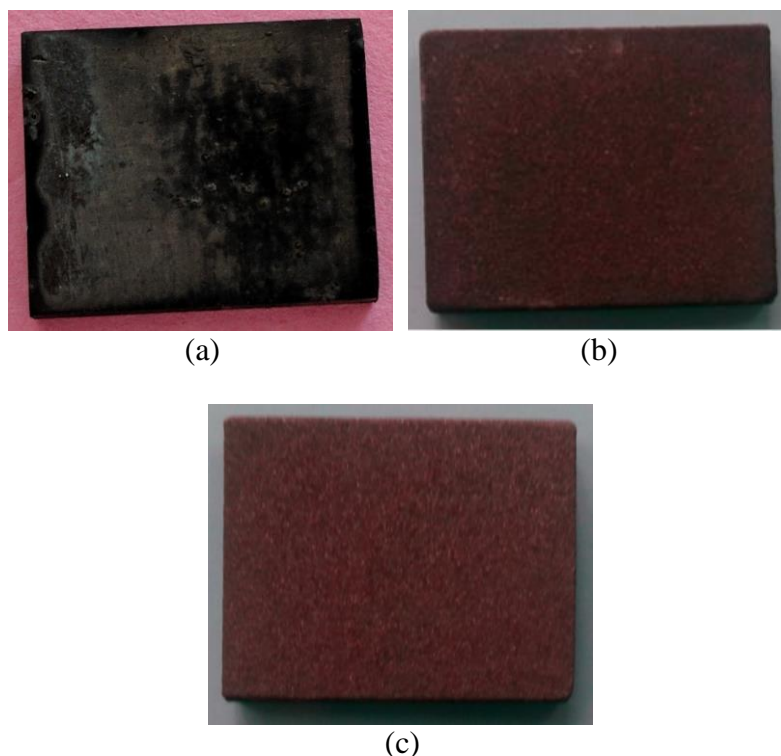
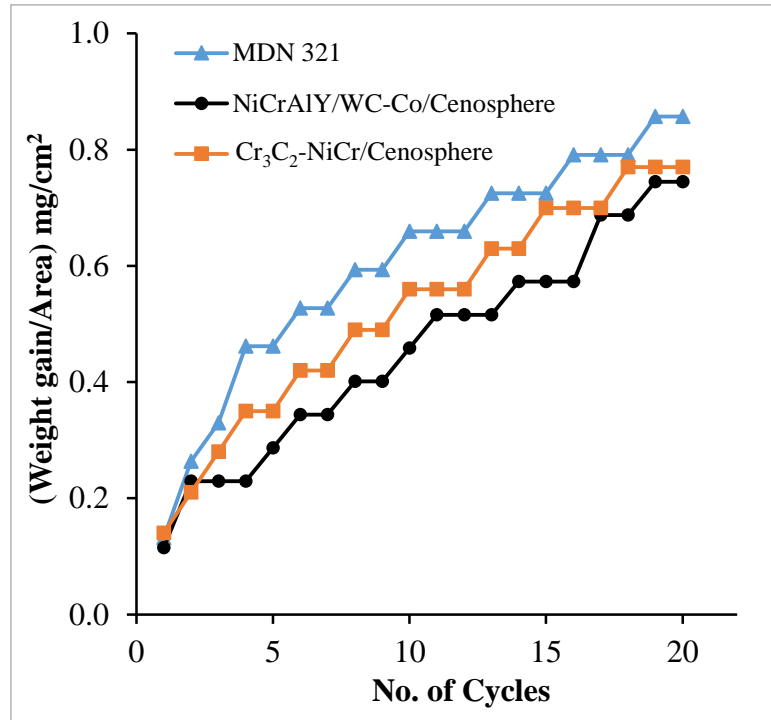
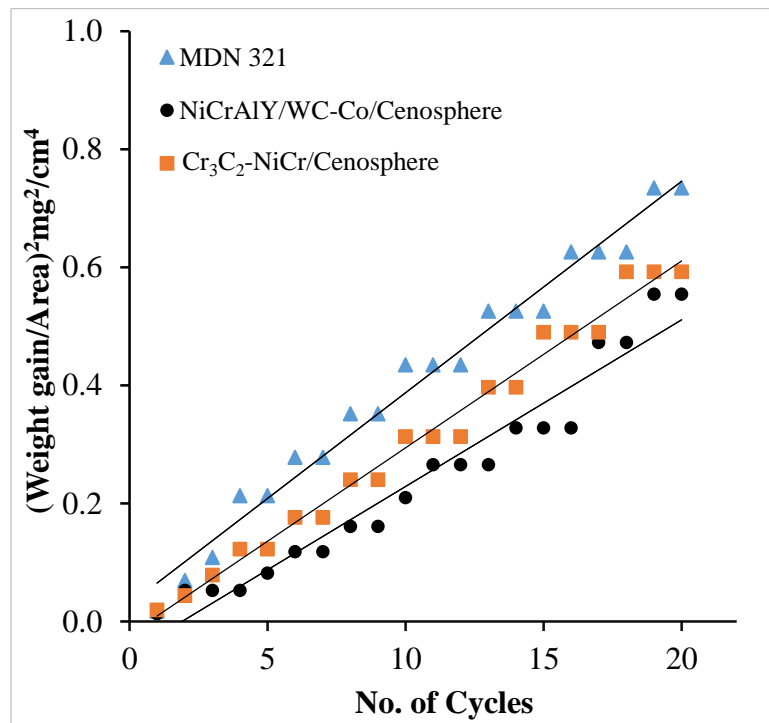


Figure 3.41 The camera photographs of (a) MDN 321 steel (b) Cr_3C_2 -NiCr/Cenosphere and (c) NiCrAlY/WC-Co/cenosphere coatings subjected to cyclic oxidation at 600 °C in air for 20 cycles.



(a)



(b)

Figure 3.42 Plot of oxidation cycles (a) weight gain per unit area (b) square of weight gain per unit area.

3.8.3 XRD analysis

XRD pattern of Cr_3C_2 -NiCr/Cenosphere coating oxidized at $600\text{ }^\circ\text{C}$ is shown in Figure 3.43. Cr_{23}C_6 , Al_2O_3 , Cr, and Ni are found as a major phases and SiO_2 is found as minor phase. Cr_2O_3 and NiCr_2O_4 oxides are observed in the XRD pattern as result of oxidation. These oxides form the protective oxide scale on the surface of the coating thereby protects the coating.

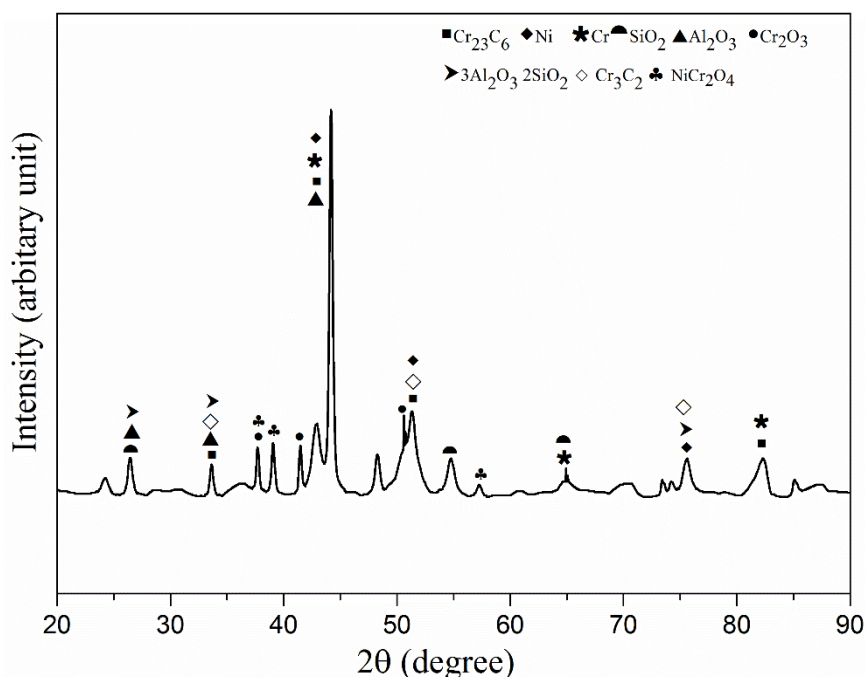


Figure 3.43 XRD pattern of Cr_3C_2 -NiCr/Cenosphere coating oxidized at $600\text{ }^\circ\text{C}$.

Figure 3.44 presents the XRD pattern of NiCrAlY/WC-Co/Cenosphere coating oxidized at $600\text{ }^\circ\text{C}$. XRD pattern depicts Al_2O_3 , SiO_2 , and AlNi_3 as major and W_2C as a minor phase. XRD pattern also consists of WO_3 , AlNi_3 , Cr_2O_3 , NiO oxides and spinel oxide of CoWO_4 owing to oxidation.

3.8.4 Surface and cross-sectional analysis of scale

Surface morphology of the oxidized Cr_3C_2 -NiCr/Cenosphere coating with EDS analysis is presented in Figure 3.45. EDS analysis depicts that the scale is mainly consisting of Ni, Cr, Al, Si, and O, implies the possibility of formation oxides of Ni, Cr, Al, and Si. XRD results (Figure 3.43) of oxidized coating also confirms the existence of Al_2O_3 , Cr_2O_3 and SiO_2 oxides on the surface.

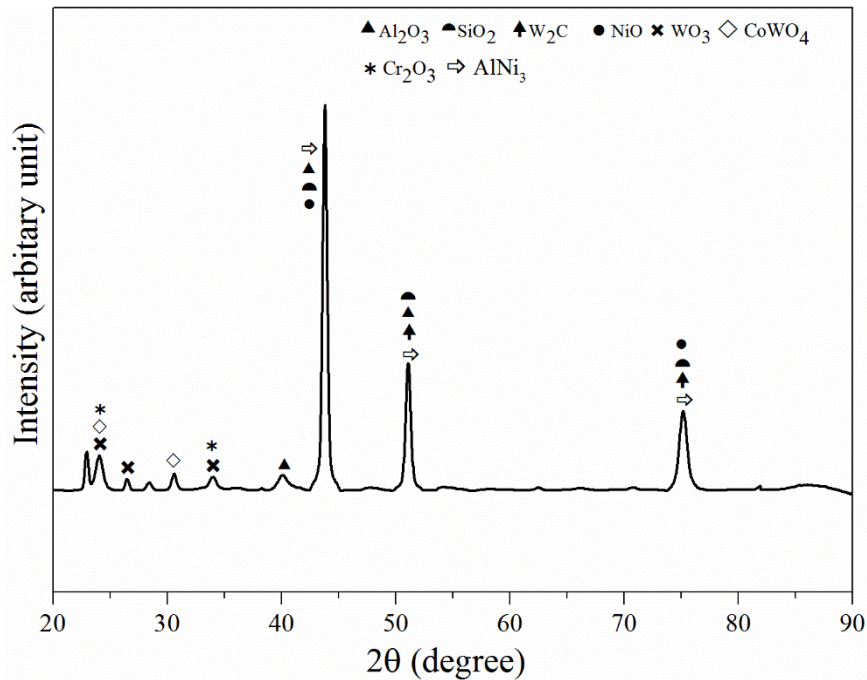


Figure 3.44 XRD pattern of NiCrAlY/WC-Cenosphere coating oxidized at 600 °C.

The protective oxide layer is formed on the coating surface from the oxides there by restricts the entry of oxygen into the coating (Somasundaram et al. 2014).

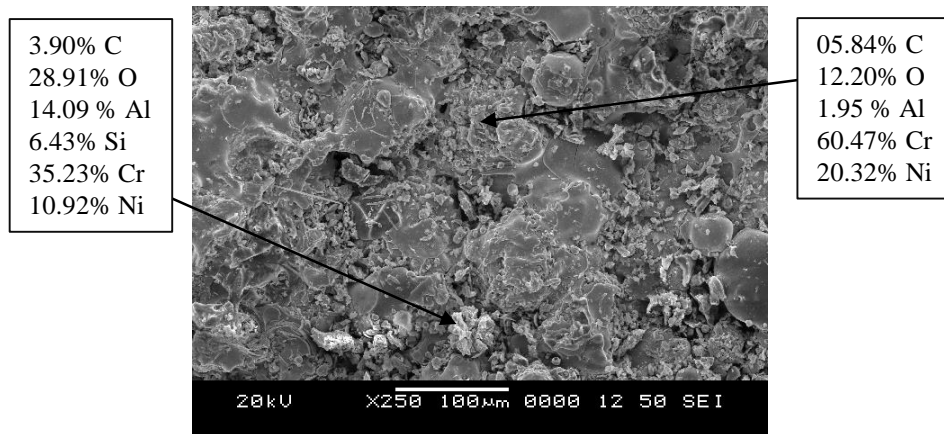


Figure 3.45 Surface morphology and EDS analysis of oxidized Cr_3C_2 -NiCr/Cenosphere coating at 600 °C.

Cross-sectional elemental X-ray mapping of Cr_3C_2 -NiCr/Cenosphere coating subjected to cyclic oxidation for 20 cycles is shown in Figure 3.46. X-ray mapping revealed that the topmost layer is rich in Ni, Cr and O indicates the formation of NiO and Cr_2O_3

oxides. The oxide scale formed on the surface acts as a barrier to the inward diffusion of oxygen and other oxidizing elements into the coating.

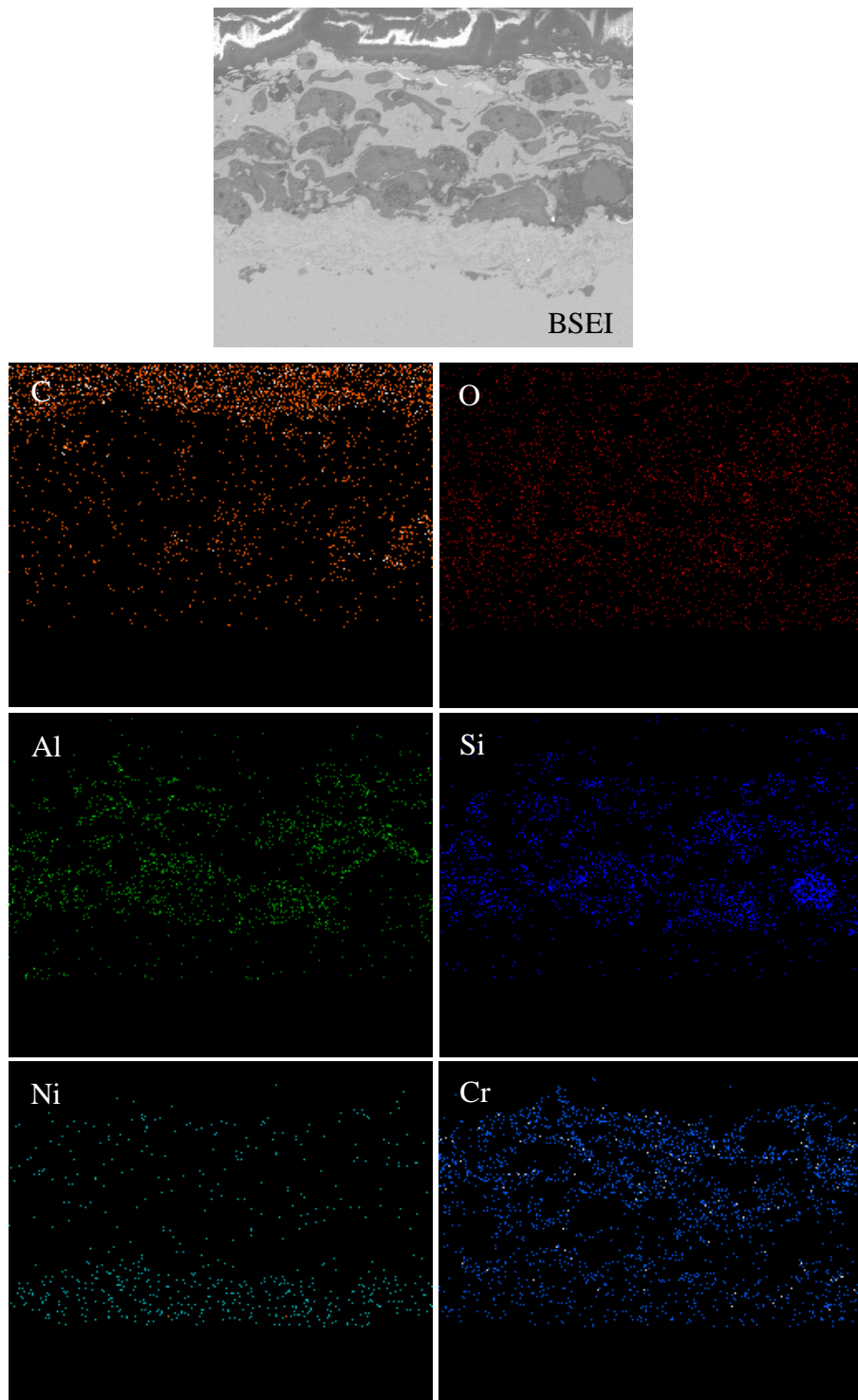


Figure 3.46 Cross sectional X-ray mapping of oxidized $\text{Cr}_3\text{C}_2\text{-NiCr/Cenosphere}$ coating at $600\text{ }^\circ\text{C}$.

Figure 3.47 shows the surface morphology with EDS analysis of the oxidized NiCrAlY/WC-Co/Cenosphere coating. EDS analysis of oxidized surface reveals the presence Ni, Cr, Al, W and O as main constituents that denotes the presence of its oxides and spines. XRD pattern (Figure 3.44) of oxidized coating also demonstrates the existence of Al₂O₃, NiO, Cr₂O₃, and CoWO₄ oxides on the surface. The formed oxides restrict the penetration of oxygen into the coating by forming a protective oxide layer on the top surface. Hence only the top surface of the coating has undergone oxidation increasing the oxidation resistance of the coating.

Cross-sectional elemental X-ray mapping of NiCrAlY/WC-Co/Cenosphere coating subjected to cyclic oxidation for 20 cycles is presented in Figure 3.48. X-ray mapping shows the distribution of O, Al, Si, Cr, Ni and W in the coating. Dense oxygen is observed towards the top layer depicts the presence of oxides on the top layer. Distribution of oxygen inside the coating is also observed which is due to cenosphere presence in the coating.

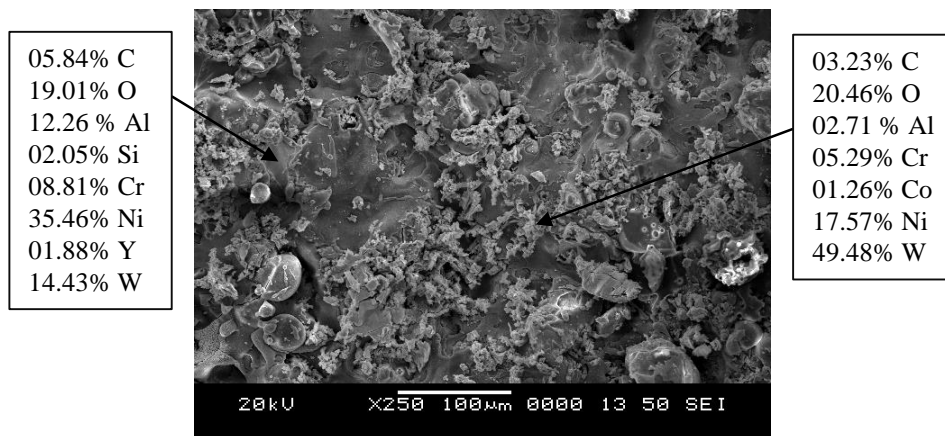


Figure 3.47 Surface morphology and EDS analysis of oxidized NiCrAlY/WC-Co/Cenosphere coating at 600 °C.

3.8.5 Comparative discussion

Cr₃C₂-NiCr/Cenosphere and NiCrAlY/WC-Co/Cenosphere coatings exhibited higher oxidation resistance as compared to MDN 321 steel. Protective thin oxide scale formed during oxidation imparted better oxidation resistance to the coatings. Based on the

thermogravimetric data, the relative oxidation resistance of the MDN 321 steel and coatings can be arranged in the following sequence:

NiCrAlY/WC-Co/Cenosphere coating > Cr₃C₂-NiCr/Cenosphere coating > MDN 321 steel.

The better oxidation resistance of NiCrAlY/WC-Co/Cenosphere coating is attributed to the superior oxidation resistance property of NiCrAlY matrix as compared to Cr₃C₂-NiCr. Further, continuous and protective thin oxide scale consisting of oxides of Cr, Al and Ni and mixed spinel-type oxides of CoWO₄ increased the resistance to oxidation. The formation of Cr₂O₃ and Al₂O₃ protective oxide layer formed during the subsequent stages of oxidation enhancing oxidation resistance.

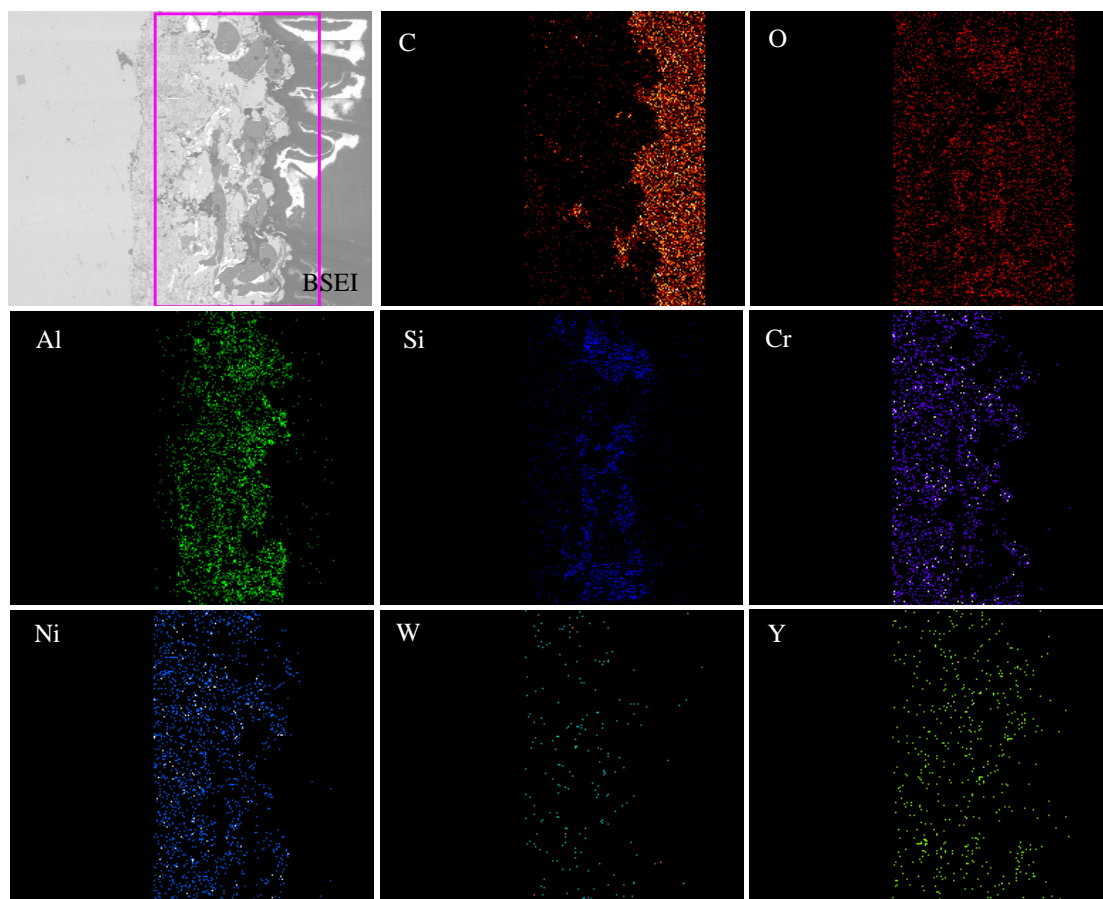


Figure 3.48 Cross sectional X ray mapping of oxidized NiCrAlY/WC-Co /Cenosphere coating at 600 °C.

3.9 Wear studies

3.9.1 MDN 321 steel substrate

3.9.1.1 Frictional behaviour

Figure 3.49a and Figure 3.49b demonstrates the variation in the friction coefficient of MDN 321 steel at 200, 400 and 600 °C with sliding velocity of 1.5 and 2.5 m/s at 20 and 40 N normal loads respectively. It is observed that friction coefficient is decreased with increasing sliding velocity and increased with increasing normal load. As the velocity increases, the friction induced temperature at the interface raises which results in softening resulting in lower friction coefficient. With respect to temperature, friction coefficient registered higher value at 400 °C and lower value at 600 °C.

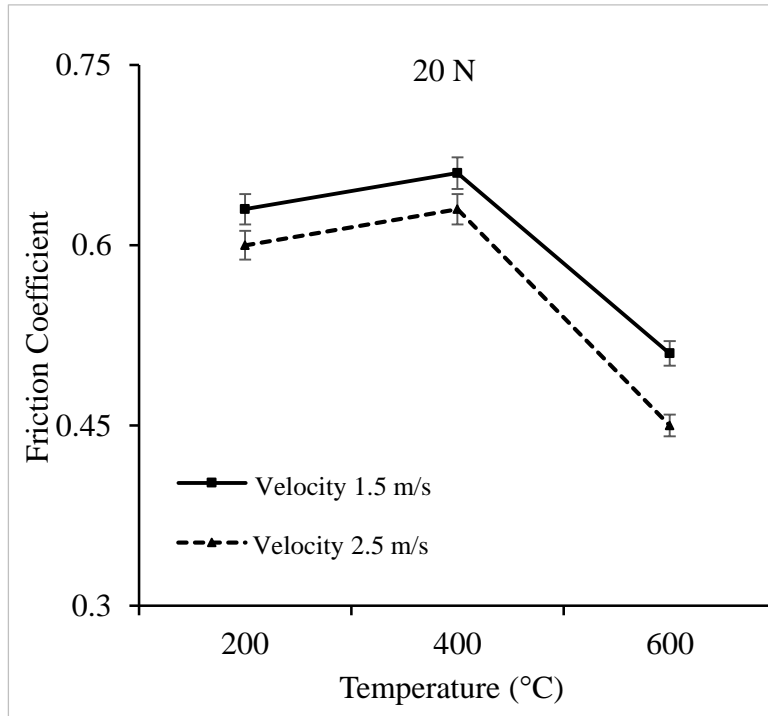
3.9.1.2 Wear rate

Wear rate of MDN 321 steel at 200, 400 and 600 °C with sliding velocity of 1.5 and 2.5 m/s at 20 and 40 N normal loads is shown in Figure 3.50a and Figure 3.50b respectively. Wear rate is observed to increase with increasing load and found to decrease with increase in sliding velocity. Wear rate is found to change with temperature variation. It is minimum at 200 °C and a maximum at 400 °C. This fact infers temperature rise lowers material hardness that leads to higher wear rate.

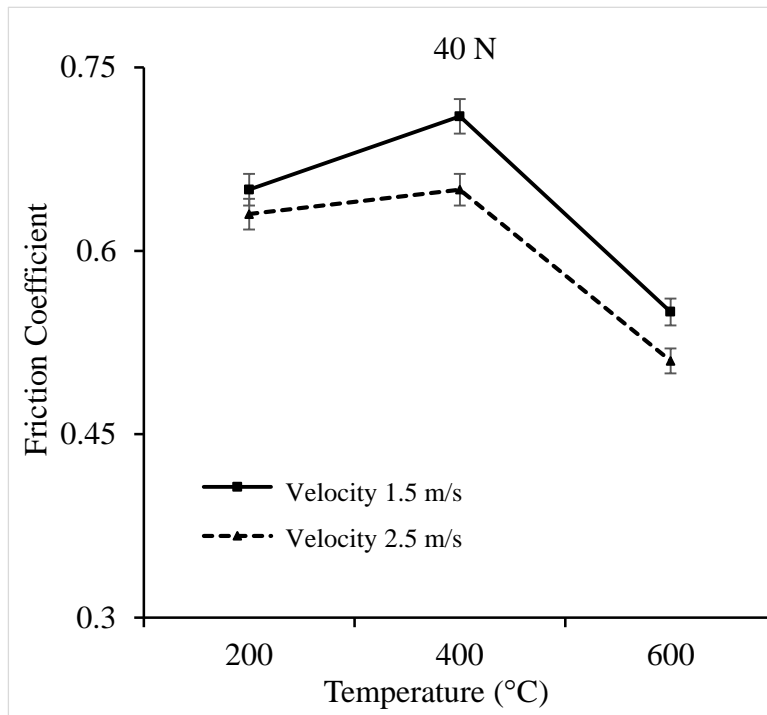
According to Archard's wear equation,

$$Q = \frac{KWL}{H} \quad (3)$$

where, Q - wear volume, W - load, H - hardness of matthe erial, K - constant, L - sliding distance. Wear rate varies inversely with the hardness (Chen et al. 2013). As temperature increases, hardness of the material decreases and wear rate increases. Wear rate at 600 °C is slightly reduced owing to the formation of oxide film.

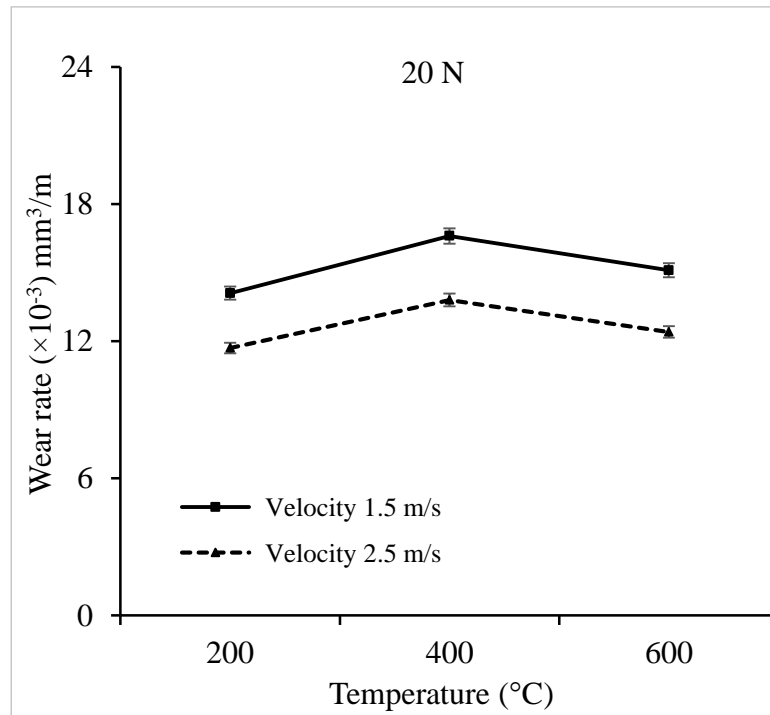


(a)

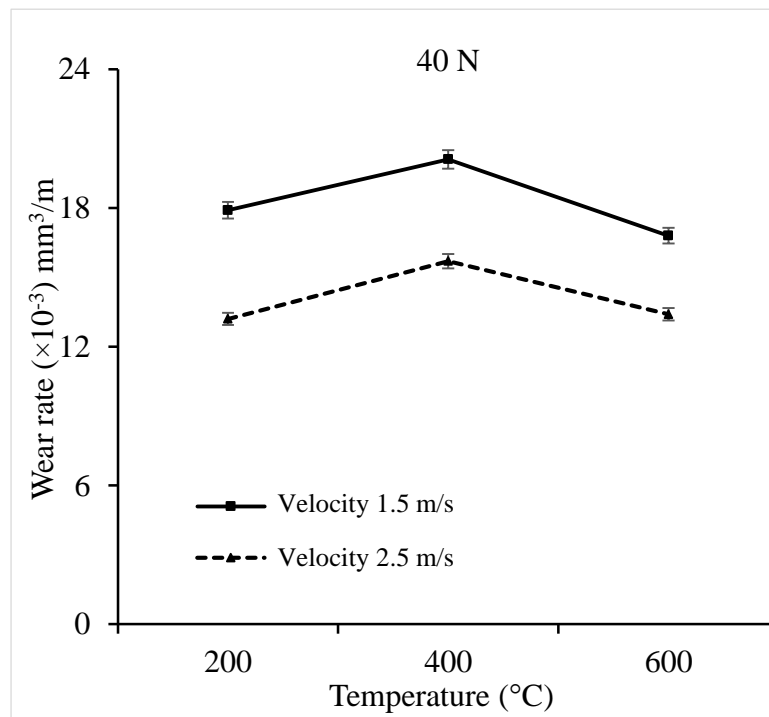


(b)

Figure 3.49 Friction coefficient of MDN 321 steel at sliding velocity of 1.5 and 2.5 m/s with (a) 20 and (b) 40 N normal loads at 200, 400 and 600 °C.



(a)



(b)

Figure 3.50 Wear rate of MDN 321 steel at sliding velocity of 1.5 and 2.5 m/s with (a) 20 and (b) 40 N normal loads at 200, 400 and 600 °C.

3.9.1.3 SEM analysis

Worn surface SEM micrographs of the MDN 321 steel at 1.5 m/s sliding velocity with 40 N normal load and 2.5 m/s sliding velocity with 20 N normal load at 200, 400 and 600 °C temperatures are presented in Figure 3.51 and Figure 3.52 respectively. It can be observed that the worn surfaces are characterized with groove and delamination at all the test temperatures. Grooves are formed as a result of ploughing and exhibit plastic deformation of the material. At 400 °C (Figure 3.51b and Figure 3.52b), worn surfaces are seen to be rough with a number of grooves suggesting drastic wear loss. At 600 °C (Figure 3.51c and Figure 3.52c), worn surfaces look like smooth with minimum grooves implying moderate wear loss. Formation of the oxide layer at an elevated temperature on the contacting surfaces might be the reason for lower wear at 600 °C.

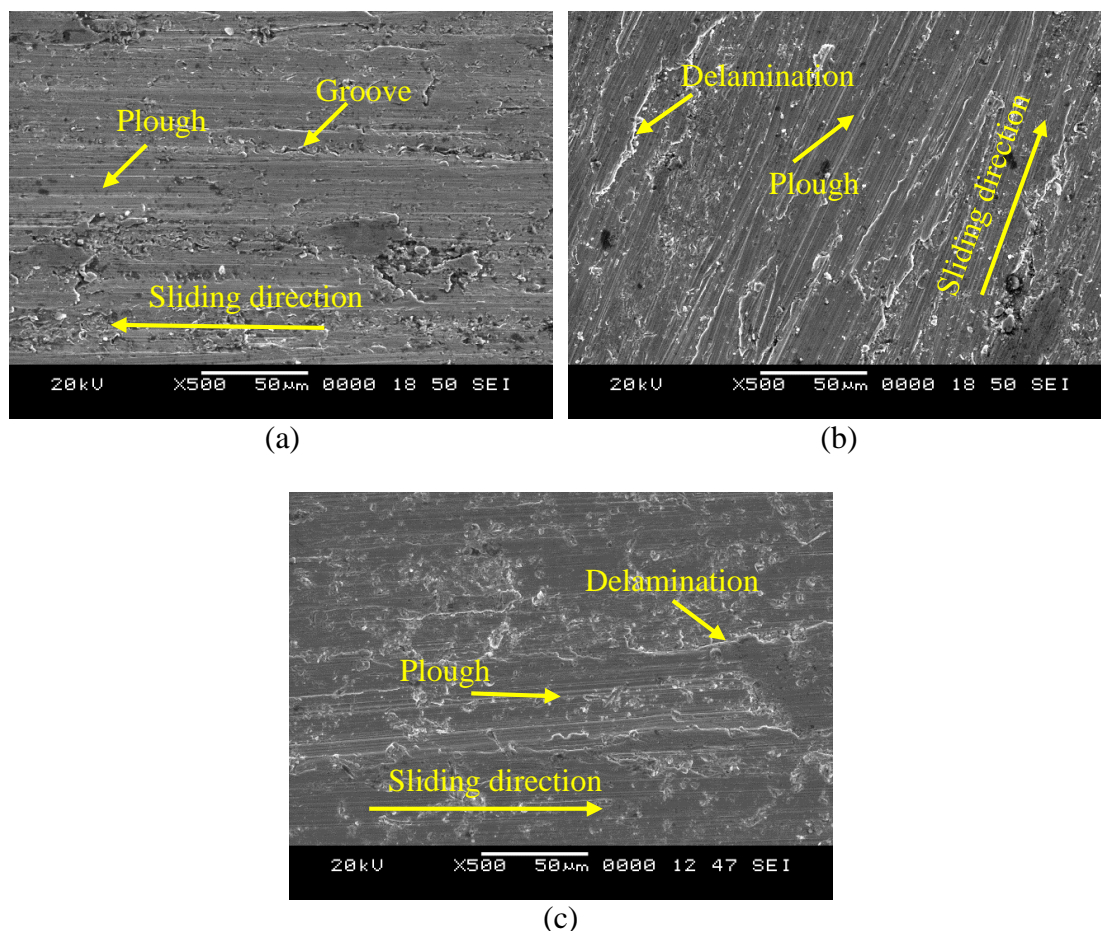
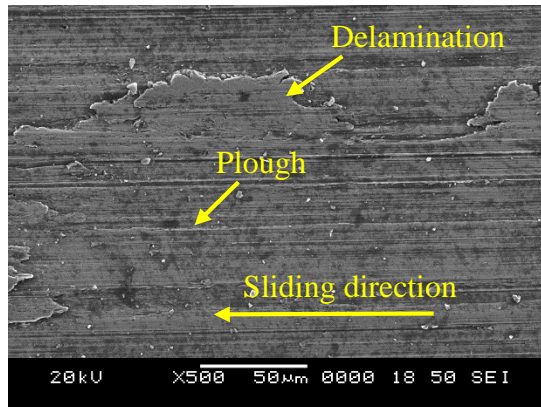
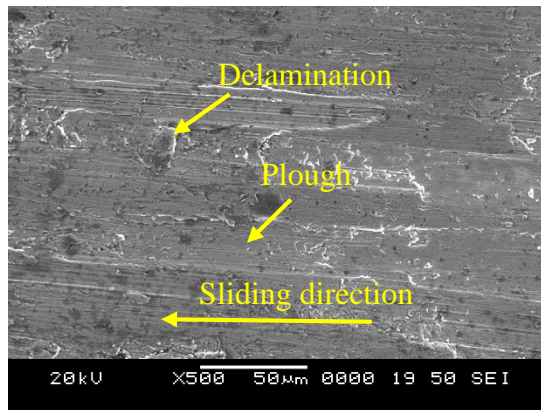


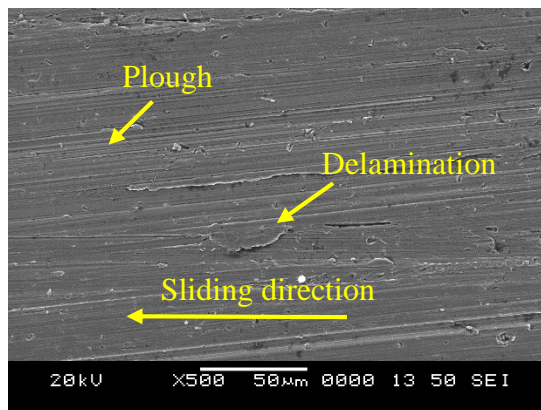
Figure 3.51 Worn surface SEM micrographs of MDN 321 steel with 1.5 m/s sliding velocity and 40 N normal load at (a) 200 (b) 400 and (c) 600 °C.



(a)



(b)



(c)

Figure 3.52 Worn surface SEM micrographs of MDN 321 steel with 2.5 m/s sliding velocity and 20 N normal load at (a) 200 (b) 400 and (c) 600 °C.

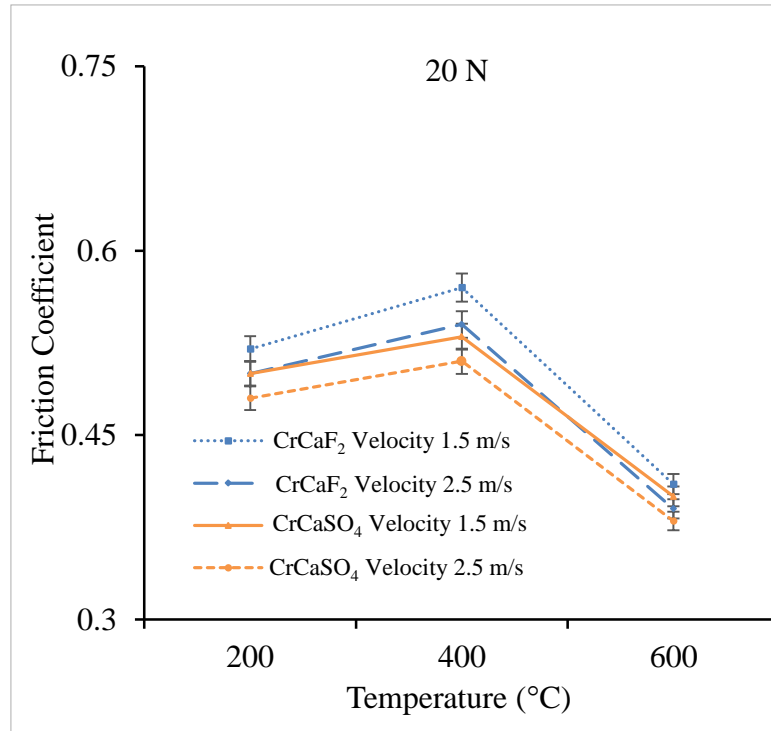
3.9.2 Cr₃C₂-NiCr/Cenosphere/MoS₂/CaF₂ and Cr₃C₂-NiCr/Cenosphere/MoS₂/CaSO₄ coatings

3.9.2.1 Frictional behavior

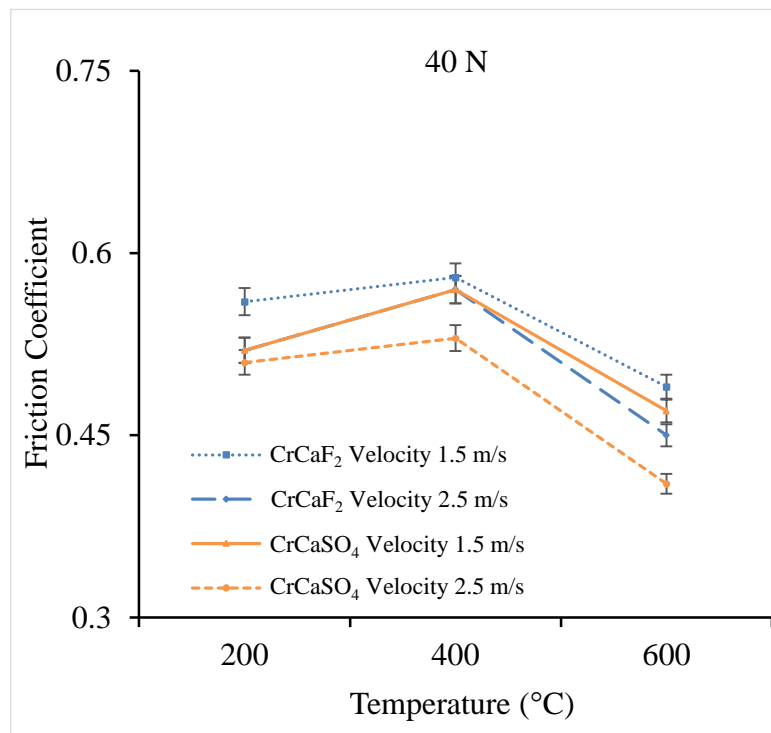
Friction coefficient of Cr₃C₂-NiCr/Cenosphere/MoS₂/CaF₂ (designated as CrCaF₂) and Cr₃C₂-NiCr/Cenosphere/MoS₂/CaSO₄ (designated as CrCaSO₄) coatings at 200, 400 and 600 °C with sliding velocity of 1.5 and 2.5 m/s at 20 and 40 N normal loads is presented in Figure 3.53a and Figure 3.53b respectively. From Figure 3.53a and Figure 3.53b, it is observed that the friction coefficient is decreased with the increase in the sliding velocity and increased with increasing load for both the coatings. With respect to temperature, friction coefficient showed higher value at 400 °C and lower value at 600 °C.

Cr₃C₂-NiCr/Cenosphere/MoS₂/CaF₂ coating exhibited higher friction coefficient as compared to Cr₃C₂-NiCr/Cenosphere/MoS₂/CaSO₄ coating. At 20 N normal load and 1.5 m/s sliding velocity, friction coefficient of Cr₃C₂-NiCr/Cenosphere/MoS₂/CaF₂ and Cr₃C₂-NiCr/Cenosphere/MoS₂/CaSO₄ coatings are in the range of 0.41-0.57 and 0.40-0.53 respectively. At 40 N normal load and 1.5 m/s sliding velocity, friction coefficient of Cr₃C₂-NiCr/Cenosphere/MoS₂/CaF₂ and Cr₃C₂-NiCr/Cenosphere/MoS₂/CaSO₄ coatings are in the range of 0.49-0.58 and 0.47-0.57 respectively.

The lower friction coefficient of the coatings as compared to MDN 321 steel is attributed to lubricity property of MoS₂, CaF₂, and CaSO₄ at wide temperature range. At lower temperature, MoS₂ establishes the lubricating layer between the contacting surfaces thereby lowers the friction coefficient. At elevated temperature, CaF₂ and CaSO₄ act as effective lubricants leading to low friction coefficient. Similar lubrication behavior is reported in the literature (Huang et al. 2014, Kong et al. 2013).



(a)



(b)

Figure 3.53 Friction coefficient of Cr₃C₂-NiCr/Cenosphere/MoS₂/CaF₂ and Cr₃C₂-NiCr/Cenosphere/MoS₂/CaSO₄ coatings at sliding velocity of 1.5 and 2.5 m/s with (a) 20 and (b) 40 N normal loads at 200, 400 and 600 °C.

3.9.2.2 Wear loss

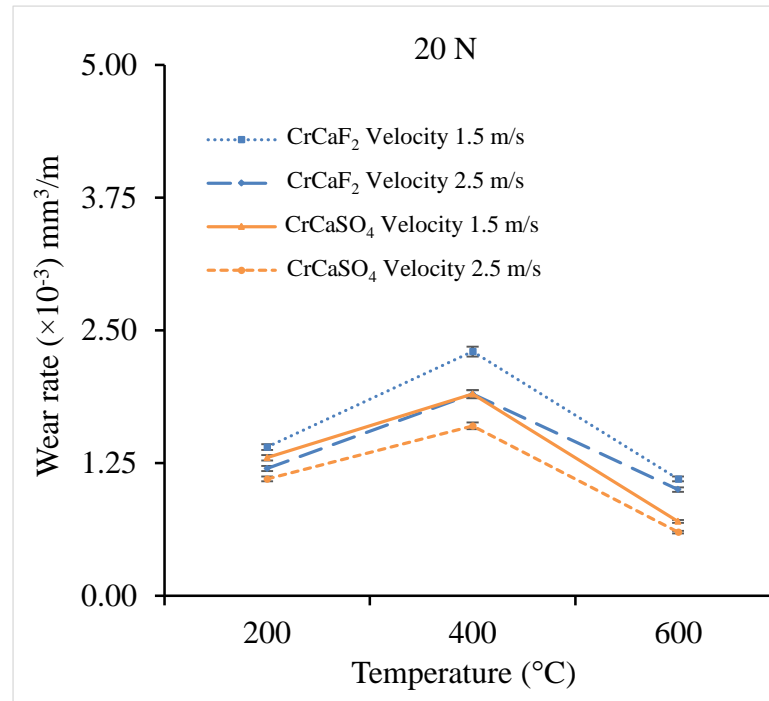
Figure 3.54a and Figure 3.54b demonstrates the wear rate of $\text{Cr}_3\text{C}_2\text{-NiCr/Cenosphere/MoS}_2/\text{CaF}_2$ and $\text{Cr}_3\text{C}_2\text{-NiCr/Cenosphere/MoS}_2/\text{CaSO}_4$ coatings at 200, 400 and 600 °C and sliding velocity of 1.5 and 2.5 m/s with 20 and 40 N normal loads. The wear rate of both the coatings increased with increasing normal load and decreased with an increase in the sliding velocity. With respect to temperature, both the coatings exhibited higher and lower wear rate at 400 and 600 °C respectively. Higher wear rate at 400 °C is due to loss of lubricating property of MoS_2 owing to its oxidation at a higher temperature and brittle form of solid lubricants (CaF_2 and CaSO_4). Lower wear rate at 200 and 600 °C is due to the formation of the lubrication layer on the surface. At 200 °C, MoS_2 acts as a lubricant as it is a low-temperature lubricant and forms the lubricating layer on the surface thereby reduces the wear rate. At 600 °C, solid lubricants CaF_2 and CaSO_4 get converted from brittle to ductile form and slides easily on the surface leading to lower wear rate.

3.9.2.3 XRD analysis

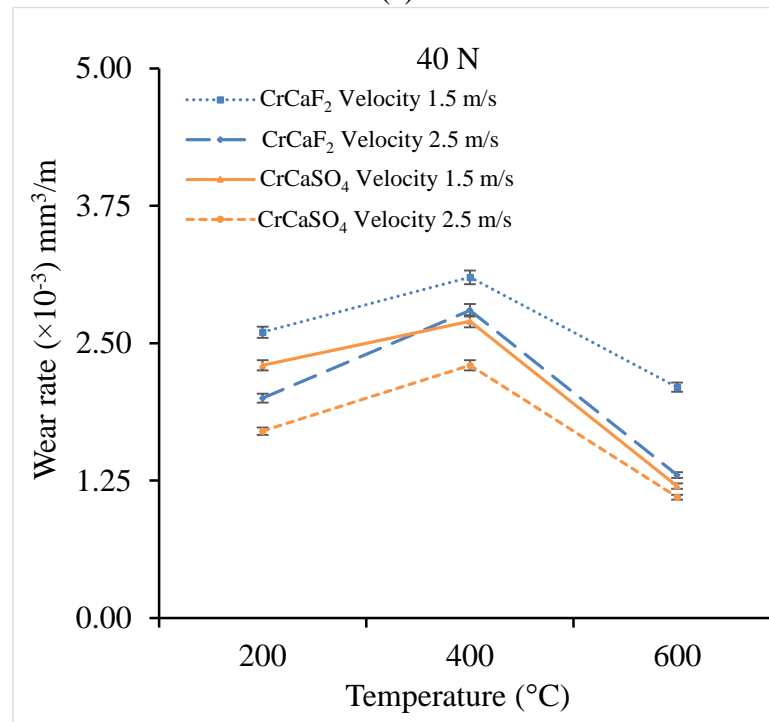
Figure 3.55 exhibit the XRD pattern of $\text{Cr}_3\text{C}_2\text{-NiCr/Cenosphere/MoS}_2/\text{CaF}_2$ coating worn surfaces tested at 200, 400 and 600 °C. From Figure 3.55 it is observed that distinct peaks of MoS_2 appear on the worn surfaces at 200 °C, whereas at 400 and 600 °C, some MoS_2 peaks are disappeared and intensity is reduced, which indicates that MoS_2 is active at 200 °C. At 600 °C, distinct CaF_2 peaks are observed along with new phases of CaMoO_4 and MoO_3 . At elevated temperature, molybdenum reacts with calcium and oxygen leads to the formation of molybdates and molybdenum oxide which are responsible for low coefficient of friction and lower wear rate. (Chen et al. 2013, Kong et al. 2013, Li et al. 2017).

XRD pattern of $\text{Cr}_3\text{C}_2\text{-NiCr/Cenosphere/MoS}_2/\text{CaSO}_4$ coating worn surfaces after 200, 400 and 600 °C wear tests is presented in Figure 3.56. At 200 °C, distinct peaks of MoS_2 are observed reveal that MoS_2 is formed on the surface during wear test at 200 °C temperature. At 400 °C, it is noticed some peaks of MoS_2 are disappeared suggesting that MoS_2 does not act as a lubricant at such intermediate temperature.

At 600 °C, distinct peaks of CaSO_4 are observed along with new phases of CaMoO_4 and MoO_3 as a result of oxidation.



(a)



(b)

Figure 3.54 Wear rate of $\text{Cr}_3\text{C}_2\text{-NiCr/Cenosphere/MoS}_2/\text{CaF}_2$ and $\text{Cr}_3\text{C}_2\text{-NiCr/Cenosphere/MoS}_2/\text{CaSO}_4$ coatings at sliding velocity of 1.5 and 2.5 m/s with (a) 20 and (b) 40 N normal loads at 200, 400 and 600 °C.

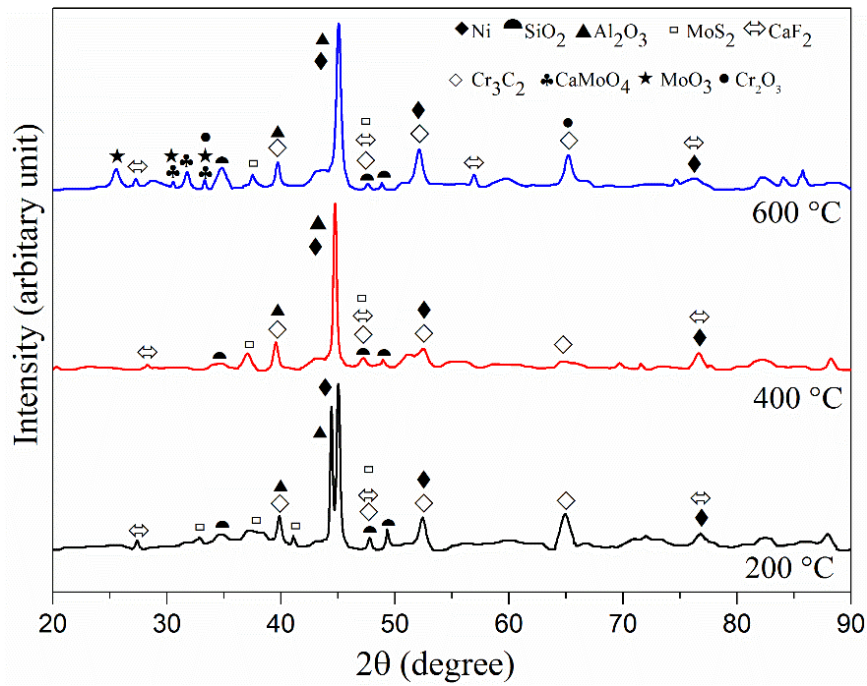


Figure 3.55 XRD pattern of worn out Cr_3C_2 -NiCr/Cenosphere/ MoS_2 / CaF_2 coating at 200, 400 and 600 °C.

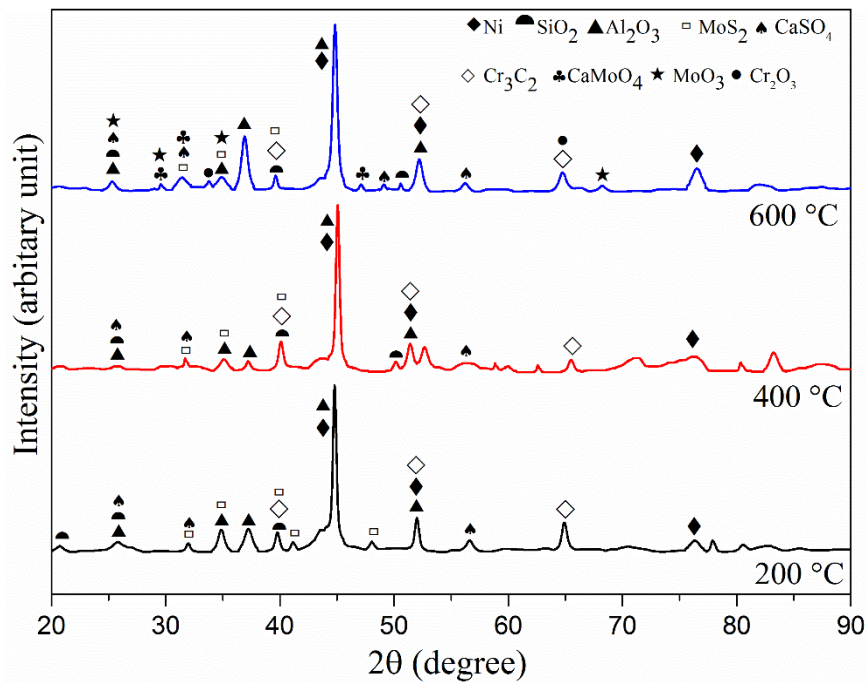


Figure 3.56 XRD pattern of worn out Cr_3C_2 -NiCr/Cenosphere/ MoS_2 / CaSO_4 coating at 200, 400 and 600 °C.

3.9.2.4 SEM/EDS analysis

Figure 3.57 and Figure 3.58 demonstrates the worn surface SEM micrographs of the $\text{Cr}_3\text{C}_2\text{-NiCr/Cenosphere/MoS}_2/\text{CaF}_2$ and $\text{Cr}_3\text{C}_2\text{-NiCr/Cenosphere/MoS}_2/\text{CaSO}_4$ coatings respectively at 1.5 m/s sliding velocity with 40 N normal load at 200, 400 and 600 °C. It can be observed from these micrographs that the worn surfaces of both the coatings characterized by a groove, delamination and flaking pit at all the test temperatures (Figure 3.57 and Figure 3.58) indicate ploughing and delamination. From Figure 3.57b and Figure 3.58b, it is noticed that at 400 °C worn surfaces are not smooth and the coating is detached by severe delamination. At 600 °C (Figure 3.57c and Figure 3.58c) worn surfaces are smooth with minimum delamination indicating lower wear loss. Figure 3.57d and Figure 3.58d show the worn surfaces of coatings at 200 °C with opened unmelted/semi-melted cenosphere. These hollow spheres accumulate the wear debris, avoiding three body abrasion leading to lower wear loss.

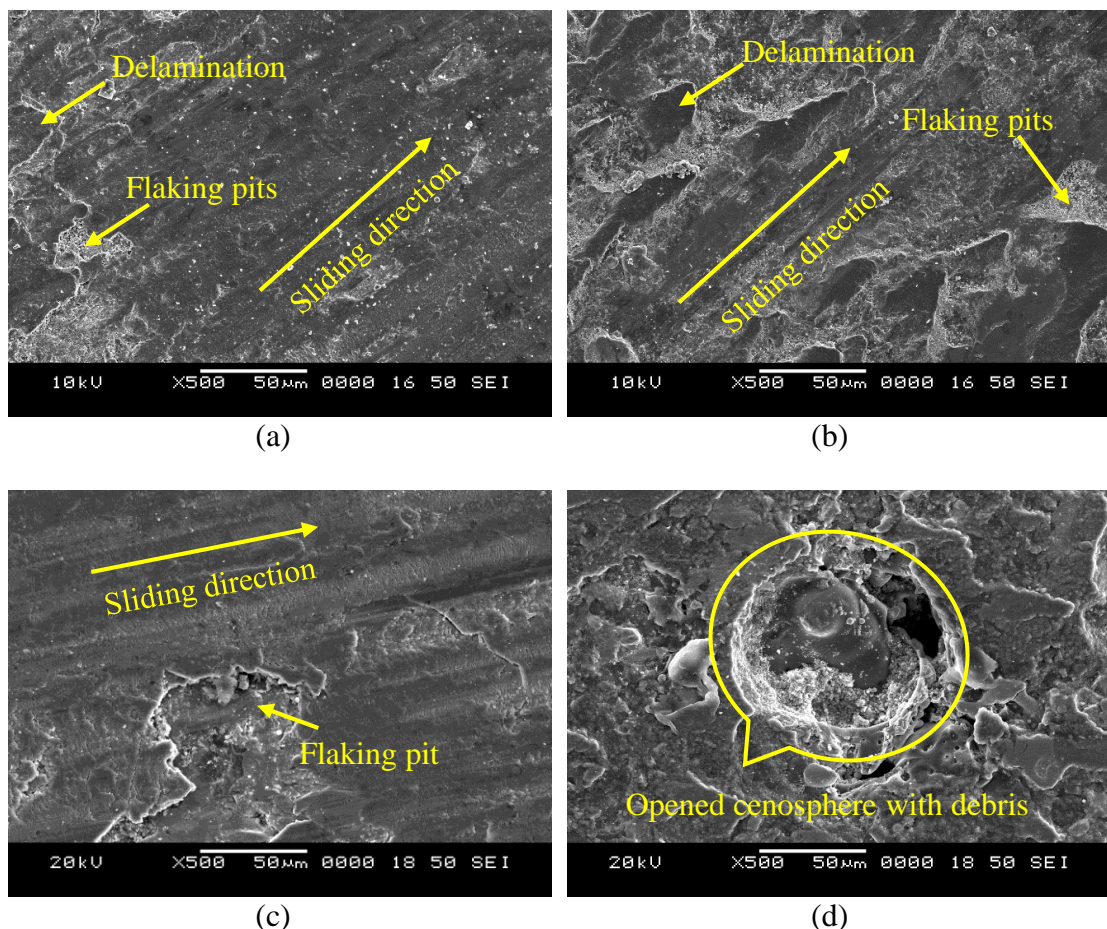


Figure 3.57 Worn surface SEM micrographs of $\text{Cr}_3\text{C}_2\text{-NiCr/Cenosphere/MoS}_2/\text{CaF}_2$ coating at (a) 200 (b) 400 (c) 600 °C and (d) opened cenosphere containing debris during wear test.

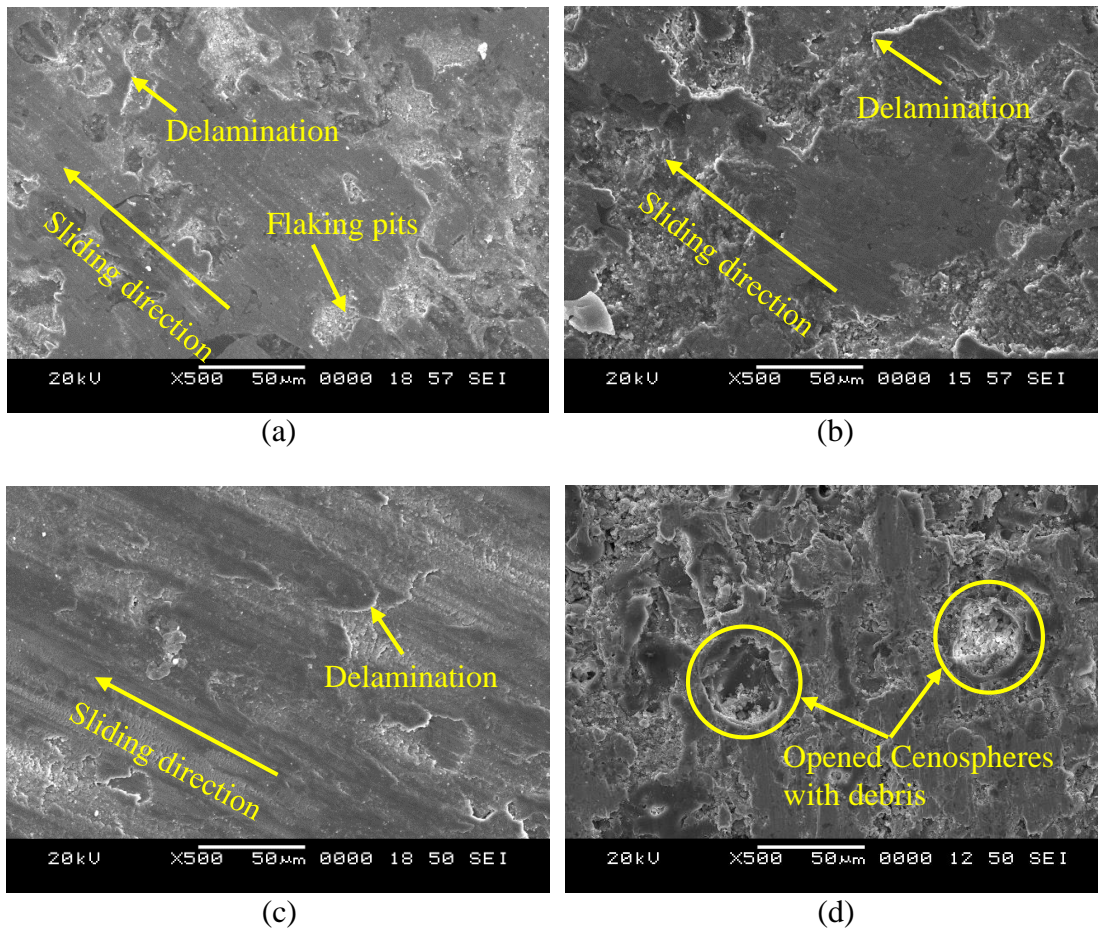


Figure 3.58 Worn surface SEM micrographs of $\text{Cr}_3\text{C}_2\text{-NiCr/Cenosphere/MoS}_2\text{/CaSO}_4$ coating at (a) 200 (b) 400 (c) 600 °C and (d) opened cenospheres containing debris during wear test.

Post wear test photograph of $\text{Cr}_3\text{C}_2\text{-NiCr/Cenosphere/MoS}_2\text{/CaF}_2$ coating wear track on Al_2O_3 disc at 200 °C and wear debris SEM micrographs of $\text{Cr}_3\text{C}_2\text{-NiCr/Cenosphere/MoS}_2\text{/CaF}_2$ coating collected at 200, 400 and 600 °C after wear test is displayed in Figure 3.59. Wear track of distinct gray color is established on the disc indicating the lubricating layer between the coating surface and disc as shown in Figure 3.59a. Figure 3.59b-d exhibits lamella-like wear debris as obtained after wear test at different temperatures. Wear debris seems to be much larger in size at 400 °C (Figure 3.59c) as compared to 200 and 600 °C demonstrating severe wear scenario at an intermediate temperature. At 600 °C, the size of the wear debris appears to be smaller owing to the smearing effect of lubricants at a higher temperature. The elemental

composition of the wear debris of $\text{Cr}_3\text{C}_2\text{-NiCr/Cenosphere/MoS}_2\text{/CaF}_2$ coating analyzed at 200, 400 and 600 °C by EDS and is presented in Table 3.5. Major elements found in wear debris are Ni, Cr, C, and Al. At 400 °C the wear debris consists of higher amounts of calcium, fluoride, oxygen and a smaller quantity of sulfur. These observations indicate oxidation of MoS_2 and CaF_2 removal in higher quantities.

At 600 °C, the wear debris contains a higher percentage of oxygen and calcium indicating the formation of CaMoO_4 due to the chemical reaction between MoO_3 and CaF_2 (Allam 1991). XRD analysis (Figure 3.55) of worn out samples at 600 °C also confirms the existence of CaMoO_4 . At higher temperature, the presence of CaMoO_4 along with CaF_2 are responsible for low friction and wear rates.

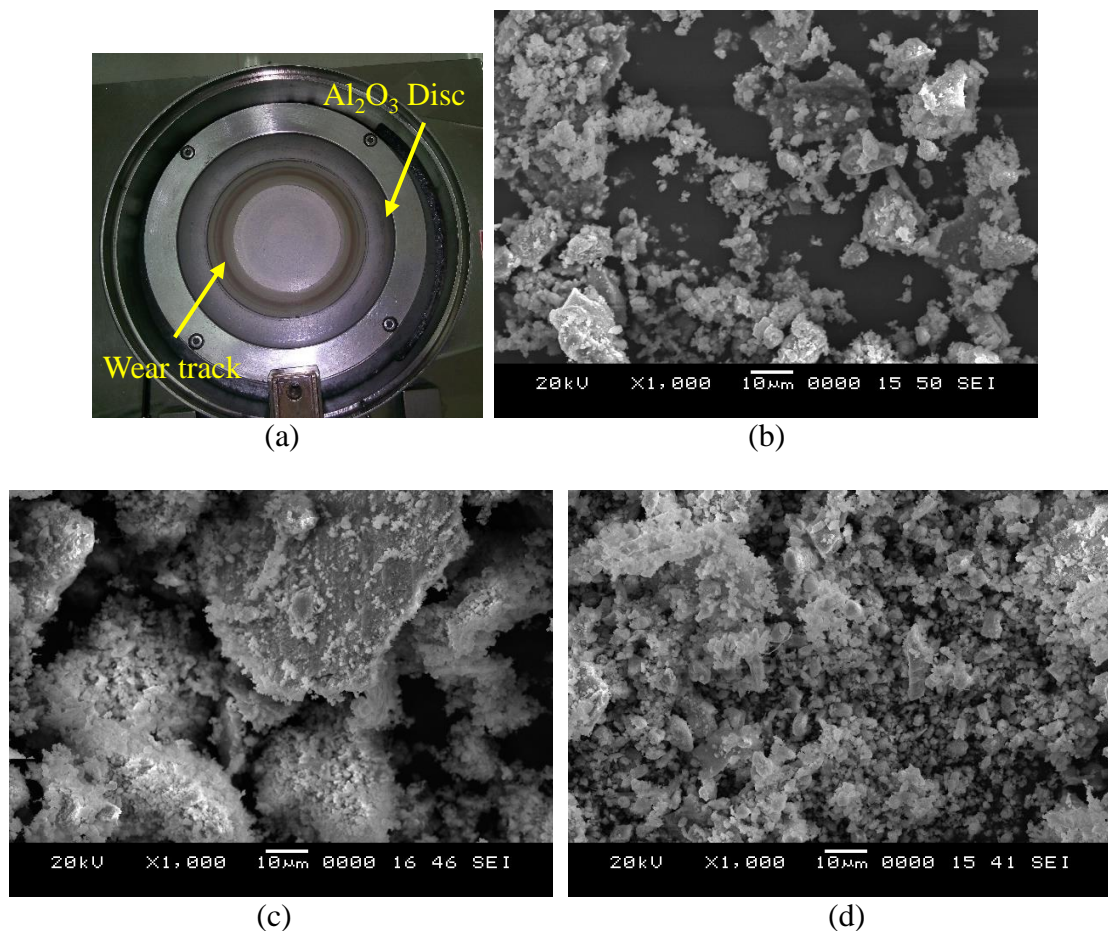


Figure 3.59 Post wear test photograph of (a) wear track on Al_2O_3 disc and wear debris SEM micrographs of $\text{Cr}_3\text{C}_2\text{-NiCr/Cenosphere/MoS}_2\text{/CaF}_2$ coating at (b) 200 (c) 400 and (d) 600 °C.

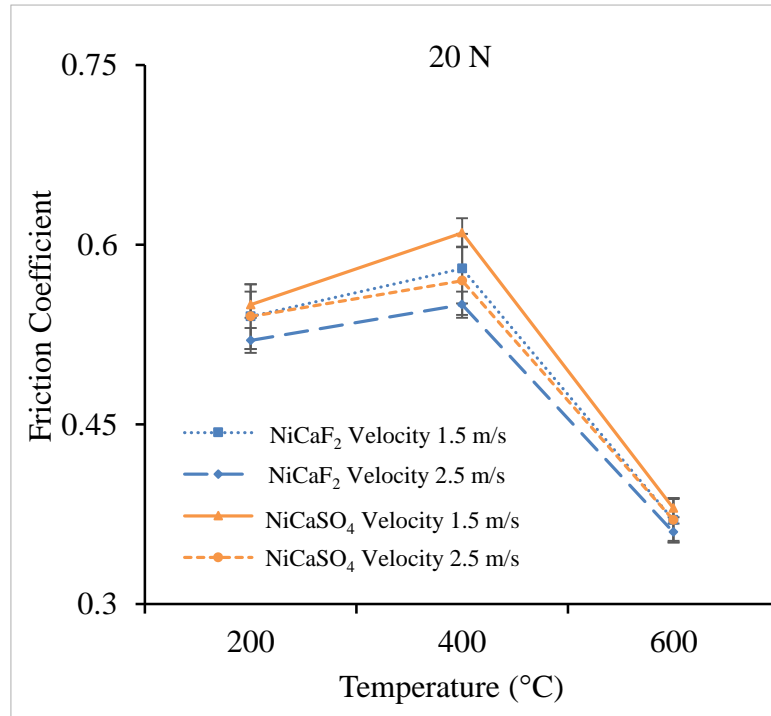
Table 3.5 EDS analysis of wear debris of Cr₃C₂-NiCr/Cenosphere/MoS₂/CaF₂ coating at 200, 400 and 600 °C.

Temperature (°C)	Elemental Composition (wt. %)									
	C	O	Al	Si	Ni	Cr	Mo	S	Ca	F
200	8.32	23.99	6.96	4.06	17.32	23.38	1.92	3.42	2.74	4.81
400	6.91	29.45	6.79	3.78	16.34	20.94	2.93	1.10	3.61	5.90
600	6.19	34.68	6.58	4.59	15.29	18.20	1.70	0.71	7.60	2.41

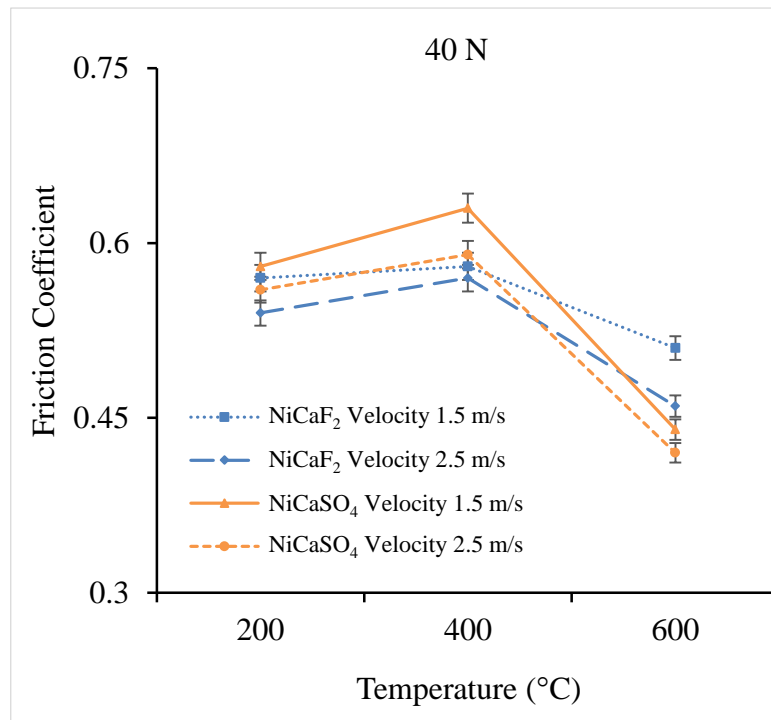
3.9.3 NiCrAlY/WC-Co/Cenosphere/MoS₂/CaF₂ and NiCrAlY/WC Co/Cenosphere/MoS₂/CaSO₄ coatings

3.9.3.1 Frictional Behaviour

Friction coefficient of NiCrAlY/WC-Co/Cenosphere/MoS₂/CaF₂ (designated as NiCaF₂) and NiCrAlY/WC-Co/Cenosphere/MoS₂/CaSO₄ (designated as NiCaSO₄) coatings at 200, 400 and 600 °C with sliding velocity of 1.5 and 2.5 m/s at 20 and 40 N normal loads is presented in Figure 3.60a and Figure 3.60b respectively. Friction coefficient is varied with temperature, sliding velocity, and normal load. It is decreased with an increase in the sliding velocity and increased with increasing load for both the coatings. In comparison with coatings, NiCrAlY/WC-Co/Cenosphere/MoS₂/CaF₂ registered lower friction coefficient as compared to NiCrAlY/WC-Co/Cenosphere/MoS₂/CaSO₄ coating. The lower friction coefficient of NiCrAlY/WC-Co/Cenosphere/MoS₂/CaF₂ coating is may be due to the lower hardness of the coating. At 20 N normal load and 1.5 m/s sliding velocity, friction coefficient of NiCrAlY/WC-Co/Cenosphere/MoS₂/CaF₂ and NiCrAlY/WC-Co/Cenosphere/MoS₂/CaSO₄ coatings are in the range of 0.37-0.58 and 0.38-0.61 respectively. At 40 N normal load and 1.5 m/s sliding velocity, friction coefficient of NiCrAlY/WC-Co/Cenosphere/MoS₂/CaF₂ and NiCrAlY/WC-Co/Cenosphere/MoS₂/CaSO₄ coatings are in the range of 0.51-0.58 and 0.44-0.63 respectively. Presence of solid lubricants in the coatings forms the lubricating layer during sliding test thereby reduces the friction coefficient of the coatings (Chen et al. 2013, Chen et al. 2014). At 400 °C, both the coatings demonstrated higher friction coefficient owing to inefficient lubrication of solid lubricants.



(a)



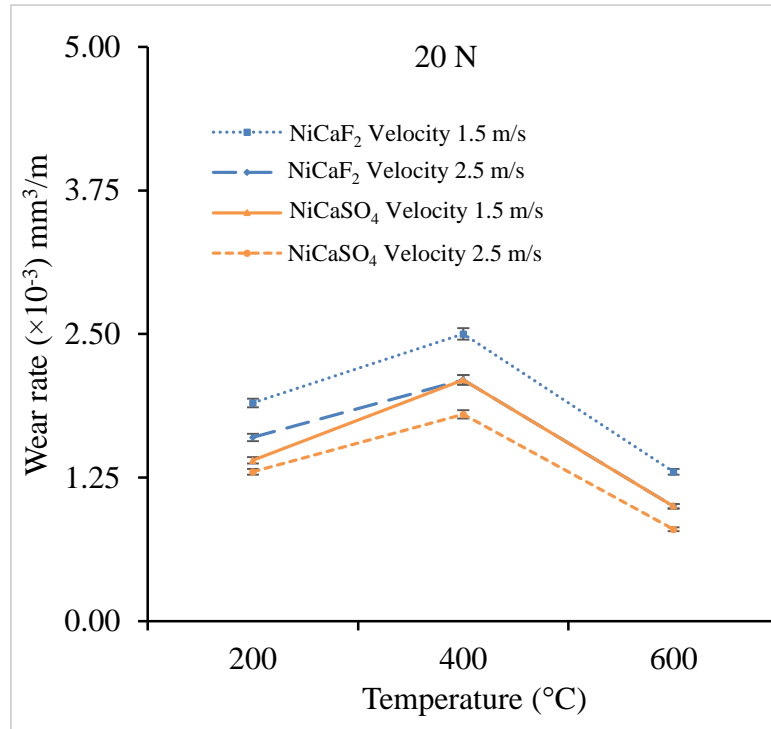
(b)

Figure 3.60 Friction coefficient of NiCrAlY/WC-Co/Cenosphere/MoS₂/CaF₂ and NiCrAlY/WC-Co/Cenosphere/MoS₂/CaSO₄ coatings at sliding velocity of 1.5 and 2.5 m/s with (a) 20 and (b) 40 N normal loads at 200, 400 and 600 °C.

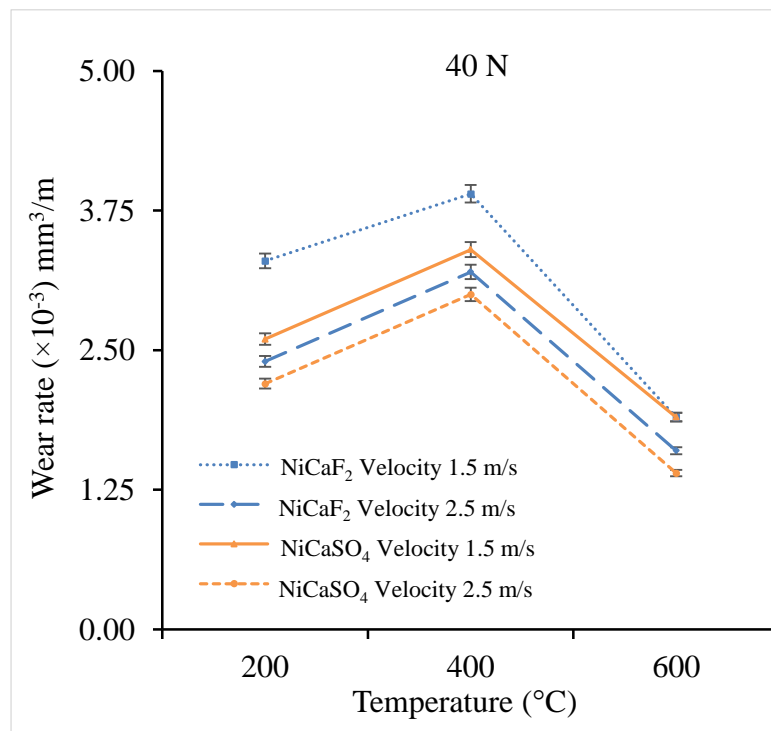
3.9.3.2 Wear loss

Figure 3.61a and Figure 3.61b exhibits the wear rates of NiCrAlY/WC-Co/Cenosphere/MoS₂/CaF₂ and NiCrAlY/WC-Co/Cenosphere/MoS₂/CaSO₄ coatings at 200, 400 and 600 °C and sliding velocity of 1.5 and 2.5 m/s with 20 and 40 N normal loads respectively. From Figure 3.61a and Figure 3.61b, it is observed that the wear rate of both the coatings is increased with increasing normal load from 20 to 40 N and decreased with increase in the sliding velocity from 1.5 to 2.5 m/s. With respect to the temperature, coatings exhibited a lower wear rate at 600 °C and a higher wear rate at 400 °C. Lower wear rate at 600 °C is due to the lubricating property of CaF₂ and CaSO₄. At elevated temperature CaF₂ and CaSO₄ get converted from brittle to ductile behavior shearing easily on the contacting surface. Higher wear rate at 400 °C is due to the inefficient lubrication of the solid lubricants. MoS₂ provides effective lubrication up to 300 °C and high-temperature solid lubricants CaF₂ and CaSO₄ are brittle in nature at 400 °C not providing any lubrication assistance.

Wear rate of NiCrAlY/WC-Co/Cenosphere/MoS₂/CaF₂ and NiCrAlY/WC-Co/Cenosphere/MoS₂/CaSO₄ coatings is in the range of $1.3-2.5 \times 10^{-3}$ and $1.0-2.1 \times 10^{-3}$ mm³/m at 20 N normal load and 1.5 m/s sliding velocity respectively. At 40 N normal load and 1.5 m/s sliding velocity, wear rate of NiCrAlY/WC-Co/Cenosphere/MoS₂/CaF₂ and NiCrAlY/WC-Co/Cenosphere/MoS₂/CaSO₄ coatings are in the range of $1.9-3.9 \times 10^{-3}$ and $1.9-3.4 \times 10^{-3}$ mm³/m respectively. Lower wear rate of the coatings is attributed to high hardness of reinforced WC-Co, the low shear strength of the solid lubricants incorporated in the coatings and presence of unmelted/semi-melted cenospheres in the coating, which open up during wear test.



(a)



(b)

Figure 3.61 Wear rate of NiCrAlY/WC-Co/Cenosphere/MoS₂/CaF₂ and NiCrAlY/WC-Co/Cenosphere/MoS₂/CaSO₄ coatings at sliding velocity of 1.5 and 2.5 m/s with (a) 20 and (b) 40 N normal loads at 200, 400 and 600 °C.

3.9.3.3 XRD analysis

Figure 3.62 displays the XRD patterns of NiCrAlY/WC-Co/Cenosphere/MoS₂/CaF₂ coating worn surfaces after 200, 400 and 600 °C wear tests. From Figure 3.62 it is observed that peaks of MoS₂ appear on worn surfaces at 200 °C. On the contrary at 400 and 600 °C test temperatures, the intensity of peaks are reduced indicating MoS₂ is active at 200 °C. Smaller peaks of CaF₂ are noticed at 400 °C. Further, these peaks become strong at 600 °C implying lubrication at higher temperatures by CaF₂. New phases of CaMoO₄ and MoO₃ are observed at 600 °C suggesting molybdenum's reaction with calcium and oxygen forming molybdates and molybdenum oxide responsible for low coefficient of friction and low wear rate at higher temperatures.

XRD pattern of worn surfaces of NiCrAlY/WC-Co/Cenosphere/MoS₂/CaSO₄ coating after 200, 400 and 600 °C wear tests are shown in Figure 3.63. At 200 °C, CaSO₄ and distinct peaks of MoS₂ are observed indicating the formation of MoS₂ on the surface during wear test. At 400 °C, it is noticed that the intensity of CaSO₄ peak is increased and some peaks of MoS₂ are disappeared which imply CaSO₄ dominance at 400 °C. At 600 °C distinct peaks of CaMoO₄ and MoO₃ are observed as a result of oxidation.

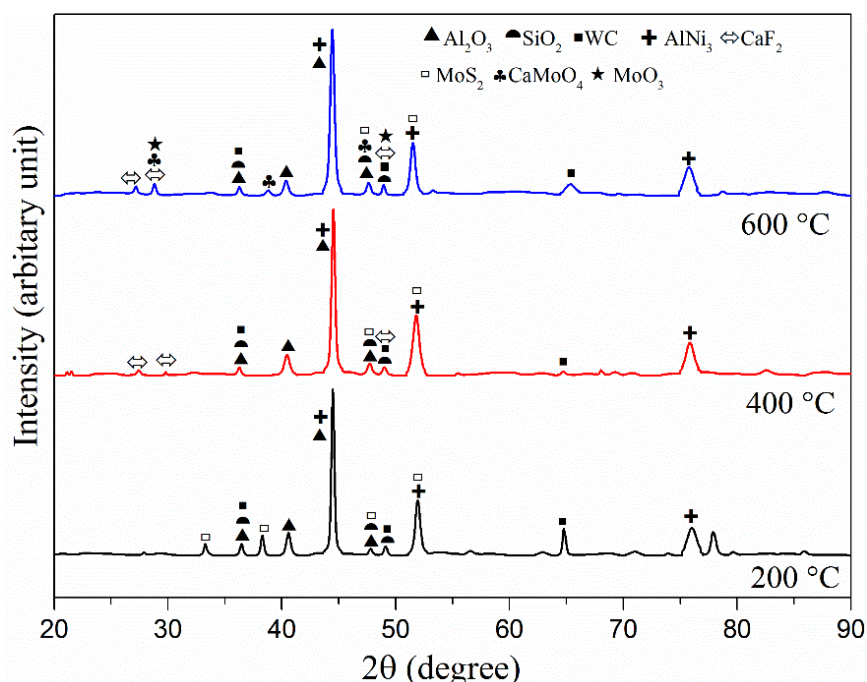


Figure 3.62 XRD pattern of worn out NiCrAlY/WC-Co/Cenosphere/MoS₂/CaF₂ coating at 200, 400 and 600 °C.

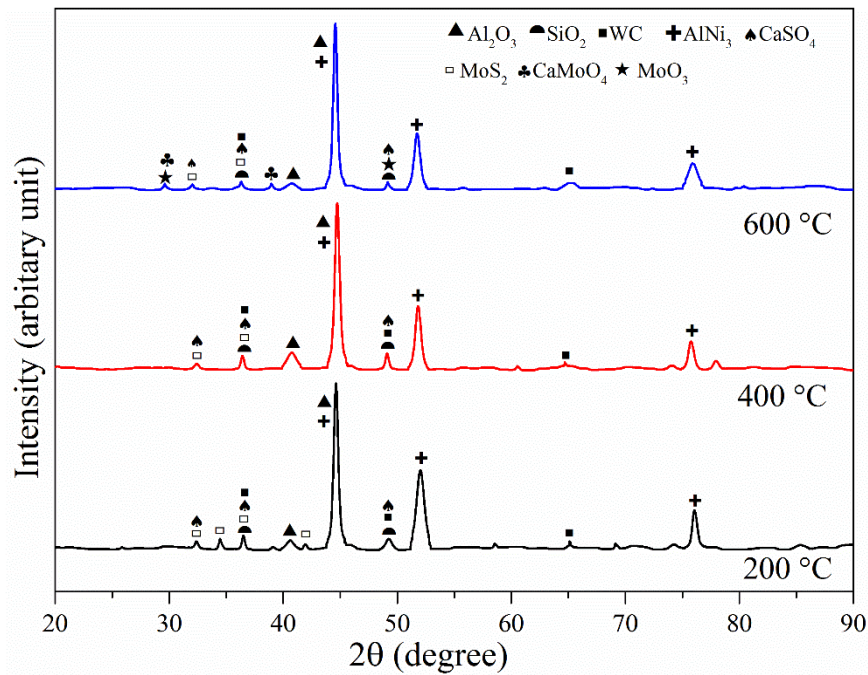


Figure 3.63 XRD pattern of worn out NiCrAlY/WC-Co/Cenosphere/ MoS_2 / CaSO_4 coating at 200, 400 and 600 °C.

3.9.3.4 SEM/EDS analysis

Worn surface SEM micrograph of NiCrAlY/WC-Co/Cenosphere/ MoS_2 / CaF_2 and NiCrAlY/WC-Co/Cenosphere/ MoS_2 / CaSO_4 coatings at 1.5 m/s sliding velocity with 40 N normal load at 200, 400 and 600 °C temperatures are showed in Figure 3.64 and Figure 3.65 respectively. At all the test temperatures, worn surface of both the coatings consists of grooves, flaking pits (Figure 3.64a and Figure 3.65a) demonstrating wear loss by ploughing and delamination. From Figure 3.64b and Figure 3.65b, it is observed that at 400 °C worn surfaces are not smooth and the coating is detached by maximum delamination suggesting severe wear. Lower wear is observed at 600 °C (Figure 3.64c and Figure 3.65c) characterized by a smoother worn surface with minimum delamination. Figure 3.64d and Figure 3.65d represent the worn surfaces of coatings at 200 °C with opened unmelted/semi-melted cenospheres. These hollow spheres accumulate the wear debris avoiding three body abrasion leading to lower wear loss subsequently.

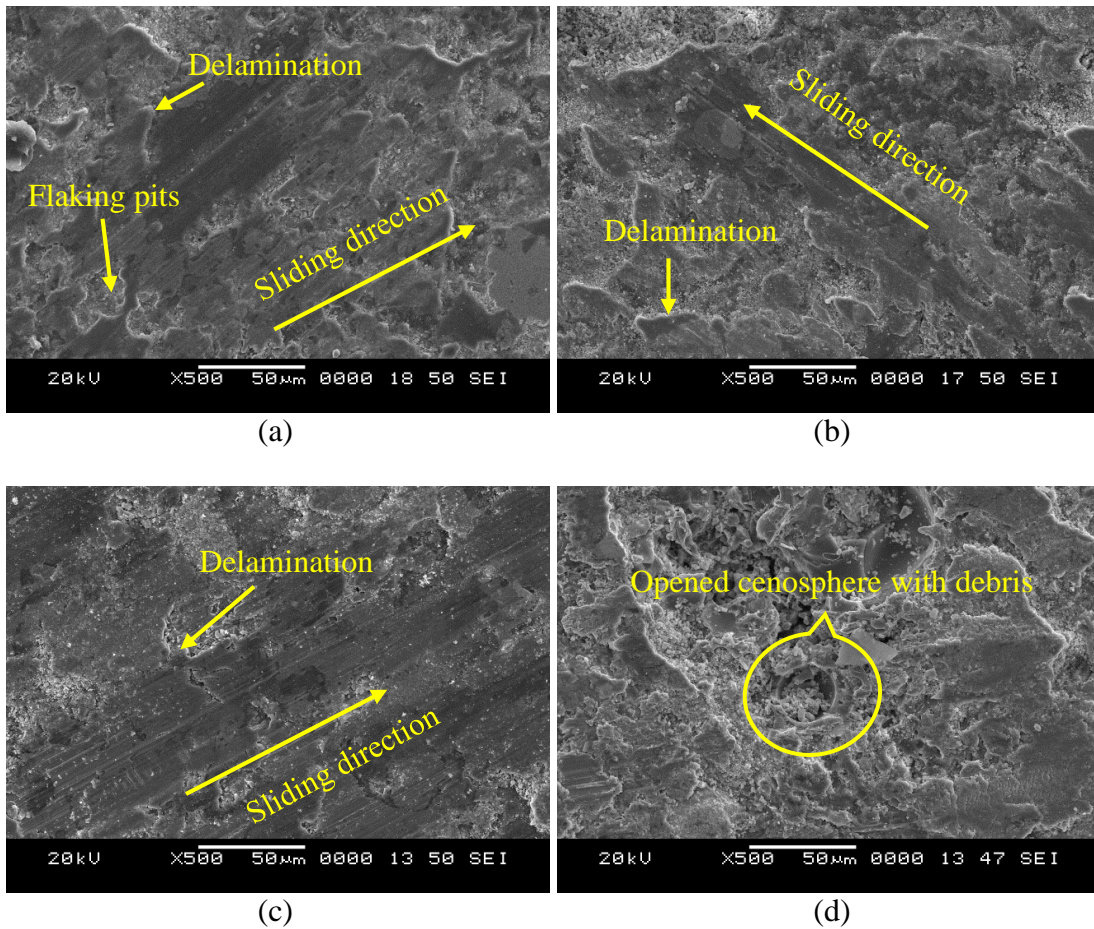


Figure 3.64 Worn surface SEM micrographs of NiCrAlY/WC-Co/Cenosphere/MoS₂/CaF₂ coating at (a) 200 (b) 400 (c) 600 °C and (d) opened cenosphere containing debris during wear test.

Figure 3.66 depicts post wear test photograph of NiCrAlY/WC-Co/Cenosphere/MoS₂/CaF₂ coating wear track on Al₂O₃ disc at 200 °C and wear debris SEM micrographs of NiCrAlY/WC-Co/Cenosphere/MoS₂/CaF₂ coating at 1.5 m/s sliding velocity, 40 N load and 200, 400 and 600 °C. From Figure 3.66a, it is observed that the gray color wear track is formed on the disc suggesting a lubricating layer between the coating surface and disc. Lamella like wear debris is observed post wear test as seen in Figure 3.66b-d. At 400 °C, Wear debris appears to be much larger in size (Figure 3.66c) as compared to 200 and 600 °C indicating extreme wear condition at an intermediate temperature.

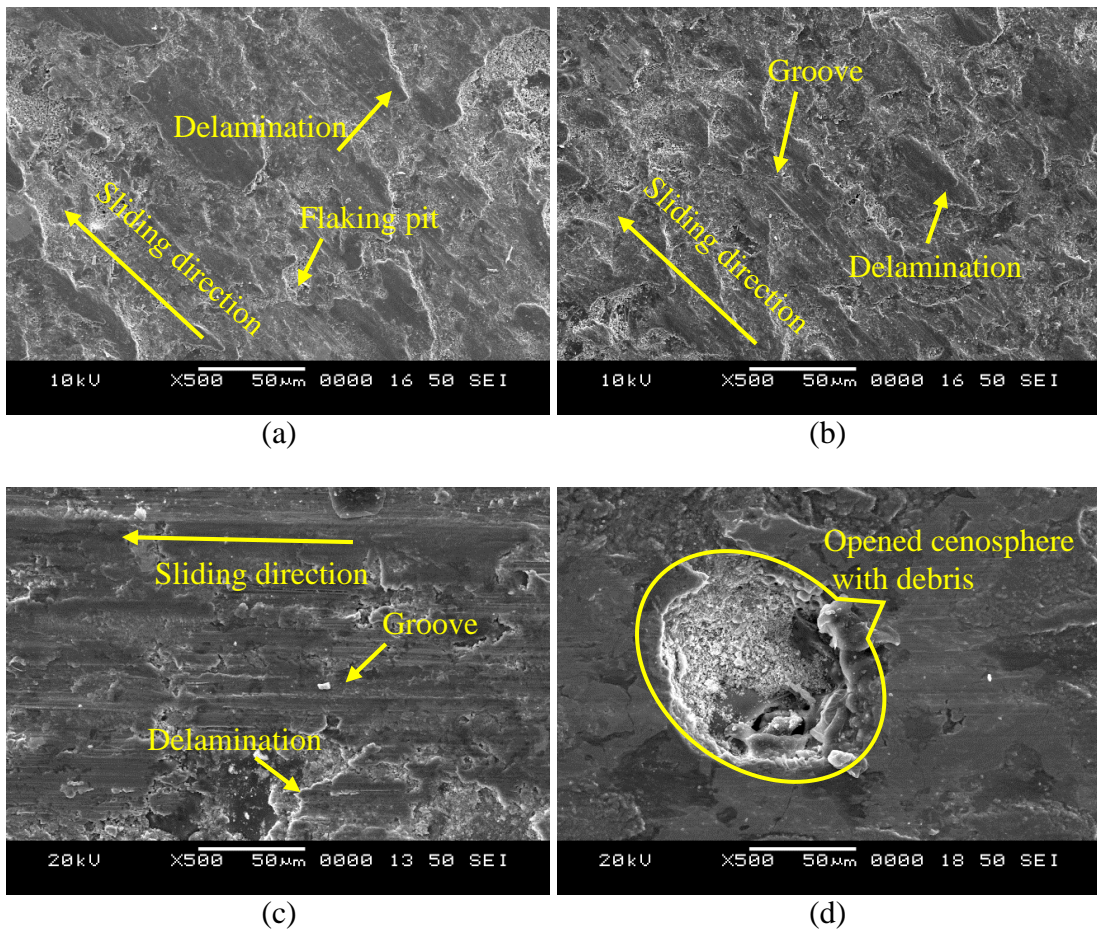


Figure 3.65 Worn surface SEM micrographs of NiCrAlY/WC-Co/Cenosphere/MoS₂/CaSO₄ coating at (a) 200 (b) 400 (c) 600 °C and (d) opened cenosphere containing debris during wear test.

The elemental composition of the wear debris analyzed by EDS is presented in Table 3.6. The elements found in wear debris are Ni, W, C, and Al which are removed from coatings. A large amount of Calcium, Fluoride, and Oxygen and a small amount of sulfur in wear debris at 400 °C implies that MoS₂ has undergone oxidation and a larger amount of CaF₂ is removed. At 600 °C, the wear debris contains higher oxygen and calcium percentage indicating the formation of CaMoO₄ due to the chemical reaction between MoO₃ and CaF₂. CaMoO₄ along with CaF₂ is responsible for low friction and low wear rate of coating at a higher temperature.

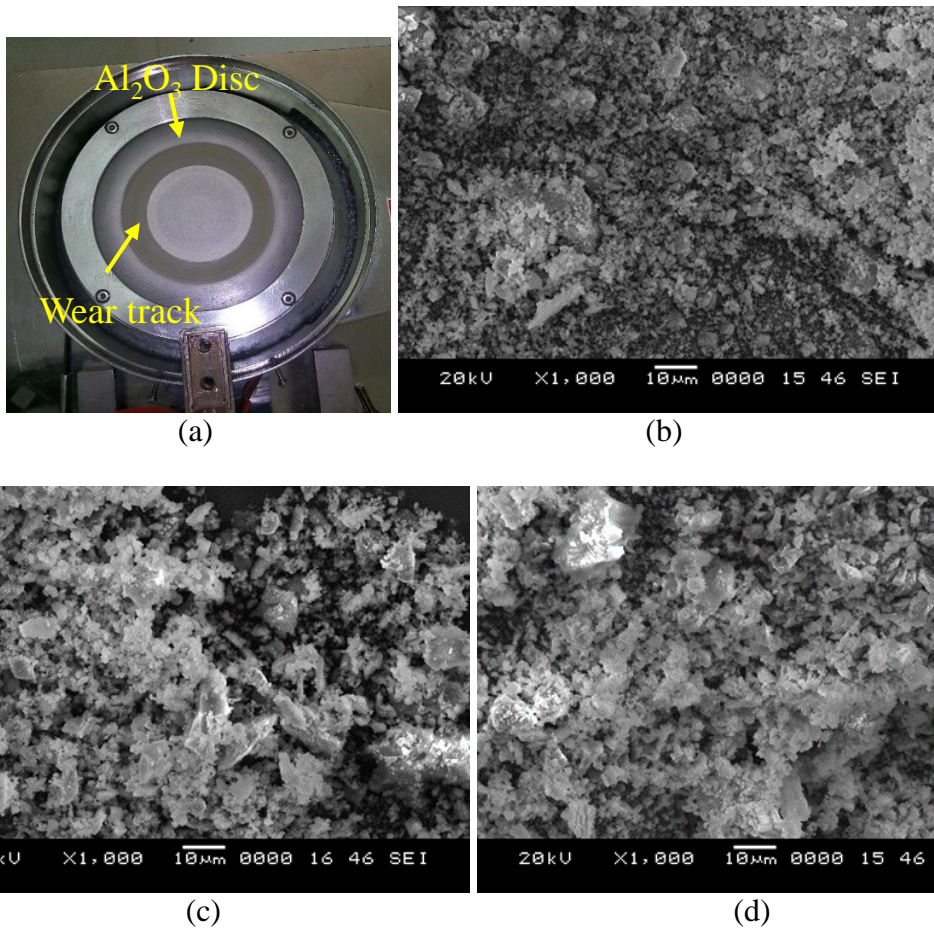


Figure 3.66 Post wear test photograph of (a) wear track on Al_2O_3 disc and wear debris SEM micrographs of NiCrAlY/WC-Co/Cenosphere/ MoS_2 / CaF_2 coating at (b) 200 (c) 400 and (d) 600 °C.

Table 3.6 EDS analysis of NiCrAlY/WC-Co/Cenosphere/ MoS_2 / CaF_2 coating wear debris at 200, 400 and 600 °C.

Temperature (°C)	Elemental Composition (wt. %)										
	C	O	Al	Si	Ni	Cr	W	Mo	S	Ca	F
200	7.32	24.40	10.06	3.19	18.02	11.99	9.58	2.10	3.56	2.81	4.94
400	8.80	29.25	9.21	3.83	16.43	6.91	9.12	2.81	1.04	3.86	6.09
600	6.72	34.07	8.72	3.33	16.44	7.88	7.74	1.92	0.84	7.76	2.54

3.9.4 Wear mechanism

Figure 3.67 demonstrates the wear mechanism of $\text{Cr}_3\text{C}_2\text{-NiCr/Cenosphere/MoS}_2/\text{CaF}_2$ coating. Figure 3.67a shows beginning stage of friction where coating constituents cenospheres, MoS_2 and CaF_2 are distributed uniformly in the $\text{Cr}_3\text{C}_2\text{-NiCr}$ matrix. Once the coating comes in contact with the counter body, cenospheres, MoS_2 , and CaF_2 emerge on the coating surface. MoS_2 and CaF_2 being soft, get extruded and spread on the worn surface of the coating. Meanwhile, all the unmelted/semi-melted cenospheres in the coating which are in contact with disc open up as they are hollow and part of the debris generated as result of friction, gets accumulated in broken hollow microspheres (Figure 3.67b). This accumulated debris in the broken hollow spheres further acts as a lubricating agent. At 200 °C, MoS_2 being a low-temperature lubricant, smeared on the worn surface and forms a lubricating layer leading to better lubrication (Figure 3.67b). At 600 °C, MoS_2 gets oxidized rapidly prior to wear and forms MoO_3 . Meanwhile, Cr_2O_3 oxide particles are produced owing to oxidation of chromium and get deposited on the surface. As the wear begins, MoO_3 reacts with CaF_2 and forms CaMoO_4 . Further, at 600 °C CaF_2 gets converted from brittle to ductile providing smoothening effect augmenting lubrication effectively. These CaF_2 and CaMoO_4 get smeared on the worn surface under the applied loads and friction leading to the formation of CaF_2 and CaMoO_4 layer (Figure 3.67c). This formed layer on the top surface and protective Cr_2O_3 layer underneath providing excellent lubrication and wear resistance at elevated temperature.

3.9.5 Comparative discussion

Figure 3.68a and Figure 3.68b represents the friction coefficient and wear rate of MDN 321 steel and coatings at 40 N normal load with 1.5 m/s velocity at 200, 400 and 600 °C temperatures. All the developed coatings exhibited lower friction coefficient and wear rate as compared to MDN 321 steel substrate. The lower friction coefficient of coatings is attributed to the lubricating property of the solid lubricants incorporated in the coatings. Solid lubricants possess lower shear strength and easily gets sheared on the rubbing surfaces thereby reduces the friction coefficient. MoS_2 provides lubrication at 200 °C while at elevated temperatures, CaF_2 and CaSO_4 provide lubrication. Lower

wear rate of the coatings is due to the higher hardness of the coatings and presence of unmelted/semi-melted cenospheres in the coating.

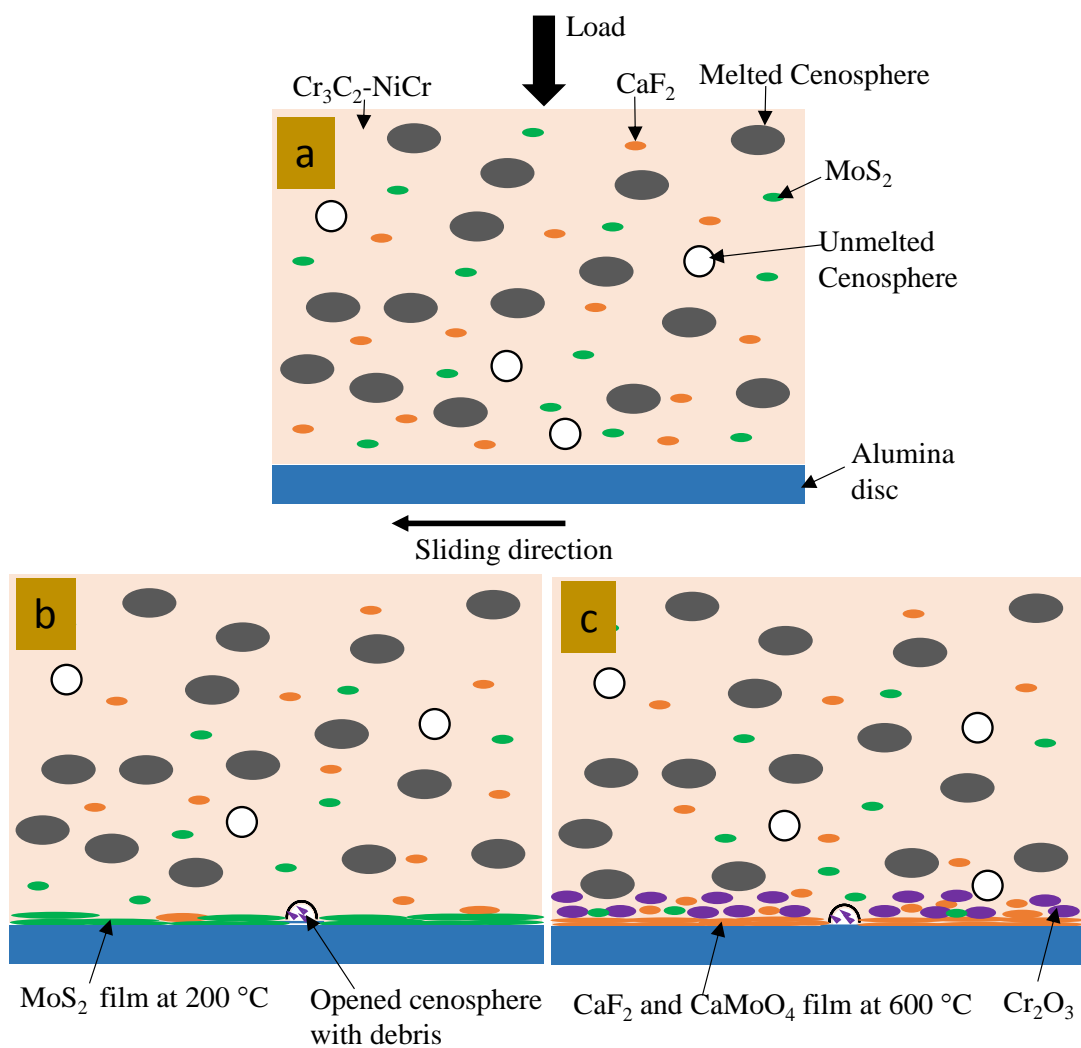


Figure 3.67 Schematic diagram of the wear mechanism of $\text{Cr}_3\text{C}_2\text{-NiCr/Cenosphere/MoS}_2/\text{CaF}_2$ coating at different temperatures (a) start of wear test (b) wear surface at $200\text{ }^\circ\text{C}$ (c) wear surface at $600\text{ }^\circ\text{C}$.

Relative wear resistance of the MDN 321 steel and coatings can be arranged in the following sequence:

$\text{Cr}_3\text{C}_2\text{-NiCr/Cenosphere/MoS}_2/\text{CaSO}_4 > \text{Cr}_3\text{C}_2\text{-NiCr/Cenosphere/MoS}_2/\text{CaF}_2 > \text{NiCrAlY/WC-Co/Cenosphere/MoS}_2/\text{CaSO}_4 > \text{NiCrAlY/WC-Co/Cenosphere/MoS}_2/\text{CaF}_2 > \text{MDN 321 steel substrate.}$

$\text{Cr}_3\text{C}_2\text{-NiCr/Cenosphere/MoS}_2/\text{CaSO}_4$ and $\text{Cr}_3\text{C}_2\text{-NiCr/Cenosphere/MoS}_2/\text{CaF}_2$ coatings registered higher wear resistance as compared to $\text{NiCrAlY/WC-Co/Cenosphere/MoS}_2/\text{CaSO}_4$ and $\text{NiCrAlY/WC-Co/Cenosphere/MoS}_2/\text{CaF}_2$ which might be attributed to the higher hardness of the $\text{Cr}_3\text{C}_2\text{-NiCr/Cenosphere/MoS}_2/\text{CaSO}_4$ and $\text{Cr}_3\text{C}_2\text{-NiCr/Cenosphere/MoS}_2/\text{CaF}_2$ coatings.

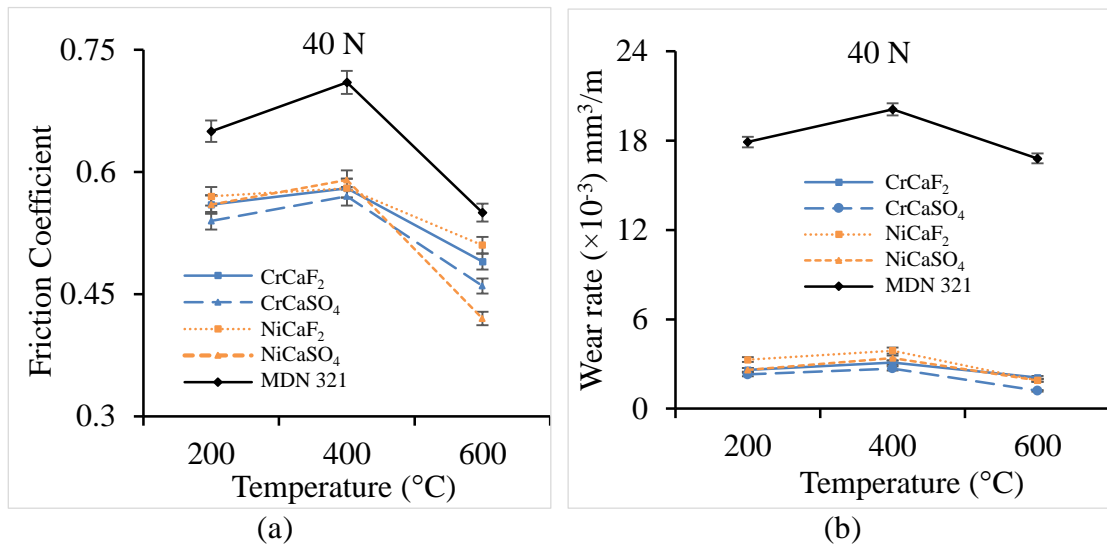


Figure 3.68 (a) friction coefficient and (b) wear rate of MDN 321 steel and coatings at 40 N normal load with 1.5 m/s velocity at 200, 400 and 600 °C temperatures.

4 CONCLUSIONS

In the present study composite coatings composed of metallic, carbides, fly ash cenospheres and solid lubricants are successfully developed using plasma spray technique on MDN 321 steel substrate. Use of cenospheres can reduce the cost of coatings. In addition, fly ash is an industrial waste and use of cenospheres in coatings can reduce the landfill burden addressing the environmental concern of fly ash disposal.

The main conclusions can be summarized as:

- The $\text{Cr}_3\text{C}_2\text{-NiCr/Cenosphere}$, $\text{NiCrAlY/WC-Co/Cenosphere}$, $\text{Cr}_3\text{C}_2\text{-NiCr/Cenosphere/MoS}_2\text{/CaF}_2$, $\text{Cr}_3\text{C}_2\text{-NiCr/Cenosphere/MoS}_2\text{/CaSO}_4$, $\text{NiCrAlY/WC-Co/Cenosphere/MoS}_2\text{/CaF}_2$ and $\text{NiCrAlY/WC-Co/Cenosphere/MoS}_2\text{/CaSO}_4$ coatings exhibited uniform thickness in the range of 350-400 μm having lesser than 5% porosity.
- All the coatings registered higher hardness as compared to MDN 321 steel due to the higher hardness of the coating constituents. $\text{Cr}_3\text{C}_2\text{-NiCr/Cenosphere}$ coating displayed higher hardness owing to the higher hardness of $\text{Cr}_3\text{C}_2\text{-NiCr}$. Coatings with solid lubricants showed lower hardness owing to the lower hardness of solid lubricants.
- All the coatings exhibited almost similar peaks in coated samples as compared to that of the blended powder, indicating a minor change in their phase composition after plasma spraying. $\text{NiCrAlY/WC-Co/Cenosphere}$ coating showed W_2C phase due to decarburization of WC during plasma spraying.
- $\text{Cr}_3\text{C}_2\text{-NiCr/Cenosphere/MoS}_2\text{/CaSO}_4$ coating registered higher adhesion strength of 18.10 ± 2.2 MPa as compared to other coatings. Fractured surface reveals the cohesive failure of the coatings which is due to lower impact force of low density cenospheres and solid lubricants during the spraying process.

Solid particle erosion studies

- $\text{Cr}_3\text{C}_2\text{-NiCr/Cenosphere}$ and $\text{NiCrAlY/WC-Co/Cenosphere}$ coatings showed higher erosion resistance as compared to MDN 321 steel. Erosion resistance of the $\text{Cr}_3\text{C}_2\text{-NiCr/Cenosphere}$ and $\text{NiCrAlY/WC-Co/Cenosphere}$ coatings are 87 and 85 % higher than the MDN 321 steel.

- Relative erosion resistance of the MDN 321 steel and coatings can be arranged in the following sequence:
NiCrAlY/WC-Co/Cenosphere coating > Cr₃C₂-NiCr/Cenosphere coating > MDN 321 steel
- Higher erosion resistance of the coatings is attributed to high hardness of the coatings, higher temperature stability of constituents and oxidation resistance.
- Higher erosion resistance of the NiCrAlY/WC-Co/Cenosphere coating is due to the higher percentage of NiCrAlY matrix which is deformed plastically owing to its ductility and hard WC-Co reinforcement resisting the matrix plough and thereby minimizing erosion loss.
- Both the coatings reported brittle mode of material removal where material is removed by brittle cracking and chipping.

Oxidation studies

- Cr₃C₂-NiCr/Cenosphere and NiCrAlY/WC-Co/Cenosphere coatings exhibited higher oxidation resistance as compared to MDN 321 steel. Protective thin oxide scale formed during oxidation imparted better oxidation resistance to the coatings.
- The oxide scale is found to be compact, smooth and no spalling or cracks have been observed during the oxidation cycles.
- Cr₃C₂-NiCr/Cenosphere and NiCrAlY/WC-Co/Cenosphere coatings exhibited considerable lower weight gain as compared to MDN 321 steel which is 10.58 and 13.00% less than MDN 321 steel respectively.
- Based on the thermogravimetric data, the relative oxidation resistance of the MDN 321 steel and coatings can be arranged in the following sequence:
NiCrAlY/WC-Co/Cenosphere coating > Cr₃C₂-NiCr/Cenosphere coating > MDN 321 steel.
- The better oxidation resistance of NiCrAlY/WC-Co/Cenosphere coating is attributed to the superior oxidation resistance property of NiCrAlY matrix as compared to Cr₃C₂-NiCr. Further, continuous and protective thin oxide scale consisting of oxides of Cr, Al and Ni and mixed spinel type oxides of CoWO₄ improved the oxidation resistance.

Wear studies

- All the coatings presented lower friction coefficient and wear rate as compared to MDN 321 steel substrate. The lower friction coefficient of coatings is attributed to the lubricating property of the solid lubricants incorporated in the coatings.
- Lower wear rate of the coatings is due to the higher hardness of the coatings, presence of unmelted/semi-melted cenospheres in the coating that opens up during wear test. These opened cenospheres accumulate the debris generated during the test and avoid the three body abrasion reducing wear rate.
- Friction coefficient and wear rate of the MDN 321 steel and coatings found to be increased with increase in the normal load and decreased with increase in the sliding velocity. With respect to temperature, MDN 321 steel and all the coatings registered higher and lower coefficient of friction and wear rate at 400 and 600 °C respectively.
- At 200 °C, MoS₂ provided the lubrication by easily getting sheared on the sliding surfaces while at 600 °C high temperature solid lubricants like CaF₂ and CaSO₄ along with CaMoO₄ (formed through tribo chemistry reaction) offered effective lubrication.
- Based on the wear rate data, the relative wear resistance of the coatings under dry sliding conditions are arranged in the following sequence:
(Cr₃C₂-NiCr/Cenosphere/MoS₂/CaSO₄) > (Cr₃C₂-NiCr/Cenosphere/MoS₂/CaF₂) > (NiCrAlY/WC-Co/Cenosphere/MoS₂/CaSO₄) > (NiCrAlY/WC-Co/Cenosphere/MoS₂/CaF₂).
- Higher wear resistance of Cr₃C₂-NiCr/Cenosphere/solid lubricant coatings is attributed to the higher hardness of Cr₃C₂-NiCr.

Present work successfully demonstrated the feasibility of fly ash cenospheres as a coating material for plasma spray coatings. Coatings showed better resistance to erosion, oxidation and wear at elevated temperature making them suitable for elevated temperature industrial applications. Incorporating fly ash cenospheres in the coatings reduced the cost of coatings to around 10%. Further, usage of such fly ash cenospheres reduces landfill burden and environmental linked disposal issues. As the cenospheres are readily available in powder form, they can eliminate the expensive powder manufacturing process and associated longer lead times.

SCOPE OF FUTURE WORK

Present work demonstrates the feasibility of fly ash cenospheres as a coating material for plasma spray technique. Though coatings exhibited better erosion, oxidation and wear resistance as compared to MDN 321 steel, the adhesion strength of the coatings is observed to be lower due low impact force of cenospheres while getting deposited as part of the coating process. Impact force can be increased by developing the coatings by employing high velocity oxy fuel coating technique. Further, cenosphere can be added to the different percentage in order to optimize the weight percentage of cenospheres in the coating.

REFERENCES

- Allam, IM. (1991). "Solid lubricants for applications at elevated temperatures." *Journal of materials science*, 26(15), 3977-3984.
- Arizmendi-Morquecho, A, Chávez-Valdez, A and Alvarez-Quintana, J. (2012). "High temperature thermal barrier coatings from recycled fly ash cenospheres." *Applied Thermal Engineering*, 48, 117-121.
- ASTM B276-05, *Standard Test Method for Apparent Porosity in Cemented Carbides*, ASTM International, PA, USA.
- ASTM C135-96, *Standard Test Method for True Specific Gravity of Refractory Materials by Water Immersion*, ASTM International, PA, USA.
- ASTM C633-13, *Standard Test Method for Adhesion or Cohesion Strength of Thermal Spray Coatings*, ASTM International, PA, USA.
- ASTM G76-13, *Standard Test Method for Conducting Erosion Tests by Solid Particle Impingement Using Gas Jets*, ASTM International, PA, USA.
- ASTM G99-05, *Standard Test Method for Wear Testing with a Pin-on-Disk Apparatus*, ASTM International, PA, USA.
- Baker, CC, Chromik, RR, Wahl, KJ, Hu, JJ and Voevodin, AA. (2007). "Preparation of chameleon coatings for space and ambient environments." *Thin Solid Films*, 515(17), 6737-6743.
- Behera, Ajit and Mishra, SC. (2012). "Application of Fly-ash Composite in Plasma Surface Engineering". *National Seminar on Waste to Wealth*, Bhubaneswar.
- Berger, Lutz-Michael. (2015). "Application of hardmetals as thermal spray coatings." *International Journal of Refractory Metals and Hard Materials*, 49, 350-364.
- Bharath Kumar, B. R., Doddamani, Mrityunjay, Zeltmann, Steven E., Gupta, Nikhil, Ramesh, M. R. and Ramakrishna, Seeram. (2016 A). "Processing of cenosphere/HDPE

syntactic foams using an industrial scale polymer injection molding machine." *Materials & Design*, 92, 414-423.

Bharath Kumar, B. R., Doddamani, Mrityunjay, Zeltmann, Steven E., Gupta, Nikhil, Uzma, Gurupadu, S. and Sailaja, R. R. N. (2016 B). "Effect of particle surface treatment and blending method on flexural properties of injection-molded cenosphere/HDPE syntactic foams." *Journal of materials science*, 51(8), 3793-3805.

Bharath Kumar, B. R., Zeltmann, Steven Eric, Doddamani, Mrityunjay, Gupta, Nikhil, Uzma, Gurupadu, S. and Sailaja, R. R. N. (2016 C). "Effect of cenosphere surface treatment and blending method on the tensile properties of thermoplastic matrix syntactic foams." *Journal of Applied Polymer Science*, 133(35).

Bi, Qinling, Zhu, Shengyu and Liu, Weimin. (2013). "High temperature self-lubricating materials." *InTech*.

Bin, CAI, TAN, Ye-fa, Long, HE, Hua, TAN and WANG, Xiao-long. (2013). "Tribological behavior and mechanisms of graphite/CaF₂/TiC/Ni-base alloy composite coatings." *Transactions of Nonferrous Metals Society of China*, 23(2), 392-399.

Bonache, V, Salvador, MD, García, JC, Sánchez, E and Bannier, E. (2011). "Influence of plasma intensity on wear and erosion resistance of conventional and nanometric WC-Co coatings deposited by APS." *Journal of thermal spray technology*, 20(3), 549-559.

Brudnyi, AI and Karmadonov, AF. (1975). "Structure of molybdenum disulphide lubricant film." *Wear*, 33(2), 243-249.

Bunshah, Rointan Framroze. (1994). "Handbook of deposition technologies for films and coatings: science, technology, and applications." *William Andrew*.

CEA. (2017). "Report on fly ash generation at coal/lignite based thermal power stations and its utilization in the country for the year 2016-17." New Delhi: Central Electricity Authority, India.

Chen, Jianmin, Hou, Guoliang, Chen, Jie, An, Yulong, Zhou, Huidi, Zhao, Xiaoqin and Yang, Jie. (2012). "Composition versus friction and wear behavior of plasma sprayed WC-(W, Cr) 2 C-Ni/Ag/BaF₂-CaF₂ self-lubricating composite coatings for use up to 600° C." *Applied Surface Science*, 261, 584-592.

Chen, Jie, An, Yulong, Yang, Jie, Zhao, Xiaoqin, Yan, Fengyuan, Zhou, Huidi and Chen, Jianmin. (2013). "Tribological properties of adaptive NiCrAlY-Ag-Mo coatings prepared by atmospheric plasma spraying." *Surface and Coatings Technology*, 235, 521-528.

Chen, Jie, Zhao, Xiaoqin, Zhou, Huidi, Chen, Jianmin, An, Yulong and Yan, Fengyuan. (2014). "Microstructure and tribological property of HVOF-sprayed adaptive NiMoAl-Cr₃ C₂-Ag composite coating from 20° C to 800° C." *Surface and Coatings Technology*, 258, 1183-1190.

Choudhury, S.D and Bhakta, U.C. (1996). "Superalloys in NTPC Gas Turbine and Their Properties." *R&D Journal*, 2-1, 41-46.

Das, S, Ghosh, S, Pandit, A, Bandyopadhyay, TK, Chattopadhyay, AB and Das, K. (2005). "Processing and characterisation of plasma sprayed zirconia-alumina-mullite composite coating on a mild-steel substrate." *Journal of materials science*, 40(18), 5087-5089.

Doddamani, Mrityunjay, Shunmugasamy, Vasanth Chakravarthy, Gupta, Nikhil and Vijayakumar, HB. (2015). "Compressive and flexural properties of functionally graded fly ash cenosphere-epoxy resin syntactic foams." *Polymer Composites*, 36(4), 685-693.

Du, Lingzhong, Huang, Chuanbing, Zhang, Weigang, Zhang, Jingmin and Liu, Wei. (2010). "Effect of NiCr Clad BaF₂-CaF₂ Addition on Wear Performance of Plasma Sprayed Chromium Carbide-Nichrome Coating." *Journal of thermal spray technology*, 19(3), 551-557.

Erdemir, Ali. (2001). "Solid lubricants and self-lubricating films." *Modern tribology handbook*, 2, 787.

- Eriksson, Robert, Yuan, Kang, Li, Xin-Hai and Peng, Ru Lin. (2015). "Corrosion of NiCoCrAlY Coatings and TBC Systems Subjected to Water Vapor and Sodium Sulfate." *Journal of thermal spray technology*, 24(6), 953-964.
- Fauchais, P. (2004). "Understanding plasma spraying." *Journal of Physics D: Applied Physics*, 37(9), 86.
- Fauchais, P., Vardelle, A. and Dussoubs, B. (2001). "Quo vadis thermal spraying?". *Journal of thermal spray technology*, 10(1), 44-66.
- Fauchais, Pierre, Coudert, JF and Vardelle, Michel. (1997). "Transient phenomena in plasma torches and in plasma sprayed coating generation." *Le Journal de Physique IV*, 7(C4), 187-198.
- Guilemany, JM, Miguel, JM, Vizcaino, S, Lorenzana, C, Delgado, J and Sanchez, J. (2002). "Role of heat treatments in the improvement of the sliding wear properties of Cr₃C₂-NiCr coatings." *Surface and Coatings Technology*, 157(2-3), 207-213.
- Hoop, PJ and Allen, C. (1999). "The high temperature erosion of commercial thermally sprayed metallic and cermet coatings by solid particles." *Wear*, 233, 334-341.
- Huang, Chuanbing, Du, Lingzhong and Zhang, Weigang. (2009). "Effects of solid lubricant content on the microstructure and properties of NiCr/Cr₃C₂-BaF₂·CaF₂ composite coatings." *Journal of Alloys and Compounds*, 479(1), 777-784.
- Huang, Chuanbing, Du, Lingzhong and Zhang, Weigang. (2014). "Friction and wear characteristics of plasma-sprayed self-lubrication coating with clad powder at elevated temperatures up to 800° C." *Journal of thermal spray technology*, 23(3), 463-469.
- Jafari, M, Enayati, MH, Salehi, M, Nahvi, SM and Park, CG. (2013). "Microstructural and mechanical characterizations of a novel HVOF-sprayed WC-Co coating deposited from electroless Ni-P coated WC-12Co powders." *Materials Science and Engineering: A*, 578, 46-53.

Jegadeeswaran, N, Ramesh, MR and Bhat, K Udaya. (2014). "Oxidation resistance HVOF sprayed coating 25%(Cr₃C₂-25 (Ni₂₀Cr))+ 75% NiCrAlY on titanium alloy." *Procedia Materials Science*, 5, 11-20.

Ji, Gang-Chang, Li, Chang-Jiu, Wang, Yu-Yue and Li, Wen-Ya. (2007). "Erosion performance of HVOF-sprayed Cr₃ C₂-NiCr coatings." *Journal of thermal spray technology*, 16(4), 557-565.

Kaur, Manpreet, Singh, Harpreet and Prakash, Satya. (2009). "High-Temperature Corrosion Studies of HVOF-Sprayed Cr₃C₂-NiCr Coating on SAE-347H Boiler Steel." *Journal of thermal spray technology*, 18(4), 619.

Kaur, Manpreet, Singh, Harpreet and Prakash, Satya. (2012). "High-temperature behavior of a high-velocity oxy-fuel sprayed Cr₃C₂-NiCr coating." *Metallurgical and Materials Transactions A*, 43(8), 2979-2993.

Kim, Gilyoung, Choi, Hanshin, Han, Changmin, Uhm, Sangho and Lee, Changhee. (2005). "Characterization of atmospheric plasma spray NiCr–Cr₂O₃–Ag–CaF₂/BaF₂ coatings." *Surface and Coatings Technology*, 195(1), 107-115.

Kong, Lingqian, Bi, Qinling, Niu, Muye, Zhu, Shengyu, Yang, Jun and Liu, Weimin. (2013). "ZrO₂ (Y₂O₃)–MoS₂–CaF₂ self-lubricating composite coupled with different ceramics from 20° C to 1000° C." *Tribology International*, 64, 53-62.

Krishna, L Rama, Sen, D, Rao, D Srinivasa and Sundararajan, G. (2003). "Coatability and characterization of fly ash deposited on mild steel by detonation spraying." *Journal of thermal spray technology*, 12(1), 77-79.

Kulu, P and Pihl, T. (2002). "Selection criteria for wear resistant powder coatings under extreme erosive wear conditions." *Journal of thermal spray technology*, 11(4), 517-522.

Li, Bo, Jia, Junhong, Gao, Yimin, Han, Minmin and Wang, Wenzhen. (2017). "Microstructural and tribological characterization of NiAl matrix self-lubricating

composite coatings by atmospheric plasma spraying." *Tribology International*, 109, 563-570.

Li, JF and Ding, CX. (2000). "Improvement in tribological properties of plasma-sprayed Cr₃C₂-NiCr coating followed by electroless Ni-based alloy plating." *Wear*, 240(1-2), 180-185.

Luo, Lai-Ma, Liu, Shao-Guang, Jia, Yu, Juan, LUO and Jian, LI. (2010). "Effect of Al content on high temperature erosion properties of arc-sprayed FeMnCrAl/Cr₃C₂ coatings." *Transactions of Nonferrous Metals Society of China*, 20(2), 201-206.

Manakari, Vyasraj, Parande, Gururaj, Doddamani, Mrityunjay, Gaitonde, VN, Siddhalingeshwar, IG, Shunmugasamy, Vasanth Chakravarthy and Gupta, Nikhil. (2015). "Dry sliding wear of epoxy/cenosphere syntactic foams." *Tribology International*, 92, 425-438.

Manjunatha, M, Kulkarni, RS and Krishna, M. (2014). "Investigation of HVOF Thermal Sprayed Cr₃C₂-NiCr Cermet Carbide Coatings on Erosive Performance of AISI 316 Molybdenum steel." *Procedia Materials Science*, 5, 622-629.

Martin Jr, Peter. (1972). A survey of solid lubricant technology: Army weapons command rock island il general thomas j rodman lab.

Metco, Sulzer. (2014). "An introduction to thermal spray." *Caderno informativo do fabricante*, 6.

Mishra, SB, Chandra, K and Prakash, S. (2008). "Characterisation and erosion behaviour of NiCrAlY coating produced by plasma spray method on two different Ni-based superalloys." *Materials Letters*, 62(12), 1999-2002.

Mishra, SB, Chandra, K and Prakash, S. (2013). "Erosion-corrosion performance of NiCrAlY coating produced by plasma spray process in a coal-fired thermal power plant." *Surface and Coatings Technology*, 216, 23-34.

Mishra, SC, Rout, KC, Padmanabhan, PVA and Mills, B. (2000). "Plasma spray coating of fly ash pre-mixed with aluminium powder deposited on metal substrates." *Journal of Materials Processing Technology*, 102(1), 9-13.

Mishra, SC, Satapathy, Alok, Singh, KP, Sethy, Sangeetha, Padmanabhan, PVA, Sreekumar, KP and Satpute, R. (2006) "Plasma spray coating of fly ash on metals for tribological application." *Proceedings of the International Seminar on Mineral Processing Technology* Chennai, 825-829.

Murthy, JKN, Rao, DS and Venkataraman, B. (2001). "Effect of grinding on the erosion behaviour of a WC-Co-Cr coating deposited by HVOF and detonation gun spray processes." *Wear*, 249(7), 592-600.

Niranatlumpong, P, Ponton, CB and Evans, HE. (2000). "The failure of protective oxides on plasma-sprayed NiCrAlY overlay coatings." *Oxidation of Metals*, 53(3-4), 241-258.

Ouyang, JH, Sasaki, S and Umeda, K. (2001). "Microstructure and tribological properties of low-pressure plasma-sprayed ZrO₂-CaF₂-Ag₂O composite coating at elevated temperature." *Wear*, 249(5-6), 440-451.

Ozdemir, I, Tekmen, C, Tsunekawa, Y and Grund, T. (2010). "Wear behavior of plasma-sprayed Al-Si/TiB 2/h-BN composite coatings." *Journal of thermal spray technology*, 19(1-2), 384-391.

Pfender, E. (1988). "Fundamental studies associated with the plasma spray process." *Surface and Coatings Technology*, 34(1), 1-14.

Picas, JA, Forn, A, Igartua, A and Mendoza, G. (2003). "Mechanical and tribological properties of high velocity oxy-fuel thermal sprayed nanocrystalline CrC.NiCr coatings." *Surface and Coatings Technology*, 174, 1095-1100.

Praveen, Ayyappan Susila, Sarangan, J, Suresh, S and Subramanian, J Siva. (2015). "Erosion wear behaviour of plasma sprayed NiCrSiB/Al₂O₃ composite coating." *International Journal of Refractory Metals and Hard Materials*, 52, 209-218.

- Ramachandran, CS, Balasubramanian, V and Ananthapadmanabhan, PV. (2013). "Erosion of atmospheric plasma sprayed rare earth oxide coatings under air suspended corundum particles." *Ceramics International*, 39(1), 649-672.
- Ramazani, M, Ashrafizadeh, F and Mozaffarinia, R. (2014). "Optimization of Composition in Ni (Al)-Cr₂O₃ Based Adaptive Nanocomposite Coatings." *Journal of thermal spray technology*, 23(6), 962-974.
- Ramesh, MR, Prakash, S, Nath, SK, Sapra, Pawan Kumar and Venkataraman, B. (2010). "Solid particle erosion of HVOF sprayed WC-Co/NiCrFeSiB coatings." *Wear*, 269(3-4), 197-205.
- Sahraoui, Tahar, Fenineche, Nour-Eddine, Montavon, Ghislain and Coddet, Christian. (2003). "Structure and wear behaviour of HVOF sprayed Cr₃C₂-NiCr and WC-Co coatings." *Materials & Design*, 24(5), 309-313.
- Sahu, Suwendu Prasad, Satapathy, Alok, Patnaik, Amar, Sreekumar, KP and Ananthapadmanabhan, PV. (2010). "Development, characterization and erosion wear response of plasma sprayed fly ash-aluminum coatings." *Materials & Design*, 31(3), 1165-1173.
- Santa, JF, Espitia, LA, Blanco, JA, Romo, SA and Toro, A. (2009). "Slurry and cavitation erosion resistance of thermal spray coatings." *Wear*, 267(1-4), 160-167.
- Seo, D, Ogawa, K, Suzuki, Y, Ichimura, K, Shoji, T and Murata, S. (2008). "Comparative study on oxidation behavior of selected MCrAlY coatings by elemental concentration profile analysis." *Applied Surface Science*, 255(5), 2581-2590.
- Sharma, Ashok and Goel, SK. (2016). "Erosion behaviour of WC-10Co-4Cr coating on 23-8-N nitronic steel by HVOF thermal spraying." *Applied Surface Science*, 370, 418-426.
- Sharma, S. (2012). "High temperature erosive wear study of NiCrFeSiB flame sprayed coatings." *Journal of The Institution of Engineers (India): Series D*, 93(1), 7-12.

Sidhu, Buta Singh, Singh, Harpreet, Puri, D and Prakash, S. (2007). "Wear and oxidation behaviour of shrouded plasma sprayed fly ash coatings." *Tribology International*, 40(5), 800-808.

Sidhu, TS, Prakash, S and Agrawal, RD. (2006). "Characterizations and hot corrosion resistance of Cr₃C₂-NiCr coating on Ni-base superalloys in an aggressive environment." *Journal of thermal spray technology*, 15(4), 811-816.

Sidhu, TS, Prakash, S and Agrawal, RD. (2006). "Studies of the metallurgical and mechanical properties of high velocity oxy-fuel sprayed stellite-6 coatings on Ni-and Fe-based superalloys." *Surface and Coatings Technology*, 201(1-2), 273-281.

Sidky, PS and Hocking, MG. (1999). "Review of inorganic coatings and coating processes for reducing wear and corrosion." *British Corrosion Journal*, 34(3), 171-183.

Singh, Harpreet, Kaur, Manpreet and Prakash, Satya. (2016). "High-Temperature Exposure Studies of HVOF-Sprayed Cr₃C₂-25 (NiCr)/(WC-Co) Coating." *Journal of thermal spray technology*, 25(6), 1192-1207.

Singh, Lakhwinder, Chawla, Vikas and Grewal, JS. (2012). "A review on detonation gun sprayed coatings." *Journal of Minerals & Materials Characterization & Engineering*, 11(3), 243-265.

Sliney, Harold E. (1969). "Rare earth fluorides and oxides-An exploratory study of their use as solid lubricants at temperatures to 1800 deg F/1000 deg C." *Springfield*, Washington DC.

Somasundaram, B, Kadoli, Ravikiran and Ramesh, MR. (2014). "Evaluation of cyclic oxidation and hot corrosion behavior of HVOF-sprayed WC-Co/NiCrAlY coating." *Journal of thermal spray technology*, 23(6), 1000-1008.

Tsunekawa, Y, Ozdemir, I and Okumiya, M. (2006). "Plasma sprayed cast iron coatings containing solid lubricant graphite and h-BN structure." *Journal of thermal spray technology*, 15(2), 239-245.

- Tucker Jr, Robert C. (1994). "Advanced thermal spray deposition techniques." Vol. 5. *ASM Handbook*.
- Vicenzi, J, Villanova, DL, Lima, MD, Takimi, AS, Marques, CM and Bergmann, CP. (2006). "HVOF-coatings against high temperature erosion ($\sim 300^\circ \text{C}$) by coal fly ash in thermoelectric power plant." *Materials & Design*, 27(3), 236-242.
- Wang, Bu-Qian and Verstak, Andrew. (1999). "Elevated temperature erosion of HVOF $\text{Cr}_3\text{C}_2/\text{TiC}-\text{NiCrMo}$ cermet coating." *Wear*, 233, 342-351.
- Wang, Bu Qian. (2003). "Hot erosion behavior of two new iron-based coatings sprayed by HVCC process." *Wear*, 255(1-6), 102-109.
- Wang, Bu Qian and Shui, Zheng Rong. (2002). "The hot erosion behavior of HVOF chromium carbide-metal cermet coatings sprayed with different powders." *Wear*, 253(5-6), 550-557.
- Wang, Hai-Dou, Xu, Bin-Shi, Liu, Jia-Jun and Zhuang, Da-Ming. (2005). "Characterization and tribological properties of plasma sprayed FeS solid lubrication coatings." *Materials Characterization*, 55(1), 43-49.
- Wang, Wenchao. (2004). "Application of a high temperature self-lubricating composite coating on steam turbine components." *Surface and Coatings Technology*, 177, 12-17.
- Wang, Y and Chen, W. (2003). "Effect of ceria on the erosion resistance of HVOF thermal sprayed NiAl intermetallic coatings." *Journal of materials science letters*, 22(11), 845-848.
- Wang, Y, Yang, Y and Yan, MF. (2007). "Microstructures, hardness and erosion behavior of thermal sprayed and heat treated NiAl coatings with different ceria." *Wear*, 263(1-6), 371-378.
- William, Batchelor Andrew, Margam, Chandrasekaran and Lam, Loh Nee. (2003). "Materials Degradation And Its Control By Surface Engineering." *World Scientific*.

Wood, Robert JK. (2010). "Tribology of thermal sprayed WC–Co coatings." *International Journal of Refractory Metals and Hard Materials*, 28(1), 82-94.

Xia, Zhidong, Zhang, Xiuying and Song, Jiayin. (1999). "Erosion-resistance of plasma sprayed coatings." *Journal of Materials Engineering and Performance*, 8(6), 716-718.

Yang, Guan-Jun, Li, Chang-Jiu, Zhang, Shi-Jun and Li, Cheng-Xin. (2008). "High-temperature erosion of HVOF sprayed Cr₃C₂-NiCr coating and mild steel for boiler tubes." *Journal of thermal spray technology*, 17(5-6), 782-787.

Yang, Q, Senda, T and Hirose, A. (2006). "Sliding wear behavior of WC–12% Co coatings at elevated temperatures." *Surface and Coatings Technology*, 200(14-15), 4208-4212.

Yoshida, M. (1993). "Effect of hot corrosion on the mechanical performances of superalloys and coating systems." *Corrosion science*, 35(5-8), 1115-1124.

Yuan, Jianhui, Zhu, Yingchun, Ji, Heng, Zheng, Xuebing, Ruan, Qichao, Niu, Yaran, Liu, Ziwei and Zeng, Yi. (2010). "Microstructures and tribological properties of plasma sprayed WC–Co–Cu–BaF₂/CaF₂ self-lubricating wear resistant coatings." *Applied Surface Science*, 256(16), 4938-4944.

Zavareh, Mitra Akhtari, Sarhan, Ahmed Aly Diaa Mohammed, Razak, Bushroa BintiAbd and Basirun, Wan Jeffrey. (2015). "The tribological and electrochemical behavior of HVOF-sprayed Cr₃C₂–NiCr ceramic coating on carbon steel." *Ceramics International*, 41(4), 5387-5396.

Zeltmann, Steven Eric, Bharath Kumar, B. R., Doddamani, Mrityunjay and Gupta, Nikhil. (2016). "Prediction of strain rate sensitivity of high density polyethylene using integral transform of dynamic mechanical analysis data." *Polymer*, 101, 1-6.

Zhang, Tiantian, Lan, Hao, Huang, Chuanbing, Yu, Shouquan, Du, Lingzhong and Zhang, Weigang. (2016). "Preparation and characterizations of nickel-based composite coatings with self-lubricating property at elevated temperatures." *Surface and Coatings Technology*, 294, 21-29.

Zhang, Xiao-Feng, Zhang, Xiang-Lin, Wang, Ai-Hua and Huang, Zao-Wen. (2009). "Microstructure and properties of HVOF sprayed Ni-based submicron WS_2/CaF_2 self-lubricating composite coating." *Transactions of Nonferrous Metals Society of China*, 19(1), 85-92.

Zhang, Zhenyu, Lu, Xinchun and Luo, Jianbin. (2007). "Tribological properties of rare earth oxide added Cr_3C_2-NiCr coatings." *Applied Surface Science*, 253(9), 4377-4385.

Zhen, Jinming, Cheng, Jun, Li, Maohua, Zhu, Shengyu, Long, Zerong, Yang, Bo and Yang, Jun. (2017). "Lubricating behavior of adaptive nickel alloy matrix composites with multiple solid lubricants from 25° C to 700°C." *Tribology International*, 109, 174-181.

Zhou, Wuxi, Zhou, Kesong, Deng, Chunming, Zeng, Keli and Li, Yuxi. (2017). "Hot corrosion behavior of HVOF-sprayed $Cr_3C_2-WC-NiCoCrMo$ coating." *Ceramics International*, 43(12), 9390-9400.

LIST OF PUBLICATIONS

INTERNATIONAL JOURNALS

1. Mahantayya Mathapati, Ramesh, M. R., & Mrityunjay Doddamani. (2017). “High temperature erosion behavior of plasma sprayed NiCrAlY/WC-Co/cenosphere coating”. *Surface and Coatings Technology*, 325, 98-106. (Elsevier, 2.96)
2. Mahantayya Mathapati, Mrityunjay Doddamani, & Ramesh, M. R. (2018) “High-Temperature Erosive Behavior of Plasma Sprayed Cr₃C₂-NiCr/Cenosphere Coating”. *Journal of Materials Engineering and Performance*, 1-9. (Springer, 1.30)

INTERNATIONAL CONFERENCES

1. Mahantayya Mathapati, Ramesh, M. R., & Mrityunjay Doddamani. (2017) “High Temperature Erosion Behaviour of Plasma Sprayed NiCrAlY-25WC-Co/Cenospheres Composite Coating.” 6Th International Engineering Symposium, March 1-3, Kumamoto University, Japan.
2. Mahantayya Mathapati, Ramesh, M. R., & Doddamani, M. (2018) “Cyclic Oxidation Behaviour of Plasma Sprayed NiCrAlY-25WC-Co/Cenosphere Coating.” International Conference on Design, Materials and Manufacturing, January 29-31, NITK, India.

BIO-DATA

1. **Name** : Mahantayya Mathapati
2. **Father's Name** : Kallayya Mathapati
3. **Date of Birth** : 12th May 1988
4. **Nationality** : Indian
5. **Marital Status** : Married
6. **Address** : Department of Mechanical Engineering
National Institute of Technology Karnataka
Surathkal, PO Srinivasnagar 575 025
Karnataka, India.
7. **Mobile Number** : +91 9739866342
8. **E-mail id.** : *mahantkm@gmail.com*
9. **Educational Qualification** :

Qualification	University/Board	Year of Passing
Ph.D. (Mechanical Engineering)	National Institute of Technology Karnataka	Pursuing
M.Tech. (Mechanical Engineering)	Visvesvaraya Technological University, Belgaum	2013
B.E. (Automobile Engineering)	Visvesvaraya Technological University, Belgaum	2010
